

ELECTRON AND PHONON DYNAMICS IN NANOSTRUCTURES

by

SHI-XIAN QU

(Under the direction of Heinz-Bernd Schüttler and Michael R. Geller)

ABSTRACT

This thesis comprises three major parts relating to the electron and phonon dynamics in nanostructures.

In the first part, a finite temperature Green's function theory for spherically symmetric systems is advanced, in which a self-consistent dressed random phase approximation is proposed. The finite element method is generalized to solve the Dyson equations for the Green's function and the screening potential. The linear response theory is then used to obtain the electron polarizability. By the Padé approximant, the imaginary Matsubara frequency dependence is analytically continued to calculate the polarizability in the real frequency domain. This approach has been applied to Gold and Sodium nanosphere systems.

In the second part, a general theoretical technique is developed to describe wave propagation through a curved wire of uniform cross section and lying in a plane, but of otherwise arbitrary shape. The method consists of (i) introducing a local orthogonal coordinate system, the arclength and two locally perpendicular coordinate axes, dictated by the shape of the wire; (ii) rewriting the wave equation of interest in this system; (iii) identifying an effective scattering potential caused by the local curvature; and (iv), solving the associated Lippmann-Schwinger equation for the scattering matrix. We carry out this procedure in detail for the scalar Helmholtz equation with both hard-wall and stress-free boundary conditions, appropriate for the mesoscopic transport of electrons and (scalar) phonons. The results show that, in contrast to charge transport, curvature only barely

suppresses thermal transport, even for sharply bent wires, at least within the two-dimensional scalar phonon model considered. Applications to experiments are also discussed.

In the third part, a general method is developed to calculate the net rate of thermal energy transfer between a three-dimensional conductor at temperature T_{el} and a low-dimensional phonon system at temperature T_{ph} . The main focus and principal result is a calculation of the rate of energy transfer between a clean metal film of thickness d attached to an insulating, nonpolar semi-infinite substrate. The conventional deformation-potential is employed to describe the electron-phonon scattering. A low-temperature crossover from the familiar T^5 temperature dependence to a strong $T^6 \log T$ scaling is predicted. Comparison with the existing experiments suggests a widespread breakdown of the standard model of electron-phonon thermalization in supported metallic thin films.

INDEX WORDS: Metallic Nanoparticles, Quantum wires, Low-dimensional phonon systems, Surface plasmon oscillation, Hot-electron, Susceptibility, Polarizability, Thermal Conductance, Finite Temperature Green's Function, Dyson equation, Feynman diagrams, Random phase approximation, Linear response theory, Lippmann-Schwinger equation, Finite element method.

ELECTRON AND PHONON DYNAMICS IN NANOSTRUCTURES

by

SHI-XIAN QU

B.S., Northwest University, China, 1983

M.S., Institute of Physics, Chinese Academy of Sciences, China, 1988

A Dissertation Submitted to the Graduate Faculty
of The University of Georgia in Partial Fulfillment
of the
Requirements for the Degree

DOCTOR OF PHILOSOPHY

ATHENS, GEORGIA

2005

© 2005

Shi-Xian Qu

All Rights Reserved

ELECTRON AND PHONON DYNAMICS IN NANOSTRUCTURES

by

SHI-XIAN QU

Approved:

Major Professors: Heinz-Bernd Schüttler
 Michael R. Geller

Committee: William M. Dennis
 Kanzo Nakayama
 Yiping Zhao

Electronic Version Approved:

Maureen Grasso
Dean of the Graduate School
The University of Georgia
May 2005

ACKNOWLEDGMENTS

I would like to express my heartfelt gratitude to Prof. Heinz-Bernd Schüttler and Prof. Michael R. Geller, my supervisors. I am thankful to Bernd for his kindness, his patience, his wise guidance, and the finance support and for teaching me understanding the physics behind the sophisticated theories and formulas. The most impressed skill amongst all the analytical and numerical skills that he taught me is how to incorporate the analytical properties in the numerical realization of a physics problem. I am thankful to Michael for his caring, fruitful guiding, and enthusiastic encouragement and support. Not only did he teach me the beauty of the theoretical physics (the deep insight into physics), but also the way to bridge theory and experiment. Most importantly, he always do his best to provide me with every chance to contact with the pioneer researchers on and off the campus, which benefited me a lot. I appreciate it very much.

I wish to thank all the other members of my advisory committee, Prof. William M. Dennis, Prof. Kanzo Nakayama and Prof. Yiping Zhao, for their helpful comments on the dissertation, and their guidance and encouragement during the past years. I also wish to thank all the members of my preliminary advisory committee, Prof. F. Todd Baker, Prof. M. Howard Lee, and Prof. Phillip C. Stancil and Prof. Uwe Happek, for their guidance and help as soon as I entered this university.

I would like to express my appreciation to Prof. David P. Landau, director of the Center for Simulational Physics. I thank him very much for offering me a quiet office where I have spent very important period of time in my research, allowing me to use the facilities of the center. My thanks are also due to his wonderful lessons on the Monte Carlo Simulation and to many informative and encouraging talks with him.

I am very grateful for the hospitality and friendship of Prof. Richard S. Meltzer and his wife Angela Meltzer. During my stay here in UGA, his wife and he gave me and my family a lot of help and encouragement, which made us feel like we lived at our homeland.

I also wish to show my gratitude to my late advisor Dr. Alexander Leyderman for inviting me to be a visiting professor in his group and later permitting me to break the contract with him to transfer to UGA as a student.

My acknowledgment is also due to Dr. Alfonso Barrientos for his friendship and for his inviting me to work in his group. I would like to show my thanks to Dr. Xiao-Jun Wang for his friendship and all the help, and also to my friends Dr. Jianguo Wang and Dr. Libao Zhao for their help. I am thankful to Dr. Shan-Ho Tsai for her kindly guidance of the computational techniques.

I appreciate all the assistance from Mr. Mike Caplinger, Mr. Jeff Deroshia and Mr Tom Barnello. Their hardwork for and faithful service to our society are the deep impression to me. I would also like to show my appreciation to all the beautiful staff ladies, Dale, Joline, Linda, Norma, Mica, Sherri and Stephanie, for their hospitality, kindness, patience and enthusiasm. They help to build up a quiet, relaxed and efficient atmosphere for the department.

I would like to recognize the help and friendship from my classmates, Fugao Wang, Jianwei Wang, Wenduo Zhou, Xiaoliang Zhu, Qing Zhang, Yihai Yu, Bo Wen, Chongshan Zhang, Zhuofei Hou and Lijun Pang. The special thanks are due to Cejun Liu for his help in the earlier days when I came here in Athens, and also to Xiuping Tao for all her kindly help and the wonderful time sharing the same office.

My gratitude to Prof. Da-Ren He is for his advice, cooperation and consistent support for many years.

I would like to thank my wife, Hairong Zheng, and my lovely son, Yingqi Qu, for their patience and support during my study. I would never have finished it without their love and understanding. Finally I wish to thank my father, my mother, my younger sisters and brother. Their love, support and understanding are the primary power leading my every success.

TABLE OF CONTENTS

	Page
ACKNOWLEDGMENTS	iv
LIST OF FIGURES	viii
LIST OF TABLES	x
CHAPTER	
1 INTRODUCTION AND LITERATURE REVIEW	1
2 REAL SPACE GREEN'S FUNCTION FOR SPHERICALLY SYMMETRIC SYSTEMS	11
2.1 SELF-CONSISTENT DRESSED RANDOM PHASE APPROXIMATION AT FINITE TEMPERATURE	11
2.2 SPHERICALLY SYMMETRIC SYSTEMS AND RADIAL GREEN'S FUNCTION . . .	18
2.3 HARTREE SELF-ENERGY	21
2.4 FOCK SELF-ENERGY	22
2.5 POLARIZATION OPERATOR AND SCREENED POTENTIAL	23
2.6 DYSON EQUATION FOR RADIAL GREEN'S FUNCTION	28
3 FINITE ELEMENT METHOD AND ITS APPLICATION IN SOLVING THE DYSON EQUATIONS	30
3.1 INTRODUCTION TO FINITE ELEMENT METHOD	30
3.2 FINITE ELEMENT FORM OF SCHRÖDINGER EQUATION	38
3.3 FINITE ELEMENT FORM OF DYSON EQUATIONS FOR RADIAL GREEN'S FUNC- TION AND SCREENING POTENTIAL	44
4 ELECTRON POLARIZATION AND LINEAR RESPONSE THEORY	48
4.1 ELECTRODYNAMICS OF ELECTRON POLARIZATION	48

4.2	LINEAR RESPONSE THEORY FOR ELECTRON DENSITY	50
4.3	τ -ORDER CORRELATION FUNCTION AND THE FINITE TEMPERATURE GREEN'S FUNCTION	53
4.4	τ -ORDER CORRELATION FUNCTION FOR THE POLARIZABILITY FOR SPHERI- CALLY SYMMETRIC SYSTEMS	56
4.5	DYNAMICAL POLARIZABILITY AND OPTICAL ABSORPTION CROSS SECTION . .	58
5	APPLICATIONS TO SPHERICALLY SYMMETRIC NANOPARTICLES . .	60
5.1	SYSTEMS AND BACKGROUND POTENTIAL	60
5.2	COMPUTATIONAL PROCEDURES	61
5.3	RESULTS AND DISCUSSION	67
6	MESOSCOPIC ELECTRON AND PHONON TRANSPORT THROUGH A CURVED WIRE	71
6.1	INTRODUCTION	72
6.2	APPLICATION TO SCALAR WAVE EQUATION	74
6.3	ELECTRON TRANSPORT	81
6.4	PHONON TRANSPORT	82
6.5	DISCUSSION	85
7	HOT ELECTRONS IN LOW-DIMENSIONAL PHONON SYSTEMS	87
8	CONCLUSION	96
	BIBLIOGRAPHY	97
	APPENDIX	
A	SOME USEFUL RELATIONS FOR THE CLEBSCH-GODAN COEFFICIENTS	105
A.1	REDEFINED CLEBSCH-GODAN COEFFICIENTS \tilde{C}	105
A.2	SOME SPECIAL CG COEFFICIENTS	106
B	THE ASYMPTOTICAL BEHAVIOR OF THE RADIAL GREEN'S FUNCTION	108
C	INTEGRALS INVOLVING PRODUCTS OF DIRAC DELTA FUNCTIONS AND STEP FUNC- TIONS	110

LIST OF FIGURES

1.1	Self-consistent effective potential of jellium sphere	4
2.1	Diagrammatic Dyson equation for the finite temperature Green's function	15
2.2	Feynman diagram for the Hartree-Fock self-energy	16
2.3	Ring approximation to the effective two-body interaction	17
2.4	Diagrammatic Dyson equation for the effective two-body interaction	17
2.5	Feynman diagram for the self-energy in DRPA approximation	18
3.1	1-D finite element mesh and piecewise tent function	34
3.2	linear basis functions in local coordinate system	37
3.3	Quadratic Lagrange polynomials	38
3.4	Cubic Hermite polynomials	38
5.1	Integral contour	62
5.2	Variation of the chemical potential with the number of iterations	64
5.3	Variation of the relative error on the self-energy in two successive iterations with the times of iteration	65
5.4	Variation of the relative error on the Green's function in two successive iterations with the times of iteration	65
5.5	Variation of the chemical potential with the angular quantum number cutoff	66
5.6	Temperature dependence of the chemical potential for a Gold sphere with the radius of 1nm	67
5.7	Distribution of the radial electron density for a Gold sphere with the radius of 1nm at different temperatures	67
5.8	Electron leakage from Gold nanospheres in Hartree-Fock Approximation	68
5.9	Electron leakage from Sodium spheres in Hartree-Fock Approximation	68
5.10	Imaginary part of the dynamical polarizability for Gold nanospheres in Hartree-Fock Approximation	69

5.11	Imaginary part of the dynamical polarizability for Sodium nanospheres in Hartree-Fock Approximation	69
5.12	Electron leakage from Gold nanoparticles in DRPA Approximation	70
5.13	Electron leakage from Sodium nanoparticles in DRPA Approximation	70
6.1	2D curved wire geometry and the local orthogonal coordinates	72
6.2	Dispersion relation for unperturbed scattering states	76
6.3	Section of quantum wire with circular right-angle bend.	81
6.4	Individual electron transmission probabilities for a circular right-angle bend with $R/b = 1.20$	82
6.5	Total electron transmission probability for a circular right-angle bend with $R/b = 1.20$	82
6.6	Individual phonon transmission probabilities $ t_{nn'} ^2$ as a function of energy for a circular right-angle bend with $R = 2b$. Here $\Delta_{\text{ph}} \equiv \pi \hbar v/b$	83
6.7	Individual phonon transmission probabilities $ t_{nn'} ^2$ as a function of energy for a circular right-angle bend with $R = 1.001b$	83
6.8	Dimensionless thermal conductance $G_{\text{th}}/G_{\text{q}}$	84
6.9	The solid curve is the same as Fig. 6.8. Dashed curve is the dimensionless thermal conductance for a straight Si-like wire with $b = 100$ nm. Thermal transport is hardly suppressed by the bending.	84
6.10	Individual phonon transmission probabilities $ t_{nn'} ^2$ as a function of energy for a circular right-angle bend with $R = 1.00001b$	84
7.1	(inset) Conducting film of thickness d attached to insulator. The top surface of the metal is stress-free. (main) Temperature dependence of the thermal power exponent x for a 10 nm (solid curve) and 100 nm (dashed curve) Cu film.	91

LIST OF TABLES

7.1	Values of the parameter c for the five branches of vibrational modes of a semi-infinite substrate.	91
-----	--	----

CHAPTER 1

INTRODUCTION AND LITERATURE REVIEW

In the last decade, new directions of modern research, broadly defined as nanoscience and nanotechnology, have emerged [1–4]. This new trend involves the fabrication, characterization, manipulation of materials and artificial structures at the atomic, molecular or macromolecular levels, length scales of approximately 0.1 to 100 nanometers, providing a fundamental understanding of physical phenomena occurring in this same scale. Nanoscience is intrinsically cross disciplinary including diverse research areas as engineering, physics, chemistry, material science and biology. There is no doubt that nanoscience and nanotechnology have become important factors with considerable impact and will be the most critical, if not dominant, basis for technological innovations in the new century. Revolutionary consequences can be expected if the most unique properties of nanostructures, their electronic properties, are exploited.

In typical nanostructures the motion of electrons and phonons are confined in one or more than one directions in the nanometer scale. Their mean free paths are usually greater than or comparable to the size of the structures. Therefore, the electron and phonon dynamics will be significantly different from those in bulk solids. They are thus a very important area in nanoscience research. Included in this dissertation are three different subjects: the optical (electronic) response of metallic nanoparticles (to the electromagnetic field), electron and phonon transport through curved nanowires, and hot-electrons in low-dimensional phonon systems. They will be introduced separately in the following paragraphs.

As a consequence of reducing material size, the electronic properties change drastically as the density of states and the length scale of electronic motion are reduced. The energy level structure of electrons is now determined by the boundaries of the system, and undergoes a cross-over from a bulk band structure to discrete energy levels (shell structure) [5–7] in clusters (or nanoparticles) of sub-nanometer to nanometer sizes. Hence the quantum size effect obviously attracts great interest

from researchers searching for the novel materials with special properties, such as size-dependent new optical properties which have never been observed in molecules and in bulk materials. Reviews of the properties of nanoparticles and the underlying physics have been given in [17, 18, 20]. The research on the structural and physical properties of nanoparticles is a very important field because it has not only the great academic value [8], but also the promising application potential, such as optical storage [9], solar energy conversion [11], single electron tunneling [10], catalysis [12, 13], and also biology and biomedicine [14–16].

The study of light-matter interactions has played an important role in the development of modern physics. The optical spectroscopy method has thus been widely employed in the research of nanoparticles and clusters [17–28]. The reason is that the optical response of nanoparticles directly reflects their electronic structures. It can be studied either on free clusters [23–28], or on structured geometries of nanoparticles [29–32]. The main feature observed in the optical response of nanoparticles is the surface plasmon excitation which corresponds to the collective oscillation of the conduction electrons with respect to the ionic background. The conduction electrons in bulk alkaline and noble metals follows a nearly free electron behavior and their contribution to the dielectric constant, ϵ , is described by the Drude formula [33, 34]: $\epsilon(\omega) = 1 - \omega_p^2 / [\omega^2 + i\omega/\tau]$, where ω_p is the volume plasmon frequency of bulk materials ($\omega_p^2 = 4\pi ne^2/m$, n being number density of conduction electrons and m the effective mass of electron), τ is the electron relaxation time. In the simple model of free-electron gas embedded in a spherically homogeneous positive charge distribution [20], classical electrodynamics predicts that the surface plasmon resonance occurs at $\omega_s = \omega_p/\sqrt{3}$. This is the result of the quasi-static approximation when the radius of a sphere is much smaller than the wavelength of the incident electromagnetic wave, and can also be obtained through the dipolar approximation of Mie’s classical theory. Most experiments on the alkaline and some noble metal nanoparticles reveal large deviation from this prediction, such as the red- or blue-shift of the plasmon frequency with respect to the classical value as the particle size decreases, depending on the materials or the experimental conditions [17, 18, 20]. Clearly the step function type electron density at the nanosphere surface may not be an appropriate approximation and quantum theory should be introduced when the particle size is not substantially larger than the bulk Fermi wavelength ($\lambda_F \sim 0.5\text{nm}$).

The application of quantum mechanics gives rise to the electronic shell structure [5–7] which reveals the quantized motion of the delocalized conduction electrons in the mean field created by the ions in a cluster. In different experimental conditions, the details of ionic structure have been found not to affect the properties of alkali and other simple metal clusters [17,18]. This suggests the use of the jellium model which is defined by a Hamiltonian that treats the electrons in the usually quantum mechanical way, but approximates the field of the ionic cores by a uniform positively charged background with a constant charge density ρ_{IO} . For a spherically symmetric jellium model, this charge density is determined by $\rho_{\text{IO}} = e [4\pi r_s^3/3]^{-1} \Theta(R-r)$, where e is the elementary charge, r_s is the Wigner-Seitz radius of the conduction electrons in the corresponding bulk metal, and $\Theta(x)$ is a step function with $R = r_s N^{1/3}$ being the radius of a jellium sphere consisting of N atoms. Actually, we have no way to determine the finite-size variation of r_s theoretically, so that the simplest choice is that of the corresponding bulk value [18]. We have to admit that it is really a naive assumption. But it has proven to be an almost ideal theoretical instrument for approaching the goal addressed in the review paper [18]: It is simple enough to be applied to spherical metal clusters containing up to several thousand atoms, but still allows for a self-consistent microscopic description of the average field felt by the valence electrons, thus correctly reproducing many of the observed shell structures. At the same time it allows one to extract parameters from finite clusters that can be directly compared to those of the bulk or planar metal surface to which it has been applied already for about thirty years. Its success in describing the “supershell” structure in very large alkaline clusters, for which none of the more detailed structural models have any chance to compete, speaks of itself. Of course, there are limitations in the application of this model [18]. The conduction electrons must be strongly delocalized, a condition met by metals that are good conductors. This is why the jellium model has been mainly applied in the study of nanoparticles of alkali and noble metals.

Alkali metal clusters provide very good testing cases for the jellium model because the conduction electrons are free-electron-like and the Fermi surface is nearly spherical. Especially for sodium, the deviations from a perfect Fermi sphere are negligible [34]. Thus a spherically symmetric potential is assumed to simulate the field created by the ionic cores. This is what was done in reference [5] where the Woods-Saxon potential was used. Solving the corresponding Schrödinger

equation, they got the shell structure of the conduction electrons. Similar to nuclear physics, the quantum states of conduction electrons are labeled with the principal quantum number n and the angular quantum number l . The levels are degenerate due to the spherical symmetry of this background potential. The energy shells are successively filled by the conduction electrons. As for atoms, the electronic system of a cluster with exactly the right number (the magic number) of electrons to complete a shell is very stable. When one more atom is added to the cluster, its valent electrons will occupy a state with considerably higher energy, and hence reduce the stability of the system. This is just the scenario shown by the abundance spectrum of sodium clusters. A self-consistent computation by Chou et. al. [36], based upon the jellium model of sodium cluster of 40 atoms, also shows the above mentioned shell structure. Fig. 1.1 depicts the corresponding effective potential. Further examples are given by Ekardt [37,38], where the density functional theory is applied and the nonlocalized electronic exchange-correlation is replaced by a localized potential of the Gunnarsson and Lundqvist type [41], *i.e.*, using the local density approximation (LDA). In this approximation, the shell structures of sodium clusters with different numbers of atoms are obtained by self-consistently solving the single-particle Kohn-Sham equations. Independent work by Beck also suggests the same result [39]. All these have shown the validity of the jellium model and have encouraged applications of this model to larger systems in which the molecular dynamics computation becomes more and more time consuming and one is bound to rely on the jellium model predictions.

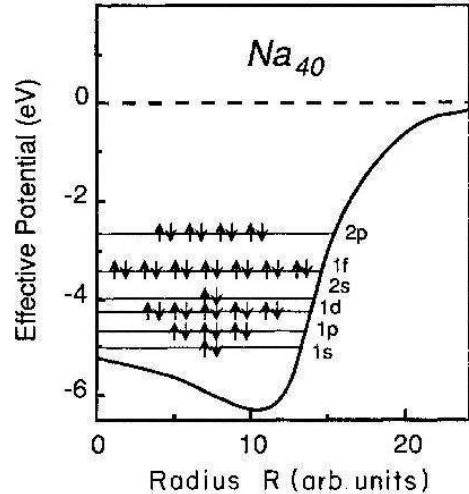


Figure 1.1: Self-consistent effective potential of jellium sphere with the corresponding electron occupation of energy levels [36].

Besides the original LDA, various improved approaches have been developed to investigate the optical properties of the alkaline clusters, such as the time dependent LDA (TDLDA) [40, 42], the LDA based random phase approximation (RPA) [43–47], Hartree-Fock ground state based full quantum mechanics RPA [48] and others. Numerous theoretical investigations have already pro-

vided us with very good understanding of the static and the dynamical properties of the alkaline nanoparticles, especially the finite size effects – the red-shift of the plasmon frequency and accordingly the increase of the static polarizability with the decreasing particle size. It is believed that this effect is attributed to the electron spilling out beyond the ionic background charge boundary. The smaller the cluster, the more prominent the spill out. It reduces the effective electron density and thereby the resonance frequency. Depending on the element, better agreement with the experimental results can be achieved by introducing various modifications such as shape deformation, effective mass corrections, pseudopotentials, core polarization effects or discrete ionic structures [54].

The situation concerning the size dependence of the optical absorption spectrum is more complicated for noble metal nanoparticles because the binding energies of the completely filled d -band are close to those of the partially filled s -band [20]. The polarization of the core electrons causes considerable screening of the conduction electrons, which contributes a non-zero susceptibility $\chi_d = \epsilon_d(\omega) - 1$, and hence results in the shift of the volume plasmon, surface plasmon and the Mie resonance to lower frequencies. At assumption that the imaginary component of χ_d is negligible, one may estimate the magnitude through the resonant condition of $\omega_s = \omega_p / [2\epsilon_m + \epsilon_d'']^{1/2}$, where ϵ_m is the dielectric constant of the surrounding matrix. The screening effect on the electrons near or beyond the surface is weaker than that on the inner ones, which induces an increase of the plasmon frequency. The smaller the size, the larger the portion of electrons which experiences weaker screening. In spite of some contradictory results most of the experiments support this blue-shift with the decreasing particle size. The interplay between the d -electron screening and the spillout effects is responsible for the overall complexity of the resonance behavior [50]. A phenomenological two-region dielectric model has been proposed to deal with this complex size dependence [49, 50]. In this model, an effective medium with dielectric constant $\epsilon_d(\omega)$ is assumed for the inner sphere of radius R_d , and the shell of thickness d is vacuum with dielectric constant $\epsilon = 1$, where $R_d = R - d$, $R = r_s N^{1/3}$ is the radius of a jellium sphere of N atoms, and the thickness d is in the order of the Wigner-Seitz radius r_s . Employing this model, many theoretical works with TDLDA or RPA based upon LDA have been carried out to qualitatively and quantitatively explain experimental observations on the optical response of noble metal clusters, and achieved great success [51–56].

So far, nearly all the jellium model calculations are within the framework of the density functional theory. In these applications, the local density approximation is used to treat the exchange-correlation, which use locally the exchange correlation energy per electron $e_{xc}(\rho)$ obtained in many-body calculations for an infinite system of electrons with the constant density ρ , *i.e.*, e_{xc} is taken at the local value $\rho = \rho(\mathbf{r})$ everywhere in this finite system. By construction, this approximation is exact only in those regions of space where the density $\rho(\mathbf{r})$ is constant, while in the current object of nanoparticle systems the density function shows a strong variation in the surface region. Although its applications have achieved considerable success in almost all branches of physics including nanoparticle systems, its validity were never analyzed from a theoretical point of view [54]. A fully quantum theory justification is still in need. We note that Guet and Jognson have ever developed a fully quantum mechanical matrix RPA based on the Hartee-Fock ground state [48]. In their approach the exchange-correlation is treated nonlocally, and they observed a redshift of the plasmon frequency with respect to the experimental measurement rather than the blue-shift reported in the previous LDA-RPA studies. Also an improvement of the agreement between calculations and experimental data was achieved to a certain extent.

As it is well known, the finite temperature Green's function method [61–63] is a powerful theoretical tool which has been shown to be very successful in dealing with both the equilibrium and the excited state problems in condensed matter systems. To the best of our knowledge, we have not found any previous work applying this method to compute the optical properties of nanoparticles. Recently, there has been increasing interests in the temperature effect of the optical properties and the electron dynamics of nanoparticles [57–60]. The finite temperature Green's function method takes the temperature effects into account in a natural way. In the current dissertation work, we apply this method to calculate the optical properties of any metallic nanoparticle with spherically symmetric geometry. Our primary goal is to develop novel computational tools for the comprehensive, quantitative modeling of the optical properties of these structures. In our approach, the jellium model is chosen as the positive background potential to confine the conduction electrons, and the mutual, repulsive Coulomb interactions between conduction electrons is treated fully quantum mechanically. The Dyson equations for the nonlocalized screening potential and finite temperature Green's function in real-space and imaginary-frequence domain are set up within the framework of

a so-called “dressed random phase approximation”(DRPA). The lack of translation symmetry in nanoparticles make the numerical solutions of these coupled self-consistent field equations a great computational challenge. Considering the spherical symmetry, the angular and radial portions of these equations are separated by using the angular momentum theory [66]. The finite element method [67] is extended to the Green’s function calculations, which considerably stabilizes the self-consistent iterations and saves the computation time. Even though great effort has been made to develop a highly efficient numerical algorithm to solve these self-consistent field equations, our computations are still confined by the constraints of currently available high-performance computing capabilities.

A new class of nanomechanics is attempting to measure extremely minute amounts of energy, of the order a few neV, and to use such calorimeters to probe fundamental properties of thermal conduction in the nanoscale regime [76–80]. Like the related case of electrical conduction [81, 82], low-temperature thermal conduction in nanostructures is entirely different than in macroscopic materials because the phonons are in the mesoscopic regime, where they scatter elastically but not inelastically. Because inelastic scattering is required to establish thermodynamic equilibrium, there is a breakdown of Fourier’s law and the heat equation, which assume a local thermodynamic equilibrium characterized by a spatially varying temperature profile. These nanodevices have inspired considerable theoretical work on thermal transport by phonons in the mesoscopic limit [83–97].

There has been considerable attention given to mesoscopic electron transport through curved wires and waveguides [100], but none to thermal transport. Electron transmission probabilities in curved wires are usually obtained by mode-matching, a method restricted to piecewise separable geometries (wires composed of straight segments, circles, and other shapes where the wave equation is separable). A related problem that has been studied extensively is the formation of electronic bound states and resonances in curved wires, where the mapping to local curvilinear coordinates is also often used [100–102]. Surprisingly, we are not aware of any work using moving frames and then directly solving the resulting Lippmann-Schwinger equation in that basis. Nor are we aware of the use of this method in the extensive microwave engineering literature [104, 105], where the (more generally applicable but purely numerical) finite-element method is the technique of choice.

In this work we introduce a general method to calculate the scattering matrix for waves propagating through a curved wire or waveguide. The wire is assumed to be of uniform cross-section and lying in a plane, but the curved segment may have any smooth curvature profile. The ends of the wire (the “leads”) are also assumed to be straight. For definiteness we consider two-dimensional waves described by the scalar Helmholtz equation

$$[\nabla^2 + \alpha]\Phi(\mathbf{r}) = 0, \quad \mathbf{r} \equiv (x, y)$$

Here $\alpha(\epsilon) \equiv 2m\epsilon/\hbar^2$ in the case of electrons of energy ϵ and mass m , whereas $\alpha(\epsilon) \equiv \epsilon^2/\hbar^2 v^2$ in the case of scalar phonons of energy ϵ and bulk sound velocity v . The hard wall boundary condition is assumed for electrons, but the stress free boundary condition for the phonon case. Our approach involves rewriting this equation and the boundary conditions in terms of new curvilinear coordinates X and Y , dictated by the shape of the wire, such that the wave equation becomes more complicated (the wire’s curvature produces an effective potential), but the boundary conditions become trivial. We choose X to be the arclength along one edge of the wire, and Y is locally perpendicular. This transformation allows us to apply the standard techniques of scattering theory, including solution of the Lippmann-Schwinger equation, in the XY frame.

A particularly novel aspect of the phonon transport problem is that the reflection probability always vanishes in the long-wavelength limit, permitting an analytic (second-order Born approximation) treatment at low energies. The energy-dependent transmission probability is then expressed as a simple functional of the curvature profile $\kappa(X)$, making possible a straightforward analysis of a variety of wire shapes.

The interaction between electrons and phonons at low temperatures is a subject of considerable interest and importance, as this coupling is the primary mechanism by which an electron system can exchange energy with its environment. At low temperatures, electron-electron scattering will cause nonequilibrium electrons to equilibrate on a timescale that is typically much shorter than the electron-phonon equilibration time, resulting in an electron distribution that is thermal, but at a temperature higher than that of the lattice. Understanding the effects of these “hot” electrons is crucial in studies of transport in semiconductors and metals at low temperatures [114]. The widely used “standard” model of low temperature electron-phonon thermal coupling and hot-electron

effects in bulk metals [113, 114] assumes (i) a clean three-dimensional free-electron gas with a spherical Fermi surface, rapidly equilibrated to a temperature T_{el} ; (ii) a continuum description of the acoustic phonons, which have a temperature T_{ph} ; (iii) a negligible Kapitza-like thermal boundary resistance [115] between the metal and any surrounding dielectric, an assumption that is well justified experimentally; and (iv), a deformation-potential electron-phonon coupling, expected to be the dominant interaction at long-wavelengths. In a bulk metal, the net rate P of thermal energy transfer between the electron and phonon subsystems is [114]

$$P = \Sigma V_{\text{el}} (T_{\text{el}}^5 - T_{\text{ph}}^5),$$

where V_{el} is the volume of the metal, and

$$\Sigma \equiv \frac{8 \zeta(5) k_{\text{B}}^5 \epsilon_{\text{F}}^2 N_{\text{el}}(\epsilon_{\text{F}})}{3\pi \hbar^4 \rho v_{\text{F}} v_{\text{l}}^4}.$$

Here ζ is the Riemann zeta function, ϵ_{F} is the Fermi energy, N_{el} is the electronic density of states (DOS) per unit volume, ρ is the mass density, v_{l} is the bulk longitudinal sound speed, and v_{F} is the Fermi velocity.

This model, which has no adjustable parameters, has successfully explained some experiments [114, 116, 117], but others report a power-law temperature dependence with smaller exponents [118, 119], indicating an enhanced electron-phonon coupling at low temperatures. However, the experiments typically involve heating measurements in thin metal films deposited on semiconducting substrates, and the relevant phonons at low temperature are strongly modified by the exposed stress-free surface. An attempt to directly probe such phonon-dimensionality effects was carried out by DiTusa *et al.* [119], who intentionally suspended some of their samples, necessarily modifying the vibrational spectrum, although they found no significant difference from their supported films. We argue that the paradox reported in Ref. [119] is actually quite widespread, and all experiments known to us on supported films actually contradict the standard model when that model is modified to account for the actual vibrational modes present in a realistic supported-film geometry. Our results have important implications for the thermal properties of mesoscopic and low-dimensional phonon systems and the use of such systems as nanoscale thermometers, bolometers, and calorimeters [120–122].

Part one of the my dissertation consists of Chapter 2 to 5, including the application of the finite temperature Green's function method to the investigation of the optical properties, or say electron dynamics, of nanoparticles. A brief review of the quantum field theory at finite temperature is made in Chapter 2.1, for later use in this work. In Chapter 2, we develop the real-space Green's function at finite temperature for any spherically symmetric system within the framework of so-called DRPA. Also in this chapter, by using the angular momentum coupling theory, the angular parts of these field equations are separated and only leave the radial parts for consideration, which dramatically reduces the computation strength. Two radial Dyson equations of Green's function and the nonlocalized screening electronic interaction potentials are derived, respectively. The finite element forms of these self-consistent iteration equations are built in Chapter 3. The linear response theory is setup in Chapter 4 to compute the susceptibility and the polarizability. Chapter 5 gives the examples on the application of the approaches created in the previously chapters. Part two of my dissertation appears in Chapter 6, included are our results on the electron and phonon transport through curved nanowires which is in the manuscript style. In Sec. 6.2 we carry out the above analysis for the two-dimensional Helmholtz equation. In Sec. 6.3 we consider electron transport through a circular right-angle bend, recovering results obtained by Sols and Macucci [106] and by Lin and Jaffe [107] using mode-matching methods. Our main results are given in Sec. 6.4, where we address thermal transport through curved wires. Sec. 6.5 contains a discussion of our conclusions and the experimental implications of this work. In part three of my dissertation, *i.e.*, Chapter 7, presented is the result for hot-electrons in low-dimensional phonon systems which is in the manuscript style. The conclusions are in Chapter 8.

CHAPTER 2

REAL SPACE GREEN'S FUNCTION FOR SPHERICALLY SYMMETRIC SYSTEMS

2.1 SELF-CONSISTENT DRESSED RANDOM PHASE APPROXIMATION AT FINITE TEMPERATURE

Condensed matter systems usually consist of many interacting particles. A complete understanding of such systems, involving solution of the many-particle Schrödinger equation, requires the knowledge of the interaction potential between particles, *i.e.*, the Hamiltonian

$$H = H_0 + H_V \quad (2.1)$$

with

$$H_0 \equiv \sum_{i=1} \left[-\frac{\hbar^2 \nabla^2}{2m_e} + U(\mathbf{r}_i) \right], \quad H_V \equiv \frac{1}{2} \sum_{i,j} V(\mathbf{r}_i, \mathbf{r}_j)$$

where H_0 includes the kinetic energy and some single-particle potential $U(\mathbf{r})$ felt by particles, and H_V is the mutual interaction between particles themselves. It is impossible to directly solve the corresponding many-particle coupling Schrödinger equations even for finite many-body systems, such as atoms and nuclei. Therefore other techniques are invoked instead, such as quantum field theory and Green's function methods [61–63]. The Green's function method has proved itself a very powerful tool. The finite temperature counterpart of the Green's function method was originated by Matsubara [64]. It includes the temperature in a natural way, and provides us with both the complete ground state and the excited state properties of the system. Since the Green's function method is formulated in the language of quantum field theory, we need to introduce the second quantization form of the Hamiltonian

$$\hat{H} = \hat{H}_0 + \hat{H}_V \quad (2.2)$$

$$\hat{H}_0 = \sum_{\alpha} \int d^3\mathbf{r} \hat{\Psi}_{\alpha}^{\dagger}(\mathbf{r}) \left[-\frac{\hbar^2 \nabla^2}{2m_e} + U(\mathbf{r}) \right] \hat{\Psi}_{\alpha}(\mathbf{r}) \quad (2.3)$$

$$\hat{H}_V = \frac{1}{2} \sum_{\alpha\alpha'} \int \int d^3\mathbf{r} d^3\mathbf{r}' \hat{\Psi}_{\alpha}^{\dagger}(\mathbf{r}) \hat{\Psi}_{\alpha'}^{\dagger}(\mathbf{r}') V(\mathbf{r}, \mathbf{r}') \hat{\Psi}_{\alpha'}(\mathbf{r}') \hat{\Psi}_{\alpha}(\mathbf{r}) \quad (2.4)$$

where $\hat{\Psi}_\alpha(\mathbf{r})$ and $\hat{\Psi}_\alpha^\dagger(\mathbf{r})$ are the field operators, eliminating and creating, respectively, particles at position \mathbf{r} with spin z component α .

The field operators satisfy simple commutation or anticommutation relations depending on whether the particle is boson or fermion,

$$\begin{aligned} \left[\hat{\Psi}_\alpha(\mathbf{r}), \hat{\Psi}_{\alpha'}^\dagger(\mathbf{r}') \right]_{\mp} &= \delta_{\alpha\alpha'} \delta(\mathbf{r} - \mathbf{r}') \\ \left[\hat{\Psi}_\alpha(\mathbf{r}), \hat{\Psi}_{\alpha'}(\mathbf{r}') \right]_{\mp} &= \left[\hat{\Psi}_\alpha^\dagger(\mathbf{r}), \hat{\Psi}_{\alpha'}^\dagger(\mathbf{r}') \right]_{\mp} = 0 \end{aligned} \quad (2.5)$$

where the upper (lower) sign refers to bosons (fermions).

In treating system at finite temperature, the grand canonical ensemble is often employed by introducing the grand canonical Hamiltonian,

$$\hat{K} = \hat{H} - \mu \hat{N} \quad (2.6)$$

where μ is the chemical potential, and \hat{N} is the particle number operator. The statistical operator and the grand partition function may be written as

$$\hat{\rho}_G = Z_G^{-1} e^{-\beta \hat{K}} = e^{-\beta(\Omega - \hat{K})} \quad (2.7)$$

$$Z_G = e^{-\Omega} = \text{Tr} e^{-\beta \hat{K}} \quad (2.8)$$

where Ω is the grand canonical potential, and $\beta = 1/k_B T$.

It is very convenient to work in the imaginary-time Heisenberg picture, in which any operator \hat{O} is related to its Schrödinger counterpart by

$$\hat{O}_K \equiv e^{\hat{K}\tau/\hbar} \hat{O}_S e^{-\hat{K}\tau/\hbar} \quad (2.9)$$

The representation of the field operators in this Heisenberg picture reads,

$$\hat{\Psi}_{K\alpha}(\mathbf{r}\tau) = e^{\hat{K}\tau/\hbar} \hat{\Psi}_\alpha(\mathbf{r}) e^{-\hat{K}\tau/\hbar} \quad (2.10)$$

$$\hat{\Psi}_{K\alpha}^\dagger(\mathbf{r}\tau) = e^{\hat{K}\tau/\hbar} \hat{\Psi}_\alpha^\dagger(\mathbf{r}) e^{-\hat{K}\tau/\hbar} \quad (2.11)$$

We should emphasize that $\hat{\Psi}_{K\alpha}^\dagger(\mathbf{r}\tau)$ is not the adjoint of $\hat{\Psi}_{K\alpha}(\mathbf{r}\tau)$ as long as τ is real. Actually, it can be analytically continued to a pure imaginary value it . As a result, $\hat{\Psi}_{K\alpha}^\dagger(\mathbf{r}, it)$ becomes the true adjoint of $\hat{\Psi}_{K\alpha}(\mathbf{r}, it)$ as in the original Heisenberg picture.

Now we give the definition of the single-particle Green's function as follows,

$$\mathcal{G}_{\alpha\alpha'}(\mathbf{r}\tau, \mathbf{r}'\tau') \equiv -\text{Tr} \left\{ \hat{\rho}_G T_\tau \left[\hat{\Psi}_{K\alpha}(\mathbf{r}\tau) \hat{\Psi}_{K\alpha'}^\dagger(\mathbf{r}'\tau') \right] \right\} \quad (2.12)$$

Here, T_τ is an operator that orders the operators following itself in such a way so that the one with the earlier time appears at the right, and also confines the sign of this operation by $(-1)^P$, where P is the number of permutations required by fermion operators to restore the original order. The trace (Tr) here implies the grand canonical ensemble average, or say the weighted average over a complete set of states in the Hilbert space, and the statistical operator plays a role of the weight. A simple calculation, with the help of the cyclic property of the trace [$\text{Tr}(ABC)=\text{Tr}(BCA)=\text{Tr}(CAB)$], gives the periodicity of the temperature Green's function

$$\begin{aligned} \mathcal{G}_{\alpha\alpha'}(\mathbf{r}\tau, \mathbf{r}'\tau') &= \pm \mathcal{G}_{\alpha\alpha'}[\mathbf{r}\tau, \mathbf{r}'(\tau' + \beta\hbar)] \\ \mathcal{G}_{\alpha\alpha'}(\mathbf{r}\tau, \mathbf{r}'\tau') &= \pm \mathcal{G}_{\alpha\alpha'}[\mathbf{r}(\tau + \beta\hbar), \mathbf{r}'\tau'] \end{aligned} \quad (2.13)$$

Therefore, one needs only consider the Green's function in the imaginary time domain $[0, \beta\hbar]$. Further simplification is reached when the Hamiltonian is time independent, where the Green's function is dependent only on the difference $\tau - \tau'$. One may simply write it as $\mathcal{G}_{\alpha\alpha'}(\mathbf{r}, \mathbf{r}'; \tau)$, and the periodic condition as

$$\mathcal{G}_{\alpha\alpha'}(\mathbf{r}, \mathbf{r}'; \tau < 0) = \pm \mathcal{G}_{\alpha\alpha'}(\mathbf{r}, \mathbf{r}'; \tau + \beta\hbar) \quad (2.14)$$

Nevertheless, this property enable us to get the finite temperature Green's function in the domain of the Matsubara imaginary frequency through the Fourier transformation

$$\begin{aligned} \mathcal{G}_{\alpha\alpha'}(\mathbf{r}, \mathbf{r}'; i\omega_n) &= \int_0^{\beta\hbar} d\tau e^{i\omega_n\tau} \mathcal{G}_{\alpha\alpha'}(\mathbf{r}, \mathbf{r}'; \tau) \\ \mathcal{G}_{\alpha\alpha'}(\mathbf{r}, \mathbf{r}'; \tau) &= \frac{1}{\beta\hbar} \sum_{i\omega_n} e^{-i\omega_n\tau} \mathcal{G}_{\alpha\alpha'}(\mathbf{r}, \mathbf{r}'; i\omega_n) \end{aligned} \quad (2.15)$$

where $i\omega_n$ is odd Matsubara frequency defined by

$$\omega_n \equiv \begin{cases} \frac{2n\pi}{\beta\hbar}, & \text{for bosons} \\ \frac{(2n+1)\pi}{\beta\hbar}, & \text{for fermions} \end{cases} \quad (2.16)$$

As long as Green's function is obtained, one can, in principle, calculate all the thermodynamics properties, such as the mean particle density and particle number, *i.e.*,

$$\langle \hat{n}(\mathbf{r}) \rangle = \mp \text{tr} \mathcal{G}(\mathbf{r}\tau, \mathbf{r}\tau^+) = \mp \sum_{\alpha} \mathcal{G}_{\alpha\alpha}(\mathbf{r}\tau, \mathbf{r}\tau^+) \quad (2.17)$$

$$N(T, V, \mu) = \mp \int \text{tr} \mathcal{G}(\mathbf{r}\tau, \mathbf{r}\tau^+) \quad (2.18)$$

To get a close form of the Green's function is very complicated because we do not know exactly the eigenstates of the corresponding Hamiltonian in many occasions. Hence the perturbation expansion is a tool to choose, in which one usually decomposes the full grand canonical Hamiltonian into an easily treated part \hat{K}_0 and a perturbation part $\hat{K}_1 = \hat{K} - \hat{K}_0$. Our discussion is then within the interaction picture. The representation of any mechanical operator in this picture is defined by

$$\hat{O}_I(\tau) \equiv e^{\hat{K}_0\tau/\hbar} \hat{O}_S e^{-\hat{K}_0\tau/\hbar} \quad (2.19)$$

It is related to its counterpart in the Heisenberg picture by

$$\hat{O}_K = \hat{\mathcal{U}}(0, \tau) \hat{O}_I(\tau) \hat{\mathcal{U}}(\tau, 0) \quad (2.20)$$

where the evolution operator can be easily obtained by formally solving its dynamical equation, *i.e.*,

$$\hat{\mathcal{U}}(\tau, \tau') = \sum_{n=0}^{\infty} \frac{1}{(-\hbar)^n n!} \int_{\tau'}^{\tau} d\tau_1 \cdots \int_{\tau'}^{\tau} d\tau_n T_{\tau} [\hat{K}_1(\tau_1) \cdots \hat{K}_n(\tau_n)] \quad (2.21)$$

Now the exact temperature Green's function, based upon the procedures mentioned above, can be calculated by the following perturbation expansion

$$\begin{aligned} \mathcal{G}_{\alpha\alpha'}(\mathbf{r}\tau, \mathbf{r}'\tau') = & \frac{-\text{Tr} \left\{ e^{-\beta\hat{K}_0} \sum_{n=0}^{\infty} (-\hbar)^{-n} \frac{1}{n!} \int_0^{\beta\hbar} d\tau_1 \cdots \int_0^{\beta\hbar} d\tau_n T_{\tau} \left[\hat{K}_1(\tau_1) \cdots \hat{K}_n(\tau_n) \hat{\Psi}_{I\alpha}(\mathbf{r}\tau) \hat{\Psi}_{I\alpha}^{\dagger}(\mathbf{r}'\tau') \right] \right\}}{\text{Tr} \left\{ e^{-\beta\hat{K}_0} \sum_{n=0}^{\infty} (-\hbar)^{-n} \frac{1}{n!} \int_0^{\beta\hbar} d\tau_1 \cdots \int_0^{\beta\hbar} d\tau_n T_{\tau} \left[\hat{K}_1(\tau_1) \cdots \hat{K}_n(\tau_n) \right] \right\}} \end{aligned} \quad (2.22)$$

Feynman diagram technique and Wick's theorem provide us with very efficient tools to evaluate the finite temperature Green's function. The diagram analysis shows that the denominator of equation (2.22) exactly cancels out the disconnect diagram in the nominator. Thus it reduces to,

$$\begin{aligned} \mathcal{G}_{\alpha\alpha'}(\mathbf{r}\tau, \mathbf{r}'\tau') = & - \sum_{n=0}^{\infty} \frac{1}{(-\hbar)^n n!} \int_0^{\beta\hbar} d\tau_1 \cdots \int_0^{\beta\hbar} d\tau_n \\ & \times \text{Tr} \left\{ e^{-\beta\hat{K}_0} T_{\tau} \left[\hat{K}_1(\tau_1) \cdots \hat{K}_n(\tau_n) \hat{\Psi}_{\alpha}(\mathbf{r}\tau) \hat{\Psi}_{\alpha}^{\dagger}(\mathbf{r}'\tau') \right] \right\}_{\text{connected}} \end{aligned} \quad (2.23)$$

Here the field operators $\hat{\Psi}_\alpha(\mathbf{r}\tau)$ and $\hat{\Psi}_\alpha^\dagger(\mathbf{r}'\tau')$ are associated with the unperturbed Hamiltonian \hat{K}_0 (due to the nature of the interaction picture). Thus the Green's function estimation is just to add up all the connected diagrams according to Feynman rules [61], which expresses the full Green's function in terms of the unperturbed ones, $\mathcal{G}_{\alpha\alpha'}^0(\mathbf{r}\tau, \mathbf{r}'\tau')$, associated with the Hamiltonian \hat{K}_0 .

For electron systems in solid, the Hamiltonian H_0 in the Eq.(2.3) takes the place of the grand canonical Hamiltonian, replacing single-particle potential $U(\mathbf{r})$ with the potential built up by the positive background charges and absorbing $-\mu\hat{N}$ term. It is time independent. The two-body Coulomb interaction $V(\mathbf{r} - \mathbf{r}')$ between electrons is treated as the perturbation and hence we have

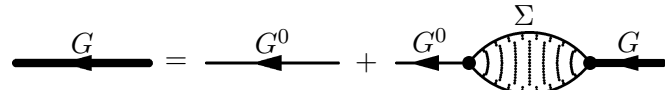
$$\hat{K}_1(\tau) = \frac{1}{2} \sum_{\alpha\alpha'} \int \int d^3\mathbf{r} d^3\mathbf{r}' \hat{\Psi}_{K\alpha}^\dagger(\mathbf{r}\tau) \hat{\Psi}_{K\alpha'}^\dagger(\mathbf{r}'\tau') V(\mathbf{r} - \mathbf{r}') \hat{\Psi}_{K\alpha'}(\mathbf{r}'\tau') \hat{\Psi}_{K\alpha}(\mathbf{r}\tau) \quad (2.24)$$

The Feynman rules corresponding to this interaction can be easily obtained. The Dyson equation provides a iteration method to self-consistently solve the Green's function through an unperturbed one. The Dyson equations for the Green's function reads

$$\mathcal{G}(\tilde{\mathbf{x}}, \tilde{\mathbf{y}}) = \mathcal{G}^0(\tilde{\mathbf{x}}, \tilde{\mathbf{y}}) + \int \int d\tilde{\mathbf{z}}_1 d\tilde{\mathbf{z}}_2 \mathcal{G}^0(\tilde{\mathbf{x}}, \tilde{\mathbf{z}}_1) \Sigma(\tilde{\mathbf{z}}_1, \tilde{\mathbf{z}}_2) \mathcal{G}(\tilde{\mathbf{z}}_2, \tilde{\mathbf{y}}) \quad (2.25)$$

where Σ is the proper self-energy in the self-consistent iterations [61]. Here we use the generalized coordinates representing the space, time and spin coordinates, *e.g.*, $\tilde{\mathbf{x}} = (\mathbf{x}, \tau_x, \alpha_x)$. The integrals include integrals over real space and imaginary time, and the summations over spin.

The diagrammatic representation of the Dyson for the temperature Green's function is shown in Fig.2.1. where the unperturbed Green's functions $\mathcal{G}_{\alpha\alpha'}^0(\mathbf{r}\tau, \mathbf{r}'\tau')$ are denoted by thin lines each



$$\text{Thick line with arrow } G = \text{Thin line with arrow } G^0 + \text{Thin line with arrow } G^0 \text{ --- } \text{Bulb } \Sigma \text{ --- Thick line with arrow } G \quad (2.26)$$

Figure 2.1: Diagrammatic Dyson equation for the finite temperature Green's function

with an arrow along the direction of $\mathbf{r} - \mathbf{r}'$, the perturbed (full or dressed) Green's functions $\mathcal{G}_{\alpha\alpha'}(\mathbf{r}\tau, \mathbf{r}'\tau')$ by thick lines with the same arrangement of the arrow directions as for G^0 . The proper self-energy diagrams [61] are denoted by filled bulbs. The solid circles on the vertexes imply the spin summations and the integrals over the space and time coordinates.

This diagram provides a self-consistent way to calculate the finite temperature Green's function, which will start to work as soon as one get the unperturbed Green's function G^0 . A typical approach is to solve the single-particle Schrödinger equation for the corresponding unperturbed first quantized Hamiltonian H_0 , and then construct the unperturbed Green's function by the following expression (for example, in the Matsubara frequency domain),

$$\mathcal{G}^0(\mathbf{r}, \mathbf{r}'; i\omega_n) = \sum_k \frac{\psi_k(\mathbf{r})\psi_k^*(\mathbf{r}')}{i\omega_n - E_k + \mu} \quad (2.27)$$

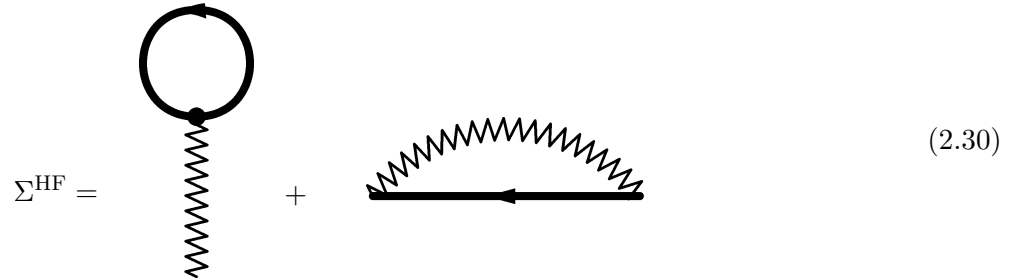
where $\psi_k(\mathbf{r})$ and E_k are respectively the eigenfunctions and eigenvalues of H_0 , and k denotes a set of quantum numbers. Alternatively, it can be obtained by directly solving the following equation

$$(i\omega_n - H_0 + \mu) \mathcal{G}^0(\mathbf{r}, \mathbf{r}'; i\omega_n) = \delta(\mathbf{r} - \mathbf{r}') \quad (2.28)$$

where μ is the chemical potential, and the single-particle Hamiltonian H_0 is defined as

$$H_0 \equiv \frac{\hbar^2 \nabla^2}{2m_e} + U(\mathbf{r}). \quad (2.29)$$

After an unperturbed Green's function is obtained, the next step is to compute the self-energy. Approximations are usually introduced at this stage. The very first ones are the Hartree and Fock approximations (the first order diagrams), shown in Fig.2.2, We have to emphasize that here we use



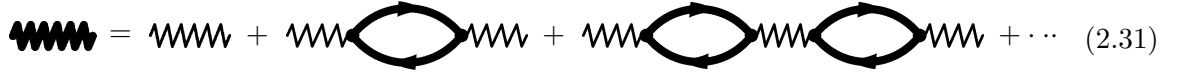
$$\Sigma^{\text{HF}} = \text{[Diagram 1]} + \text{[Diagram 2]} \quad (2.30)$$

Figure 2.2: Feynman diagram for the Hartree-Fock self-energy

the dressed Green's function instead of the unperturbed one because we confine ourself to the self-consistent computation in the current work. In many situations, the Hartree-Fock approximation gives rather good result, and at least provides a first insight into the problem under consideration.

In this research, we are interested in the polarization behavior of electrons, here the electron-hole excitation is important. Thus we need to add up all the contributions of the bulb diagrams as

shown in Fig.2.3. This is the random phase approximation (RPA) [61, 62, 65]. Here, again, we use the dressed Green's functions (the thick solid lines) instead of the unperturbed ones in all the bubble diagrams. This is why we call our approach the dressed-random-phase-approximation (DRPA). The DRPA contributes an effective two-body potential for electron-electron interactions, denoted by the thick zig-zag line, which is the result of the screening effect on the bare electron-electron interactions denoted by the thin zig-zag lines.



$$\text{thick wavy line} = \text{thin wavy line} + \text{thin wavy line} \text{---} \text{bubble} \text{---} \text{thin wavy line} + \text{thin wavy line} \text{---} \text{bubble} \text{---} \text{bubble} \text{---} \text{thin wavy line} + \dots \quad (2.31)$$

Figure 2.3: Ring approximation to the effective two-body interaction

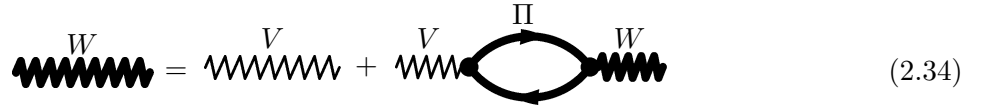
In a self-consistent way, one may get the Dyson equation for this effective potential [denoted analytically by the operator $W(\tilde{\mathbf{x}}, \tilde{\mathbf{y}})$],

$$W(\tilde{\mathbf{x}}, \tilde{\mathbf{y}}) = V(\tilde{\mathbf{x}}, \tilde{\mathbf{y}}) + \int \int d\tilde{\mathbf{z}}_1 d\tilde{\mathbf{z}}_2 V(\tilde{\mathbf{x}}, \tilde{\mathbf{z}}_1) \Pi(\tilde{\mathbf{z}}_1, \tilde{\mathbf{z}}_2) W(\tilde{\mathbf{z}}_2, \tilde{\mathbf{y}}) \quad (2.32)$$

with,

$$V(\tilde{\mathbf{x}}, \tilde{\mathbf{y}}) = V(\mathbf{x} - \mathbf{y}) \delta(\tau_x - \tau_y) \delta_{\alpha_x \alpha_y} \quad (2.33)$$

here the coordinates and the integrals are defined in the same way as in Eq.(2.25). The multiplication of the delta functions with respect to time and spin coordinates is due to the fact that the bare potential is independent of the time and spin. $\Pi(\tilde{\mathbf{z}}_1, \tilde{\mathbf{z}}_2)$ is the polarization operator. The definition of it can be found in the diagrammatic Dyson equation in Eq.(2.34),



$$\text{thick wavy line } W = \text{thin wavy line } V + \text{thin wavy line } V \text{---} \text{bubble} \text{---} \text{thick wavy line } W \quad (2.34)$$

Figure 2.4: Diagrammatic Dyson equation for the effective two-body interaction

Now we are ready to evaluate the self-energy associated this effective potential. We call this self-energy “RPA self-energy” in this dissertation because the effective potential is obtained under

the RPA. The Feynman diagram is shown in Fig.2.5. Here we subtract the Fock self-energy because its contribution has already been included previously in Eq.(2.30).

$$\Sigma^R = \text{[Diagram 1]} - \text{[Diagram 2]} \quad (2.35)$$

Figure 2.5: Feynman diagram for the self-energy in DRPA approximation

In our current approach we only include the Hartree-Fock and the RPA self-energy, *i.e.*,

$$\Sigma(\tilde{z}_1, \tilde{z}_2) = \Sigma^{\text{HF}}(\tilde{z}_1, \tilde{z}_2) + \Sigma^R(\tilde{z}_1, \tilde{z}_2) \quad (2.36)$$

Substitute this self-energy into Dyson equation (2.25), we obtain a dressed Green's function, which ends our first iteration. With this Green's function, we start next sequence of computing effective potential via Eq.(2.32), Hartree-Fock self-energy via Eq.(2.30), RPA self-energy via Eq.(2.35) and finally the dressed Green's function via Eq.(2.25). Repeating the above sequence till a required precision is reached, one may get the Green's function of the system. Based upon this finite temperature Green's function, one may calculate any interesting physical properties.

2.2 SPHERICALLY SYMMETRIC SYSTEMS AND RADIAL GREEN'S FUNCTION

In developing the self-consistent dressed random phase approximation in the previous section, no pre-assumption is made on the nature of electron systems excepting the time-independence of the Hamiltonian. We provide only a general framework of DRPA for computing the finite temperature Green's function of interacting electron systems confined in some background potential $U(\mathbf{r})$ [see eq.(2.3)]. The description will become simpler if there is some special symmetry for the system, for example, the translation invariance in the homogeneous systems. One may use Fourier transformation to transfer the current formula into momentum space when this happens. The description in this space becomes pretty simple (comparing to real space case). However, the objectives of the current research are nanoparticles lack of translation symmetry, especially for small nanoparticles. In a very rough approximation, one may assume a spherical symmetry. Actually, for the so called

close-shell metallic nanoparticles consisting of magic number of atoms, spherical symmetry is often used to simplify the problems [6, 7, 17, 18, 23, 36–40].

In the following sections, we assume the spherical symmetry for our electron system. As a result, the background potential $U(\mathbf{r})$ are only determined by the position with no relation to the angular coordinates, *i.e.*,

$$U(\mathbf{r}) = U(r)$$

Now the angular quantum number is a good quantum number, one may make use of all batch of methods developed in the angular momentum theory [66]. The first step is to separate the angular portion from the radial coordinate. By using the spherical harmonic function, one expands the two-body Coulomb potential as

$$V(\mathbf{r} - \mathbf{r}') = \frac{e^2}{|\mathbf{r} - \mathbf{r}'|} = \sum_{l=0}^{\infty} \sum_{m=-l}^{m=l} F_l(r, r') Y_{lm}^*(\theta', \varphi') Y_{lm}(\theta, \varphi) \quad (2.37)$$

with

$$F_l(r, r') \equiv \frac{4\pi\phi_0}{2l+1} \frac{q_{<}^l}{q_{>}^{l+1}} \quad (2.38)$$

and

$$\phi_0 \equiv \frac{e^2}{r_s}, \quad q_{<} \equiv \min\{q, q'\}, \quad q_{>} \equiv \max\{q, q'\}, \quad q \equiv \frac{r}{r_s},$$

where r_s is the Wigner-Seitz radius of electrons in bulk materials, which is used to rescale the length through out this work.

Similarly, one may expand the Fermion field operators (in the Heisenberg picture) as,

$$\hat{\Psi}_{\alpha}(\mathbf{r}, \tau) = \sum_{\mu} \Phi_{n_{\mu}l_{\mu}}(r) Y_{l_{\mu}m_{\mu}}(\theta, \varphi) C_{\mu\alpha}(\tau) \quad (2.39)$$

$$\hat{\Psi}_{\alpha}^{\dagger}(\mathbf{r}, \tau) = \sum_{\mu} \Phi_{n_{\mu}l_{\mu}}(r) Y_{l_{\mu}m_{\mu}}^*(\theta, \varphi) C_{\mu\alpha}^{\dagger}(\tau) \quad (2.40)$$

where, $C_{\mu\alpha}(\tau)$ and $C_{\mu\alpha}^{\dagger}$ are the creation and destruction operators in Heisenberg picture, respectively. α is the spin index. n_{μ}, l_{μ} and m_{μ} are the principal, angular and magnetic quantum number, respectively, and μ is the abbreviation of them, *i.e.*, $\mu \equiv \{n_{\mu}, l_{\mu}, m_{\mu}\}$. Substitute them in the definition of the finite temperature, Eq.(2.12), the following expansion is obtained,

$$\mathcal{G}_{\alpha\alpha'}(\mathbf{r}, \mathbf{r}'; \tau) = \sum_{\mu\mu'} Y_{l_{\mu}m_{\mu}}(\theta, \varphi) Y_{l_{\mu'}m_{\mu'}}^*(\theta', \varphi') \Phi_{n_{\mu}l_{\mu}}(r) \Phi_{n_{\mu'}l_{\mu'}}(r') \mathcal{G}_{\alpha\alpha'}(\mu, \mu'; \tau) \quad (2.41)$$

where

$$\mathcal{G}_{\alpha\alpha'}(\mu, \mu'; \tau) \equiv -\text{Tr} \left\{ \hat{\rho}_G T_\tau \left[C_{\mu\alpha}^\dagger(\tau) C_{\mu'\alpha'}^\dagger(0) \right] \right\} \quad (2.42)$$

It can be shown that $\mathcal{G}_{\alpha\alpha'}(\mu, \mu'; \tau)$ is diagonal with respect to l_μ and m_μ , *i.e.*,

$$\mathcal{G}_{\alpha\alpha'}(\mu, \mu'; \tau) = \mathcal{G}(n_\mu | n_{\mu'}; l_\mu, \tau) \delta_{\alpha\alpha'} \delta_{l_\mu l_{\mu'}} \delta_{m_\mu m_{\mu'}} \quad (2.43)$$

Therefore, Eq.(2.41) becomes,

$$\mathcal{G}_{\alpha\alpha'}(\mathbf{r}, \mathbf{r}'; \tau) = \sum_{l_\mu m_\mu} Y_{l_\mu m_\mu}(\theta, \varphi) Y_{l_\mu m_\mu}^*(\theta', \varphi') \sum_{n_\mu n_{\mu'}} \Phi_{n_\mu l_\mu}(r) \Phi_{n_{\mu'} l_{\mu'}}(r') \mathcal{G}_{\alpha\alpha'}(n_\mu | n_{\mu'}; l_\mu, \tau) \quad (2.44)$$

Introducing the radial Green's function

$$G_{l_\mu}(r, r'; \tau) \equiv \sum_{n_\mu n_{\mu'}} \Phi_{n_\mu l_\mu}(r) \Phi_{n_{\mu'} l_{\mu'}}(r') \mathcal{G}(n_\mu | n_{\mu'}; l_\mu, \tau) \quad (2.45)$$

one may express the real-space Green's function by

$$\mathcal{G}_{\alpha\alpha'}(\mathbf{r}, \mathbf{r}'; \tau) = \sum_{l_\mu m_\mu} Y_{l_\mu m_\mu}(\theta, \varphi) Y_{l_\mu m_\mu}^*(\theta', \varphi') G_{l_\mu}(r, r'; \tau) \delta_{\alpha\alpha'} \quad (2.46)$$

The Fourier transformation defined in Eq.(2.15) yields,

$$\mathcal{G}_{\alpha\alpha'}(\mathbf{r}, \mathbf{r}'; i\omega_n) = \sum_{l_\mu m_\mu} Y_{l_\mu m_\mu}(\theta, \varphi) Y_{l_\mu m_\mu}^*(\theta', \varphi') G_{l_\mu}(r, r'; i\omega_n) \delta_{\alpha\alpha'} \quad (2.47)$$

$$G_{l_\mu}(r, r'; i\omega_n) \equiv \sum_{n_\mu n_{\mu'}} \Phi_{n_\mu l_\mu}(r) \Phi_{n_{\mu'} l_{\mu'}}(r') \mathcal{G}(n_\mu | n_{\mu'}; l_\mu, i\omega_n) \quad (2.48)$$

$$\mathcal{G}_{\alpha\alpha'}(\mu, \mu'; i\omega_n) = \mathcal{G}(n_\mu | n_{\mu'}; l_\mu, i\omega_n) \delta_{\alpha\alpha'} \delta_{l_\mu l_{\mu'}} \delta_{m_\mu m_{\mu'}} \quad (2.49)$$

With the help of the spherical harmonic functions, the temperature Green's function has been successfully decomposed into the multiplication of the angular and the radial parts, which will enable us to separate the angular part completely. The similar derivations will be applied to the self-energy, polarization operator, and the screening potential separately in the following sections.

2.3 HARTREE SELF-ENERGY

According to the Feynman rules and the definition of self-energy in Eq.(2.30), one writes the Hartree self-energy as

$$\begin{aligned}\Sigma^H(\mathbf{r}, \mathbf{r}') &= \frac{(2s+1)}{\beta\hbar^2} \delta(\mathbf{r} - \mathbf{r}') \int d^3\mathbf{r}_0 V(\mathbf{r} - \mathbf{r}_0) \sum_{i\omega_n} e^{i\omega_n\eta} \mathcal{G}(\mathbf{r}_0, \mathbf{r}_0; i\omega_n) \\ &= \delta(\mathbf{r} - \mathbf{r}') \tilde{\Sigma}^H(\mathbf{r})\end{aligned}\quad (2.50)$$

where,

$$\tilde{\Sigma}^H(\mathbf{r}) = \frac{(2s+1)}{\beta\hbar^2} \int d^3\mathbf{r}_0 V(\mathbf{r} - \mathbf{r}_0) \sum_{i\omega_n} e^{i\omega_n\eta} \mathcal{G}(\mathbf{r}_0, \mathbf{r}_0; i\omega_n) \quad (2.51)$$

Substituting the expression of the Coulomb potential (2.37) and Eq.(2.47), it becomes

$$\begin{aligned}\tilde{\Sigma}^H(\mathbf{r}) &= \frac{(2s+1)}{\beta\hbar^2} \sum_{lm} \sum_{l'm'} \int d^3\mathbf{r}_0 F_l(r, r_0) Y_{lm}^*(\theta, \varphi) Y_{lm}(\theta_0, \varphi_0) Y_{l'm'}(\theta_0, \varphi_0) Y_{l'm'}^*(\theta_0, \varphi_0) \\ &\quad \sum_{i\omega_n} e^{i\omega_n\eta} G_{l'}(r_0, r_0; i\omega_n)\end{aligned}$$

Integrating the angular part through relation (A.10), we have

$$\begin{aligned}\tilde{\Sigma}^H(\mathbf{r}) &= \frac{(2s+1)}{\beta\hbar^2} \sum_{lm} \sum_{l'm'} \int r_0^2 dr_0 \sqrt{\frac{(2l'+1)}{4\pi}} F_l(r, r_0) Y_{lm}^*(\theta, \varphi) \tilde{C}(ll'l'; mm'm') C(ll'l'; 000) \\ &\quad \sum_{i\omega_n} e^{i\omega_n\eta} G_{l'}(r_0, r_0; i\omega_n)\end{aligned}$$

Summing over m and over m' using relation (A.12), and then over l , it becomes

$$\tilde{\Sigma}^H(\mathbf{r}) = \frac{(2s+1)}{\sqrt{4\pi}\beta\hbar^2} \sum_{l'} \int r_0^2 dr_0 (2l'+1) F_0(r, r_0) Y_{00}^*(\theta, \varphi) C(0l'l'; 000) \sum_{i\omega_n} e^{i\omega_n\eta} G_{l'}(r_0, r_0; i\omega_n)$$

With $C(0l'l'; 000) = 1$ and $Y_{00}^*(\theta, \varphi) = 1/\sqrt{4\pi}$, we get

$$\tilde{\Sigma}^H(\mathbf{r}) = \frac{(2s+1)}{4\pi\beta\hbar^2} \sum_{l'} \int r_0^2 dr_0 (2l'+1) F_0(r, r_0) \sum_{i\omega_n} e^{i\omega_n\eta} G_{l'}(r_0, r_0; i\omega_n)$$

Clearly $\tilde{\Sigma}^H(\mathbf{r})$ is not angular dependent, and can be expressed as,

$$\tilde{\Sigma}^H(r) = \frac{(2s+1)k_B T}{4\pi\hbar^2} \sum_{l'} \int r_0^2 dr_0 (2l'+1) F_0(r, r_0) \sum_{i\omega_n} e^{i\omega_n\eta} G_{l'}(r_0, r_0; i\omega_n) \quad (2.52)$$

and the radial Hartree self-energy is

$$\Sigma^H(r, r') = \frac{1}{r^2} \delta(r - r') \tilde{\Sigma}^H(r) \quad (2.53)$$

The partial Green's function corresponding to the Hartree self-energy can be expressed as

$$\begin{aligned}
\mathcal{G}^H(\mathbf{r}, \mathbf{r}'; i\Omega_n) &= \int d^3\mathbf{r}_1 d^3\mathbf{r}'_1 \mathcal{G}^0(\mathbf{r}, \mathbf{r}_1; i\Omega_n) \Sigma^H(\mathbf{r}_1, \mathbf{r}'_1) \mathcal{G}(\mathbf{r}'_1, \mathbf{r}'; i\Omega_n) \\
&= \int d^3\mathbf{r}_1 \mathcal{G}^0(\mathbf{r}, \mathbf{r}_1; i\Omega_n) \tilde{\Sigma}^H(r_1) \mathcal{G}(\mathbf{r}_1, \mathbf{r}'; i\Omega_n) \\
&= \sum_{lm} \sum_{l'm'} \int d^3\mathbf{r}_1 Y_{lm}(\theta, \varphi) \mathcal{G}_l^0(r, r_1; i\Omega_n) Y_{lm}^*(\theta_1, \varphi_1) Y_{l'm'}^*(\theta_1, \varphi_1) \\
&\quad \tilde{\Sigma}^H(r_1) \mathcal{G}_{l'}(r_1, r'; i\Omega_n) Y_{l'm'}(\theta', \varphi')
\end{aligned}$$

Integrating the angular part using the orthonormal relation of the spherical harmonic functions, we have

$$\mathcal{G}^H(\mathbf{r}, \mathbf{r}'; i\Omega_n) = \sum_{lm} Y_{lm}(\theta, \varphi) Y_{lm}^*(\theta', \varphi') G_l(r, r'; i\Omega_n) \quad (2.54)$$

where the radial Green's function reads,

$$G_l^H(r, r'; i\Omega_n) = \int r_1^2 dr_1 G_l^0(r, r_1; i\Omega_n) \tilde{\Sigma}^H(r_1) G_l(r_1, r'; i\Omega_n) \quad (2.55)$$

2.4 FOCK SELF-ENERGY

The Fock self-energy and the corresponding partial Green's function are defined by

$$\Sigma^F(\mathbf{r}, \mathbf{r}') = -\frac{1}{\beta\hbar^2} V(\mathbf{r} - \mathbf{r}') \sum_{i\omega_n} e^{i\omega_n\eta} \mathcal{G}(\mathbf{r}, \mathbf{r}'; i\omega_n) \quad (2.56)$$

$$\mathcal{G}^F(\mathbf{r}, \mathbf{r}'; i\Omega_n) = \int d^3\mathbf{r}_1 d^3\mathbf{r}_2 \mathcal{G}^0(\mathbf{r}, \mathbf{r}_1; i\Omega_n) \Sigma^F(\mathbf{r}_1, \mathbf{r}_2) \mathcal{G}(\mathbf{r}_2, \mathbf{r}'; i\Omega_n) \quad (2.57)$$

Substituting the expression of the Coulomb potential (2.37) and Eq.(2.47) into Eq.(2.56), one has

$$\begin{aligned}
\Sigma^F(\mathbf{r}, \mathbf{r}') &= -\frac{1}{\beta\hbar^2} \sum_{l_1 m_1} \sum_{l_2 m_2} Y_{l_1 m_1}(\theta, \varphi) Y_{l_2 m_2}(\theta, \varphi) Y_{l_1 m_1}^*(\theta', \varphi') Y_{l_2 m_2}^*(\theta', \varphi') F_{l_1}(r, r') \\
&\quad \sum_{i\omega_n} e^{i\omega_n\eta} G_{l_2}(r, r'; i\omega_n)
\end{aligned}$$

According to Eq.(A.9), coupling of the spherically harmonic functions gives,

$$\begin{aligned}
\Sigma^F(\mathbf{r}, \mathbf{r}') &= -\frac{1}{\beta\hbar^2} \sum_{lm} \sum_{l'm'} \sum_{l_1 l_2} \frac{2l_2 + 1}{4\pi} Y_{lm}(\theta, \varphi) Y_{l'm'}^*(\theta', \varphi') F_{l_1}(r, r') C(l_1 l_2 l) C(l_1 l_2 l') \\
&\quad \sum_{i\omega_n} e^{i\omega_n\eta} G_{l_2}(r, r'; i\omega_n) \sum_{m_1 m_2} \tilde{C}(l_1 l_2 l; m_1 m_2 m) \tilde{C}(l_1 l_2 l'; m_1 m_2 m')
\end{aligned}$$

Summing over $m_1 m_2$ using the orthonormal relation (A.7), and then the summation over $l' m'$ gives,

$$\Sigma^F(\mathbf{r}, \mathbf{r}') = \sum_{lm} Y_{lm}(\theta, \varphi) Y_{lm}^*(\theta', \varphi') \Sigma_l^F(r, r') \quad (2.58)$$

where the radial Fock self-energy is

$$\Sigma_l^F(r, r') \equiv -\frac{k_B T}{4\pi(2l+1)\hbar^2} \sum_{l_1 l_2} (2l_1+1)(2l_2+1) F_{l_1}(r, r') C(l_1 l_2 l)^2 \sum_{i\omega_n} e^{i\omega_n \eta} G_{l_2}(r, r'; i\omega_n)$$

To obtain the corresponding partial radial Green's function, we substitute Eq. (2.58) and (2.47) into (2.57), and get

$$\begin{aligned} \mathcal{G}^F(\mathbf{r}, \mathbf{r}'; i\Omega_n) &= \sum_{lm} \sum_{l'_1 m'_1} \sum_{l'_2 m'_2} \int d^3\mathbf{r}_1 d^3\mathbf{r}_2 Y_{l'_1 m'_1}(\theta, \varphi) G_{l'_1}^0(r, r_1; i\Omega_n) Y_{l'_1 m'_1}^*(\theta_1, \varphi_1) Y_{lm}(\theta_1, \varphi_1) \\ &\quad \Sigma_l^F(r_1, r_2) Y_{lm}^*(\theta_2, \varphi_2) Y_{l'_2 m'_2}(\theta_2, \varphi_2) G_{l'_2}(r_2, r'; i\Omega_n) Y_{l'_2 m'_2}^*(\theta', \varphi') \end{aligned}$$

Integrating the angular parts using the orthonormal relation of the spherically harmonic function, and then sum over $l'_1 m'_1$ and $l'_2 m'_2$, we obtain

$$\mathcal{G}^F(\mathbf{r}, \mathbf{r}'; i\Omega_n) = \sum_{lm} Y_{lm}(\theta, \varphi) Y_{lm}^*(\theta', \varphi') G_l^F(r, r'; i\Omega_n) \quad (2.59)$$

and the radial counterpart

$$G_l^F(r, r'; i\Omega_n) = \int r_1^2 dr_1 r_2^2 dr_2 G_l^0(r, r_1; i\Omega_n) \Sigma_l^F(r_1, r_2) G_l(r_2, r'; i\Omega_n) \quad (2.60)$$

2.5 POLARIZATION OPERATOR AND SCREENED POTENTIAL

The polarization operator is defined by,

$$\Pi(\mathbf{r}, \mathbf{r}'; ip_n) = \frac{(2s+1)}{\beta\hbar^2} \sum_{i\omega_n} \mathcal{G}(\mathbf{r}, \mathbf{r}'; i\omega_n) \mathcal{G}(\mathbf{r}', \mathbf{r}; i\omega_n - ip_n) \quad (2.61)$$

According to Eq. (2.47), it turns into

$$\begin{aligned} \Pi(\mathbf{r}, \mathbf{r}'; ip_n) &= \frac{(2s+1)}{\beta\hbar^2} \sum_{l_1 m_1} \sum_{l_2 m_2} Y_{l_1 m_1}(\theta, \varphi) Y_{l_2 m_2}^*(\theta, \varphi) Y_{l_1 m_1}^*(\theta', \varphi') Y_{l_2 m_2}(\theta', \varphi') \\ &\quad \sum_{i\omega_n} G_{l_1}(r, r'; i\omega_n) G_{l_2}(r', r; i\omega_n - ip_n) \end{aligned}$$

Employing the coupling rule of the spherical harmonics, we get

$$\begin{aligned}\Pi(\mathbf{r}, \mathbf{r}'; ip_n) &= \frac{(2s+1)}{4\pi\beta\hbar^2} \sum_{lm} \sum_{l'm'} \sum_{l_1 m_1} \sum_{l_2 m_2} (2l_2+1) (-1)^{m_1+m_2} \tilde{C}(l_1 l_2 l; m_1 - m_2 m) \\ &\quad \tilde{C}(l_1 l_2 l'; -m_1 m_2 m') Y_{lm}(\theta, \varphi) Y_{l'm'}(\theta', \varphi') C(l_1 l_2 l) C(l_1 l_2 l') \\ &\quad \sum_{i\omega_n} G_{l_1}(r, r'; i\omega_n) G_{l_2}(r', r; i\omega_n - ip_n)\end{aligned}$$

Since $l_1 + l_2 - l$ is even, one has $\tilde{C}(l_1 l_2 l; m_1 - m_2 m) = \tilde{C}(l_1 l_2 l; -m_1 m_2 - m)$, and the non-zero CG coefficient requires that $m = m_1 - m_2$. Thus, this equation becomes

$$\begin{aligned}\Pi(\mathbf{r}, \mathbf{r}'; ip_n) &= \frac{(2s+1)}{4\pi\beta\hbar^2} \sum_{lm} \sum_{l'm'} \sum_{l_1 m_1} \sum_{l_2 m_2} (2l_2+1) (-1)^m \tilde{C}(l_1 l_2 l; -m_1 m_2 - m) \\ &\quad \tilde{C}(l_1 l_2 l'; -m_1 m_2 m') Y_{lm}(\theta, \varphi) Y_{l'm'}(\theta', \varphi') C(l_1 l_2 l) C(l_1 l_2 l') \\ &\quad \sum_{i\omega_n} G_{l_1}(r, r'; i\omega_n) G_{l_2}(r', r; i\omega_n - ip_n)\end{aligned}$$

Sum over $m_1 m_2$ using the orthonormal relation (A.7), and then over $l' m'$, this equation becomes,

$$\begin{aligned}\Pi(\mathbf{r}, \mathbf{r}'; ip_n) &= \frac{(2s+1)}{4\pi\beta\hbar^2} \sum_{lm} \sum_{l_1 l_2} \frac{(2l_1+1)(2l_2+1)}{(2l+1)} Y_{lm}(\theta, \varphi) (-1)^m Y_{l-m}(\theta', \varphi') C(l_1 l_2 l)^2 \\ &\quad \sum_{i\omega_n} G_{l_1}(r, r'; i\omega_n) G_{l_2}(r', r; i\omega_n - ip_n) \\ &= \sum_{lm} Y_{lm}(\theta, \varphi) Y_{lm}^*(\theta', \varphi') \Pi_l(r, r'; ip_n)\end{aligned}\tag{2.62}$$

where,

$$\begin{aligned}\Pi_l(r, r'; ip_n) &= \frac{(2s+1)k_B T}{4\pi(2l+1)\hbar^2} \sum_{l_1 l_2} (2l_1+1)(2l_2+1) C(l_1 l_2 l)^2 \\ &\quad \sum_{i\omega_n} G_{l_1}(r, r'; i\omega_n) G_{l_2}(r', r; i\omega_n - ip_n)\end{aligned}\tag{2.63}$$

According to the Dyson equation (2.32), the screened Coulomb potential reads

$$W(\mathbf{r}, \mathbf{r}'; ip_n) = V(\mathbf{r}, \mathbf{r}') + \int \int d^3\mathbf{r}_1 d^3\mathbf{r}'_1 V(\mathbf{r}, \mathbf{r}_1) \Pi(\mathbf{r}_1, \mathbf{r}'_1; ip_n) W(\mathbf{r}'_1, \mathbf{r}'; ip_n)\tag{2.64}$$

To get the radial component, we let this integration equation evolve self-consistently. The zero-order potential is just the bare one defined in Eq.(2.37), *i.e.*,

$$W^{(0)}(\mathbf{r}, \mathbf{r}'; ip_n) = V(\mathbf{r}, \mathbf{r}') = \sum_{lm} Y_{lm}(\theta, \varphi) Y_{lm}^*(\theta', \varphi') W_l^{(0)}(\mathbf{r}, \mathbf{r}'; ip_n)\tag{2.65}$$

and thus

$$W_l^{(0)}(r, r'; ip_n) = F_l(r, r') \quad (2.66)$$

The first-order term is

$$\begin{aligned} W^{(1)}(\mathbf{r}, \mathbf{r}'; ip_n) &= \int d^3\mathbf{r}_1 d^3\mathbf{r}'_1 V(\mathbf{r}, \mathbf{r}_1) \Pi(\mathbf{r}_1, \mathbf{r}'_1; ip_n) W^{(0)}(\mathbf{r}'_1, \mathbf{r}'; ip_n) \\ &= \sum_{lm} \sum_{l_1 m_1} \sum_{l' m'} \int d^3\mathbf{r}_1 d^3\mathbf{r}'_1 Y_{lm}(\theta, \varphi) F_l(r, r_1) Y_{lm}^*(\theta_1, \varphi_1) Y_{l_1 m_1}(\theta_1, \varphi_1) \\ &\quad \Pi_{l_1}(r_1, r'_1; ip_n) Y_{l_1 m_1}^*(\theta'_1, \varphi'_1) Y_{l' m'}(\theta'_1, \varphi'_1) W^{(0)l'}(r'_1, r'; ip_n) Y_{l' m'}^*(\theta', \varphi') \end{aligned}$$

Integrating the angular parts via the orthonormal relation, it becomes,

$$\begin{aligned} W^{(1)}(\mathbf{r}, \mathbf{r}'; ip_n) &= \sum_{lm} \sum_{l_1 m_1} \sum_{l' m'} \int r_1^2 dr_1 r_1'^2 dr_1' Y_{lm}(\theta, \varphi) Y_{l' m'}^*(\theta', \varphi') F_l(r, r_1) \Pi_{l_1}(r_1, r'_1; ip_n) \\ &\quad W_{l'}^{(0)}(r'_1, r'; ip_n) \delta_{ll_1} \delta_{mm_1} \delta_{l_1 l'} \delta_{m_1 m'} \end{aligned}$$

Summation over $l_1 m_1 l' m'$ gives,

$$W^{(1)}(\mathbf{r}, \mathbf{r}'; ip_n) = \sum_{lm} Y_{lm}(\theta, \varphi) Y_{lm}^*(\theta', \varphi') W_l^{(1)}(r, r'; ip_n) \quad (2.67)$$

$$W_l^{(1)}(r, r'; ip_n) = \int r_1^2 dr_1 r_1'^2 dr_1' F_l(r, r_1) \Pi_l(r_1, r'_1; ip_n) W_l^{(0)}(r'_1, r'; ip_n) \quad (2.68)$$

Similarly, the second-order term is

$$\begin{aligned} W^{(2)}(\mathbf{r}, \mathbf{r}'; ip_n) &= \int d^3\mathbf{r}_1 d^3\mathbf{r}'_1 V(\mathbf{r}, \mathbf{r}_1) \Pi(\mathbf{r}_1, \mathbf{r}'_1; ip_n) W^{(1)}(\mathbf{r}'_1, \mathbf{r}'; ip_n) \\ &= \sum_{lm} \sum_{l_1 m_1} \sum_{l' m'} \int d^3\mathbf{r}_1 d^3\mathbf{r}'_1 Y_{lm}(\theta, \varphi) F_l(r, r_1) Y_{lm}^*(\theta_1, \varphi_1) Y_{l_1 m_1}(\theta_1, \varphi_1) \\ &\quad \Pi_{l_1}(r_1, r'_1; ip_n) Y_{l_1 m_1}^*(\theta'_1, \varphi'_1) Y_{l' m'}(\theta'_1, \varphi'_1) W_{l'}^{(1)}(r'_1, r'; ip_n) Y_{l' m'}^*(\theta', \varphi') \end{aligned}$$

Integrating the angular parts using the orthonormal relation of the spherical harmonics, and then summing over $l_1 m_1 l' m'$, we get,

$$W^{(2)}(\mathbf{r}, \mathbf{r}'; ip_n) = \sum_{lm} Y_{lm}(\theta, \varphi) Y_{lm}^*(\theta', \varphi') W_l^{(2)}(r, r'; ip_n) \quad (2.69)$$

$$W_l^{(2)}(r, r'; ip_n) = \int r_1^2 dr_1 r_1'^2 dr_1' F_l(r, r_1) \Pi_l(r_1, r'_1; ip_n) W_l^{(1)}(r'_1, r'; ip_n) \quad (2.70)$$

Suppose any n -th order term can be expressed as

$$W^{(n)}(\mathbf{r}, \mathbf{r}'; ip_n) = \sum_{lm} Y_{lm}(\theta, \varphi) Y_{lm}^*(\theta', \varphi') W_l^{(n)}(r, r'; ip_n) \quad (2.71)$$

Then, the $(n+1)$ -th order term reads,

$$\begin{aligned}
W^{(n+1)}(\mathbf{r}, \mathbf{r}'; ip_n) &= \int d^3\mathbf{r}_1 d^3\mathbf{r}'_1 V(\mathbf{r}, \mathbf{r}_1) \Pi(\mathbf{r}_1, \mathbf{r}'_1; ip_n) W^{(n)}(\mathbf{r}'_1, \mathbf{r}'; ip_n) \\
&= \sum_{lm} \sum_{l_1 m_1} \sum_{l' m'} \int d^3\mathbf{r}_1 d^3\mathbf{r}'_1 Y_{lm}(\theta, \varphi) F_l(r, r_1) Y_{lm}^*(\theta_1, \varphi_1) Y_{l_1 m_1}(\theta_1, \varphi_1) \\
&\quad \Pi_{l_1}(r_1, r'_1; ip_n) Y_{l_1 m_1}^*(\theta'_1, \varphi'_1) Y_{l' m'}(\theta'_1, \varphi'_1) W_{l'}^{(n)}(r'_1, r'; ip_n) Y_{l' m'}^*(\theta', \varphi')
\end{aligned}$$

Integrating the angular parts using the orthonormal relation of the spherical harmonics, and then summing over $l_1 m_1 l' m'$, we get,

$$W^{(n+1)}(\mathbf{r}, \mathbf{r}'; ip_n) = \sum_{lm} Y_{lm}(\theta, \varphi) Y_{lm}^*(\theta', \varphi') W_l^{(n+1)}(r, r'; ip_n) \quad (2.72)$$

$$W_l^{(n+1)}(r, r'; ip_n) = \int r_1^2 dr_1 r_1'^2 dr'_1 F_l(r, r_1) \Pi_l(r_1, r'_1; ip_n) W_l^{(n)}(r'_1, r'; ip_n) \quad (2.73)$$

Therefore, we have proved that the screen potential can be expressed as

$$W(\mathbf{r}, \mathbf{r}'; ip_n) = \sum_{lm} Y_{lm}(\theta, \varphi) Y_{lm}^*(\theta', \varphi') W_l(r, r'; ip_n) \quad (2.74)$$

$$W_l(r, r'; ip_n) = F_l(r, r') + \int r_1^2 dr_1 r_1'^2 dr'_1 F_l(r, r_1) \Pi_l(r_1, r'_1; ip_n) W_l(r'_1, r'; ip_n) \quad (2.75)$$

As the contribution of the bare potential has already been counted in Fock self-energy, we need to subtract it from the total potential. We denote the subtracted potential by ΔW . Clearly, it can also be expressed as,

$$\Delta W(\mathbf{r}, \mathbf{r}'; ip_n) = \sum_{lm} Y_{lm}(\theta, \varphi) Y_{lm}^*(\theta', \varphi') \Delta W_l(r, r'; ip_n) \quad (2.76)$$

$$\Delta W_l(r, r'; ip_n) = W_l(r, r'; ip_n) - F_l(r, r') \quad (2.77)$$

The self-energy and the partial Green's function associated with this random phase approximation can be written as

$$\Sigma^R(\mathbf{r}, \mathbf{r}'; i\Omega_n) = -\frac{1}{\beta \hbar^2} \sum_{ip_n} \Delta W(\mathbf{r}, \mathbf{r}'; ip_n) \mathcal{G}(\mathbf{r}, \mathbf{r}'; i\Omega - ip_n) \quad (2.78)$$

$$\mathcal{G}^R(\mathbf{r}, \mathbf{r}'; i\Omega_n) = \int d^3\mathbf{r}_1 d^3\mathbf{r}_2 \mathcal{G}^0(\mathbf{r}, \mathbf{r}_1; i\Omega_n) \Sigma^R(\mathbf{r}_1, \mathbf{r}_2; i\Omega_n) \mathcal{G}(\mathbf{r}_2, \mathbf{r}'; i\Omega_n) \quad (2.79)$$

Substituting the expression of the screen potential (2.76) and Eq.(2.47) into Eq.(2.78), one has

$$\begin{aligned} \Sigma^R(\mathbf{r}, \mathbf{r}'; i\Omega) &= -\frac{1}{\beta\hbar^2} \sum_{l_1 m_1} \sum_{l_2 m_2} Y_{l_1 m_1}(\theta, \varphi) Y_{l_2 m_2}(\theta, \varphi) Y_{l_1 m_1}^*(\theta', \varphi') Y_{l_2 m_2}^*(\theta', \varphi') \\ &\quad \sum_{ip_n} \Delta W_{l_1}(r, r'; ip_n) G_{l_2}(r, r'; i\Omega_n - ip_n) \end{aligned}$$

According to Eq.(A.9), the coupling of the spherically harmonic functions gives,

$$\begin{aligned} \Sigma^R(\mathbf{r}, \mathbf{r}') &= -\frac{1}{\beta\hbar^2} \sum_{lm} \sum_{l'm'} \sum_{l_1 l_2} \frac{2l_2 + 1}{4\pi} Y_{lm}(\theta, \varphi) Y_{l'm'}^*(\theta', \varphi') C(l_1 l_2 l) C(l_1 l_2 l') \\ &\quad \sum_{ip_n} \Delta W_{l_1}(r, r'; ip_n) G_{l_2}(r, r'; i\Omega_n - ip_n) \\ &\quad \sum_{m_1 m_2} \tilde{C}(l_1 l_2 l; m_1 m_2 m) \tilde{C}(l_1 l_2 l'; m_1 m_2 m') \end{aligned}$$

Summing over $m_1 m_2$ using the orthonormal relation (A.7), and then over $l' m'$, the RPA self-energy can be written as,

$$\Sigma^R(\mathbf{r}, \mathbf{r}'; i\Omega_n) = \sum_{lm} Y_{lm}(\theta, \varphi) Y_{lm}^*(\theta', \varphi') \Sigma_l^R(r, r'; i\Omega_n) \quad (2.80)$$

where the radial RPA self-energy is

$$\begin{aligned} \Sigma_l^R(r, r'; i\Omega_n) &\equiv -\frac{k_B T}{4\pi(2l+1)\hbar^2} \sum_{l_1 l_2} (2l_1 + 1)(2l_2 + 1) C(l_1 l_2 l)^2 \\ &\quad \sum_{ip_n} \Delta W_{l_1}(r, r'; ip_n) G_{l_2}(r, r'; i\Omega_n - ip_n) \end{aligned} \quad (2.81)$$

To obtain the corresponding partial Green's function, we substitute equations (2.80) and (2.47) into the equation (2.79), and get

$$\begin{aligned} \mathcal{G}^R(\mathbf{r}, \mathbf{r}'; i\Omega_n) &= \sum_{lm} \sum_{l'_1 m'_1} \sum_{l'_2 m'_2} \int d^3\mathbf{r}_1 d^3\mathbf{r}_2 Y_{l'_1 m'_1}(\theta, \varphi) G_{l'_1}^0(r, r_1; i\Omega_n) Y_{l'_1 m'_1}^*(\theta_1, \varphi_1) Y_{lm}(\theta_1, \varphi_1) \\ &\quad \Sigma_l^R(r_1, r_2; i\Omega_n) Y_{lm}^*(\theta_2, \varphi_2) Y_{l'_2 m'_2}(\theta_2, \varphi_2) G_{l'_2}(r_2, r'; i\Omega_n) Y_{l'_2 m'_2}^*(\theta', \varphi') \end{aligned}$$

Integrating the angular parts using the orthonormal relation of the spherically harmonic function, and then summing over $l'_1 m'_1$ and $l'_2 m'_2$, we obtain

$$\mathcal{G}^R(\mathbf{r}, \mathbf{r}'; i\Omega_n) = \sum_{lm} Y_{lm}(\theta, \varphi) Y_{lm}^*(\theta', \varphi') G_l^F(r, r'; i\Omega_n) \quad (2.82)$$

and the radial counterpart

$$G_l^F(r, r'; i\Omega_n) = \int r_1^2 dr_1 r_2^2 dr_2 G_l^0(r, r_1; i\Omega_n) \Sigma_l^R(r_1, r_2; i\Omega_n) G_l(r_2, r'; i\Omega_n) \quad (2.83)$$

2.6 DYSON EQUATION FOR RADIAL GREEN'S FUNCTION

Collecting the previous results, *i.e.*, Eqs. (2.55), (2.60) and (2.83), and introducing transforms,

$$\begin{aligned}
\tilde{G}_l(r, r'; i\Omega_n) &= r r' G_l(r, r'; i\Omega_n) \\
\tilde{\Sigma}^F(r, r') &= r r' \Sigma^F(r, r') \\
\tilde{\Sigma}^R(r, r'; i\Omega_n) &= r r' \Sigma^R(r, r'; i\Omega_n) \\
\tilde{\Pi}(r, r'; i\Omega_n) &= r^2 r'^2 \Pi(r, r'; i\Omega_n)
\end{aligned} \tag{2.84}$$

we obtain the Dyson equations for the radial Green's function

$$\tilde{G}_l(r, r'; i\Omega_n) = \tilde{G}_l^0(r, r'; i\Omega_n) + \int dr_1 dr_2 \tilde{G}_l^0(r, r_1; i\Omega_n) \tilde{\Sigma}_l(r_1, r_2; i\Omega_n) \tilde{G}_l(r_2, r'; i\Omega_n) \tag{2.85}$$

and the Dyson equation for the screening potential

$$W_l(r, r'; ip_n) = F_l(r, r') + \int dr_1 dr'_1 F_l(r, r_1) \tilde{\Pi}_l(r_1, r'_1; ip_n) W_l(r'_1, r'; ip_n) \tag{2.86}$$

where the self-energies are defined by

$$\tilde{\Sigma}_l(r, r'; i\Omega_n) \equiv \tilde{\Sigma}^H(r) \delta(r - r') + \tilde{\Sigma}_l^F(r, r') + \tilde{\Sigma}_l^R(r, r'; i\Omega_n) \tag{2.87}$$

$$\tilde{\Sigma}^H(r) \equiv \frac{(2s+1)k_B T}{4\pi\hbar^2} \sum_{l'} \int dr_0 (2l'+1) F_0(r, r_0) \sum_{i\omega_n} e^{i\omega_n \eta} \tilde{G}_{l'}(r_0, r_0; i\omega_n) \tag{2.88}$$

$$\begin{aligned}
\tilde{\Sigma}_l^F(r, r') &\equiv -\frac{k_B T}{4\pi(2l+1)\hbar^2} \sum_{l_1 l_2} (2l_1+1)(2l_2+1) F_{l_1}(r, r') C(l_1 l_2 l)^2 \\
&\quad \times \sum_{i\omega_n} e^{i\omega_n \eta} \tilde{G}_{l_2}(r, r'; i\omega_n)
\end{aligned} \tag{2.89}$$

$$\begin{aligned}
\tilde{\Sigma}_l^R(r, r'; i\Omega_n) &\equiv -\frac{k_B T}{4\pi(2l+1)\hbar^2} \sum_{l_1 l_2} (2l_1+1)(2l_2+1) C(l_1 l_2 l)^2 \\
&\quad \times \sum_{ip_n} \Delta W_{l_1}(r, r'; ip_n) \tilde{G}_{l_2}(r, r'; i\Omega_n - ip_n)
\end{aligned} \tag{2.90}$$

and the polarization operator reads

$$\begin{aligned}
\tilde{\Pi}_l(r, r'; ip_n) &\equiv \frac{(2s+1)k_B T}{4\pi(2l+1)\hbar^2} \sum_{lm} \sum_{l_1 l_2} (2l_1+1)(2l_2+1) C(l_1 l_2 l)^2 \\
&\quad \times \sum_{i\omega_n} \tilde{G}_{l_1}(r, r'; i\omega_n) \tilde{G}_{l_2}(r', r; i\omega_n - ip_n)
\end{aligned} \tag{2.91}$$

For convenience in later usage, we re-denote the unperturbed Green's function by $G_0(r, r'; i\Omega_n, l)$.

Multiplying the Dyson equation (2.85) by the inverse of this unperturbed Green's by left side and

integral the equation in both sides, one re-shapes it as

$$\int dr_1 \left[\tilde{G}_0^{-1}(r, r_1; i\Omega_n, l) - \tilde{\Sigma}_l(r, r_1, i\Omega_n) \right] \tilde{G}_l(r_1, r'; i\Omega_n) = \delta(r - r') \quad (2.92)$$

or formally

$$\tilde{G} = \frac{1}{\tilde{G}_0^{-1} - \tilde{\Sigma}} \quad (2.93)$$

where $\tilde{G}_0^{-1}(r, r_1; i\Omega_n, l)$ can be easily obtained via Eq.(2.28), which gives

$$\tilde{G}_0^{-1}(r, r_1; i\Omega_n, l) = [i\Omega_n - H_0(l) + \mu] \delta(r - r') \quad (2.94)$$

with

$$H_0(l) \equiv -\frac{\hbar^2}{2m_e} \left[\frac{d^2}{dr^2} - \frac{l(l+1)}{r^2} \right] + U(r) \quad (2.95)$$

CHAPTER 3

FINITE ELEMENT METHOD AND ITS APPLICATION IN SOLVING THE DYSON EQUATIONS

3.1 INTRODUCTION TO FINITE ELEMENT METHOD

The finite element method [67] is a computational technique for approximately solving the partial differential equations that arise in scientific and engineering applications. Rather than directly discretizing the differential equation as in the finite difference approximation, it utilizes the variational form of the equation which involves an integration of the differential equation over the domain of the problem to get the action functional. This domain is divided into pieces called finite elements. The solution of the differential equation is approximated by the polynomials defined in the finite elements. The action functional of the entire system is obtained by adding up all the contributions of individual elements, in which the continuity of the solution at boundaries of elements should be ensured. The condition of the least action leads to an algebraic equation which gives the approximation solution. It yields not only the solution at the discrete points, but the solution in the form of piecewise polynomial functions over the whole domain as well. The finite element method originally developed in engineering fields has been widely used in the numerical solution of the engineering and scientific problems. It has been introduced to solve pure physical problems recently [68, 69]. This section is a brief introduction of this method. In the next sections, we will discuss its applications in the quantum mechanics, and then extend this method to solve the Dyson equations of the finite temperature Green's function and the corresponding screening potential.

We will begin our discussion with the classical Sturm-Liouville problem, which is expressed by

$$-\frac{d}{dx} \left[p(x) \frac{du}{dx} \right] + q(x) u = f(x) \quad (3.1)$$

defined in $[0, 1]$ with some boundary conditions. Where $p(x)$ and $q(x)$ are continuously differentiable in $x \in [0, 1]$. Without loss of the generality, we assume boundary conditions

$$u(0) = 0, \quad u'(1) = 0. \quad (3.2)$$

Alternatively, we may combine Eq.(3.1) and the boundary conditions (3.2) to give

$$\mathcal{L} u = f \quad (3.3)$$

with \mathcal{L} a linear operator acting on a certain class of functions that satisfy the boundary conditions (3.2) and can be differentiated twice.

In a typical analytical approach, one first constructs an eigenvalue problem for this linear operator \mathcal{L} ,

$$\mathcal{L} \tilde{u} = \lambda \tilde{u} \quad (3.4)$$

and then solves it, getting its infinite eigenvalues $\{\lambda_n\}$ and eigenfunctions $\{\tilde{u}_n(x)\}$ which satisfy the orthonormal condition

$$\int_0^1 \tilde{u}_m(x) \tilde{u}_n(x) dx = \delta_{nm}, \quad m, n = 1, 2, \dots, \infty \quad (3.5)$$

These eigenfunctions span an infinite dimensional Hilbert space \mathcal{H} . Projecting the inhomogeneous function f and the solution $u(x)$ on to this space, one has

$$f(x) = \sum_0^{\infty} a_n \tilde{u}_n(x) \quad (3.6)$$

$$u(x) = \sum_0^{\infty} b_n \tilde{u}_n(x) \quad (3.7)$$

Substitute this two expressions into the original equation (3.3), one obtains the solution of the problem

$$u(x) = \sum_0^{\infty} \frac{a_n}{\lambda_n} \tilde{u}_n(x) \quad (3.8)$$

with

$$a_n = \int_0^1 \tilde{u}_n(x) f(x) dx \quad (3.9)$$

Unfortunately, in many situations, we can not get the analytical solution like this, and have to use numerical methods, for example, the finite difference method. In this approach the domain

$[0, 1]$ is divided into N pieces $\{x_i = ih, i = 0, 1, 2, \dots, N\}$ with $h = 1/N$, and the derivatives are replaced by their finite difference forms

$$\frac{du}{dx} = \frac{u(x_i + h) - u(x_i - h)}{2h} \quad (3.10)$$

$$\frac{d^2u}{dx^2} = \frac{u(x_{i+1}) - 2u(x_i) + u(x_{i-1}))}{h^2} \quad (3.11)$$

Eq.(3.3) immediately reduces to the matrix form

$$L^h U^h = F^h \quad (3.12)$$

where U^h is the column matrix consisting of N values $\{u_i\}$ of the solution at discrete points $\{x_i\}$, and F^h the column matrix of the corresponding function values $\{f_i\}$, and \mathcal{L}^h is the matrix form of the operator \mathcal{L} . Solving this algebraic equation gives an approximate solution of (3.3) at discrete point $\{x_i\}$. One can image that it will tend to the real solution of our problem when the interval of the mesh, h , goes to zero. The solutions at these discrete points $\{x_i\}$ are linearly independent, and they create a finite dimensional Hilbert space, denoted by \mathcal{S}^h . Comparing this algebraic equation (3.12) and the operator equation (3.3), one may believe that the space \mathcal{S}^h is just a finite dimensional subspace of the Hilbert space \mathcal{H} , spanned by the first N eigenstates of the linear operator \mathcal{L} .

The Sturm-Liouville problem can also be described in another way—the variational principle (or say, the least action principle). We construct the following quadratic functional (action) by inner product

$$I(u) = (v, \mathcal{L} v) - 2(v, f) \quad (3.13)$$

Setting the variation of this functional with respect to u equals to zero, *i.e.*,

$$\frac{\delta}{\delta v} I(v) = 0$$

one obtains a linear equation,

$$\mathcal{L} v = f$$

which is the same as equation (3.3). This is just the result of the variational principle, which says: To solve the Sturm-Liouville problem, or equation (3.3), is to find such a function that minimizes the action functional $I(v)$, *i.e.*,

$$\frac{\delta}{\delta v} I(v)|_{v=u} = 0. \quad (3.14)$$

here function $v(x)$ is called the trial function.

The variational statement is the primary physical principle, and the language of differential equations is only a secondary consequence. In the regime of the variational principle, our task is to find a proper trial function $v(x)$ to minimize the action $I(v)$, which leaves plenty of rooms for interpolating the trial function. In numerical work, the continuous space domain (or perhaps include time domain) is usually divided into discrete mesh, which results in projecting the continuous solution function onto a discrete finite N -dimensional subspace of the original Hilbert space as in the finite difference realization. Suppose we know the eigenfunctions and eigenvalues of our differential operator \mathcal{L} , as a test case, let us try to get the solution of this Sturm-Liouville problem via the variational principle. We expand our trial function (denoted by v_N) in terms of the linear combination of the first N eigenfunctions of the Hilbert space \mathcal{H} ,

$$v_N(x) = \sum_{i=1}^N c_i \tilde{u}_i$$

Then the action is written

$$I(v_N) = \sum_{i=1}^N \left[c_i^2 \lambda_i - 2c_i \int_0^1 f \tilde{u}_i \right] = \sum_{i=1}^N [c_i^2 \lambda_i - 2c_i a_i]$$

Now finding a solution changes into determining the values of $\{c_i\}$. The condition $\partial v^h / \partial c_i = 0$ immediately yields a system of N linear equations,

$$\mathcal{L} C = F$$

where,

$$L \equiv \{\lambda_i \delta_{ij}\}, \quad C \equiv \{c_i\}, \quad F \equiv \{a_i\}, \quad i = 1, 2, \dots, N$$

here $\{a_i\}$ are the projections of function f onto this N -dimensional subspace, $\{\lambda_i \delta_{ij}\}$ are the projections of operator \mathcal{L} onto a subspace spanned by its eigenfunctions, and therefore matrix L is diagonal, and $\{c_i\}$ are the quantities we are going to find. The solution of this algebraic equation is very trivial, which is $c_i = a_i / \lambda_i$, and thus the trial solution reads

$$v_N(x) = \sum_{n=1}^N \frac{a_n}{\lambda_n} \tilde{u}_n$$

which is exactly the same to the solution in Eq.(3.8) except that the summation here is over a finite number of eigenstates instead of infinite ones.

This is only a simplest example of solving numerically the problem in the viewpoint of variational principle, where the eigenfunctions $\{\tilde{u}_n\}$ act as the interpolation functions. Actually, approximating the solution of a differential equation based upon this principle is not new. For example, one often expands the wave function of a Schrödinger equation by a Gaussian basis, in quantum mechanics/chemistry calculations. We denote those kind of interpolations as global ones because one has to evaluate the integration over the entire domain when constructing the action defined by Eq.(3.13). The global interpolation is time consuming and sometimes inconvenient, especially for large systems. On the contrary, the finite element method interpolates the trial function by polynomials defined in a finite local range surrounding the interpolation points. The simplest finite element algorithm is the linear finite element. The domain is divided into the subdomains called “elements”, and the corresponding mesh is

$$0 = x_0 < x_1 < \cdots < x_N = 1 \quad (3.15)$$

The j – th element, denoted by e_j , is confined in the interval $[x_{j-1}, x_j]$. Clearly there are two nodes in each element, $N_{node}^e = 2$. A “tent function” is defined for each node (Fig.3.1 only shows two of them),

$$\phi_j^h(x) = \begin{cases} \frac{x-x_{j-1}}{x_j-x_{j-1}}, & \text{if } x_{j-1} \leq x < x_j \\ \frac{x_{j+1}-x}{x_{j+1}-x_j}, & \text{if } x_j \leq x < x_{j+1} \\ 0, & \text{otherwise.} \end{cases} \quad (3.16)$$

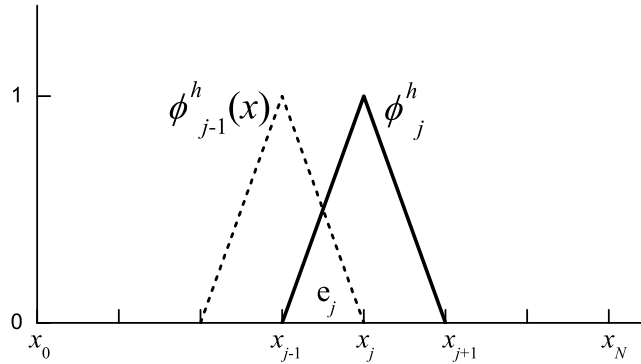


Figure 3.1: 1-D finite element mesh and piecewise tent function

As shown in Fig. 3.1, $\phi_j^h(x)$ is nonzero only in the two adjacent element containing node x_j . It goes up and down linearly in these two elements and has an unit maximum at $x = x_j$. Actually it is required that the interpolation function vanishes at all the other nodes but $x = x_j$, *i.e.*,

$$\phi_j^h(x_i) = \delta_{ij} \quad (3.17)$$

These N functions serve as the basis of the Hilbert subspace \mathcal{S}^h . We may approximate our trial function by projecting it onto this subspace, *i.e.*,

$$v_h(x) = \sum_{j=1}^N u_j \phi_j^h(x) \quad (3.18)$$

with the coefficient corresponding to the basis function ϕ_j^h for node- j being the values of the solution at this same node. Now the calculation of the action integral defined in Eq.(3.13) turns into the summation of sub-actions for all the elements, *i.e.*,

$$I(v_h) = \sum_{j=1}^N I_j(v_h) \quad (3.19)$$

where,

$$I_j(v_h) \equiv \int_{x_{j-1}}^{x_j} dx v_h(x) (\mathcal{L}(x) - 2f(x)) v_h(x) \quad (3.20)$$

In element e_j , the trial function includes only two terms,

$$v_h(x) = u_{j-1} \phi_{j-1}^h(x) + u_j \phi_j^h(x) \quad (3.21)$$

The sub-action is itself a 2 by 2 matrix,

$$I_j(v_h) = \tilde{U}^j L^j U^j - 2 \tilde{U}^j F^j \quad (3.22)$$

where \tilde{U}^j is the transpose of matrix U^j , defined by

$$\tilde{U}^j \equiv (u_{j-1}, u_j). \quad (3.23)$$

Elements of the matrices L and F are defined by

$$L_{mn}^j \equiv \int_{x_{j-1}}^{x_j} dx \phi_m^h(x) \mathcal{L}(x) \phi_n^h(x), \quad m, n = j-1, j \quad (3.24)$$

$$F_m^j \equiv \int_{x_{j-1}}^{x_j} dx \phi_m^h(x) f(x), \quad m = j-1, j \quad (3.25)$$

We would like to emphasize that the condition in (3.17) is actually a basic feature of the finite element interpolation. It guarantees that the expansion (3.18) gives $v_h(x_j) = u_j$, where $\{u_j\}$ are just the solution we are looking for. Nevertheless, condition (3.17) also assures the continuity of the solution at the boundaries between successive elements, which make the summation of two successive sub-actions a direct summation, *e.g.*,

$$I_j(v_h) + I_{j+1}(v_h) = \left(\tilde{U}^j \cup \tilde{U}^{j+1} \right) \left\{ (L^j \oplus L^{j+1}) (U^j \cup U^{j+1}) - 2(F^j \oplus F^{j+1}) \right\}$$

Finally the total action is a N by N matrix defined by the direct summation of the sub-action matrices,

$$I(v_h) = \sum_{j=1}^N \oplus I_j(v_h) = \tilde{U} L U - 2 \tilde{U} F \quad (3.26)$$

with

$$\tilde{U} = (u_1, u_2, u_3, \dots, u_N) \quad (3.27)$$

$$L = L^1 \oplus L^2 \oplus L^3 \oplus \dots \oplus L^N \quad (3.28)$$

$$F = F^1 \oplus F^2 \oplus F^3 \oplus \dots \oplus F^N \quad (3.29)$$

here the solution at the very first point $x_i = 0$ is eliminated due to the boundary condition $u(0) = 0$.

The variational condition $\delta I(v_h)/\delta u_j = 0$ results in the algebraic equation,

$$L U = F \quad (3.30)$$

which leads to the solution of our problem.

During the creation of the finite element form, the integrals defined in Eqs. (3.24) and (3.25) are calculated to get the sub-action matrices for all the elements. The two basis functions ϕ_{j-1}^h and ϕ_j^h (actually, only the descent branch of the former and the ascent branch of the latter) are encountered again and again in different elements when j goes from 1 to N , but all of them are in the same form. So we treat them systematically through introducing the local coordinate systems that map the subdomain $[x_{j-1}, x_j]$ onto interval $[0, 1]$ by transformation

$$\xi = x/s_{e_j} - j + 1 \quad (3.31)$$

where s_{e_j} is the size of j -th element (here in the current example, all the elements have the same size). Each element has $N_{\text{node}}^e = 2$ nodes, and two basis functions. They are the descent branch of $\phi_{j-1}^h(x)$ and the ascent branch of $\phi_j^h(x)$, which actually span a subspace of subspace \mathcal{S}^h .

Now each element is associated with a subspace. We are only interested in one of the elements since these two basis functions are the same for all the elements. We rename and re-define them in a local coordinate system as (see Fig. 3.2),

$$\begin{aligned}\varphi_1(\xi) &= \xi \\ \varphi_2(\xi) &= 1 - \xi\end{aligned}\quad (3.32)$$

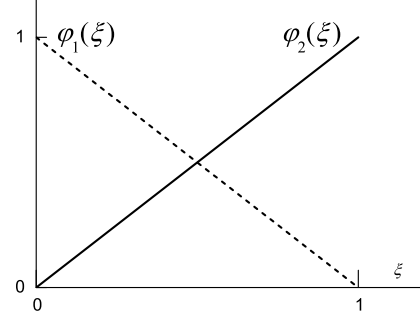


Figure 3.2: linear basis functions in local coordinate system

By introducing the local coordinates and local basis functions, Eqs. (3.24) and (3.25) are re-shaped as

$$L_{\mu\nu}^j \equiv \int_0^1 \varphi_\mu(\xi) \mathcal{L}(\xi) \varphi_\nu(\xi) s_{e_j} d\xi, \quad \mu, \nu = 1, N_{\text{node}}^e \quad (3.33)$$

$$F_\mu^j \equiv \int_0^1 \varphi_\mu(\xi) f(\xi) s_{e_j} d\xi, \quad \mu = 1, N_{\text{node}}^e \quad (3.34)$$

It can be easily shown that the matrix equation (3.30) is identical to Eq.(3.12) obtained by the finite difference method with the derivatives involved in the linear operator \mathcal{L} defined by Eq.(3.11). The linear element is only the simplest application of the spirit of the finite element method. In practice, one have plenty of flexibility to improve the stability and the precision. For example, one may create finite element form based on inhomogeneous mesh using dense element for important regions, which is impossible in the finite difference method. One can also employ higher order interpolation functions, such as Lagrange polynomial (with $N_{\text{node}}^e = 3$ nodes in each element, seen in Fig. 3.3),

$$\varphi_\mu(\xi) = \prod_{\nu=1, \nu \neq \mu}^{N_{\text{node}}^e} \frac{(\xi - \xi_\nu)}{(\xi_\mu - \xi_\nu)} \quad (3.35)$$

These functions satisfy $\varphi_\mu(\xi_\nu) = \delta_{\mu\nu}$. In the later parts of the current dissertation, we use cubic polynomials for our interpolation functions, which gives us much stable result.

In all the previous part, we only focus on the interpolation for the solution functions. However, one can even interpolate the derivatives, for example the Hermite interpolation (shown in Fig. 3.4) which interpolates both the function itself and its first order derivative,

$$v_h(\xi) = \sum_{\mu}^{N_{\text{node}}^e} \sum_{\sigma=0}^1 u_{\mu,\sigma} \varphi_{\mu,\sigma} \quad (3.36)$$

where $\sigma = 0$ represents interpolation for the function itself, and $\sigma = 1$ for the first order derivative. The interpolation functions must satisfy the following conditions,

$$\begin{aligned}\varphi_{\mu,0}(\xi_\nu) &= \delta_{\mu\nu}, & \varphi_{\mu,1}(\xi_\nu) &= 0 \\ d\varphi_{\mu,0}/d\xi &= 0, & d\varphi_{\mu,1}/d\xi &= \delta_{\mu\nu}\end{aligned}\quad (3.37)$$

which gives the explicit expression,

$$\begin{aligned}\varphi_{10}(\xi) &= 1 - 3\xi^2 + 2\xi^3, & \varphi_{11}(\xi) &= \xi - 2\xi^2 + \xi^3 \\ \varphi_{20}(\xi) &= 3\xi^2 - 2\xi^3, & \varphi_{21}(\xi) &= -\xi^2 + \xi^3\end{aligned}\quad (3.38)$$

Hermite interpolation does not increase the node number in the element but get higher order polynomials and also solve for the first derivative besides the solution itself.

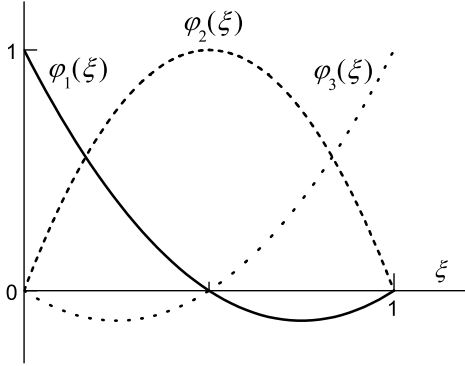


Figure 3.3: Quadratic Lagrange polynomials

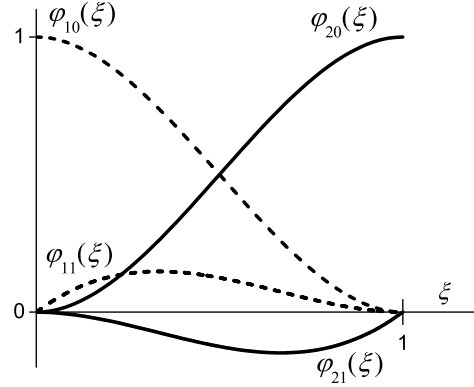


Figure 3.4: Cubic Hermite polynomials

3.2 FINITE ELEMENT FORM OF SCHRÖDINGER EQUATION

In this section, we will apply the finite element method to solve the stationary Schrödinger equation. In fact, this equation can be constructed through the variational principle [70], by considering the action

$$I(\psi) = \int d^2\mathbf{r} \left\{ \frac{\hbar^2}{2m_e} \nabla\psi^*(\mathbf{r}) \cdot \nabla\psi(\mathbf{r}) + \psi^*(\mathbf{r}) [U(\mathbf{r}) - \epsilon] \psi(\mathbf{r}) \right\} \quad (3.39)$$

If treating ψ and ψ^* as independent quantities (with their conjugate relation temporarily ignored) and calculating the variation with respect to ψ^* , we get the stationary Schrödinger equation

$$-\frac{\hbar^2}{2m_e} \nabla^2 \psi(\mathbf{r}) + U(\mathbf{r})\psi(\mathbf{r}) = \epsilon\psi(\mathbf{r}) \quad (3.40)$$

Similarly the variation with respect to ψ yields the same equation for ψ^* . All the equations are consistent if ψ^* is the complex conjugate of ψ .

The numerical solution of the quantum mechanical problems involves the discretization of the Schrödinger equation or the action defined upon the continuous space. There are in general two approaches. One discretizes the differential equation, while the other one the action integral. They are in two levels. In the differential equation level, one may project the Schrödinger equation onto a finite-dimensional subspace of an infinite-dimensional Hilbert space to get the matrix form of it. One can also use the finite difference method, in which a proper difference form of the derivatives should be chosen, special attention should be paid to treat the higher order derivatives. The action description is usually in a weak form, dealing with the lower order derivative. Here in the stationary case, only the first derivative is included, which is a great advantage for the numerical computing. Actually the boundary condition has already been involved when the action in Eq.(3.39) is built. This can be seen by integrating the corresponding differential equation and applying partial integral for the terms where the secondary derivatives are involved. Discretization from the level of the variational principle allows a considerable freedom to choose the interpolation method. One can use either the interpolation functions defined globally on the domain of the problem as in the quantum chemistry calculations, or the localized interpolation functions in the finite element analysis. To create a finite element form, we first divide the domain of our problem into elements $\{e_j, j = 1 \text{ to } N\}$ with even size s . Each element has N_{node}^e nodes. There are totally $N_{node} = N \times (N_{node}^e - 1) + 1$ nodes. Assign each node a $(N_{node}^e - 1)$ -order polynomial $\phi_m^h(x)$ such that

$$\phi_m^h(x_n) = \delta_{mn}, \quad m, n = 0, N_{node} \quad (3.41)$$

and

$$\phi_m^h(x) = \begin{cases} \varphi_\mu(\xi), & \text{if } x \in e_j \\ 0, & \text{if } x \notin e_j \end{cases} \quad (3.42)$$

with

$$j = 1 + \text{mod}(m, N_{node}^e), \quad \xi = x/s - j + 1, \quad \mu = m + 1 - (j - 1)(N_{node}^e - 1) \quad (3.43)$$

where the polynomial $\{\varphi_\mu(\xi), \mu = 1 \text{ to } N_{node}^e\}$ are the same to all elements, we call them the local representation of the interpolation functions, which is introduced just to simplify the evaluation of the matrices in building up the actions. The use of global counterpart of the interpolation functions $\{\phi_m^h(x)\}$ is convenient for the generalized description of the finite element method especially when comparing with the other methods.

Now we expand the wavefunction as

$$\psi(x) = \sum_{i=0}^{N_{node}} \psi_i \phi_i^h(x) \quad (3.44)$$

where ψ_i is the value of the wave function at node x_i , which is assumed by the condition (3.41). Substitute this expansion into the definition of the action (3.39), we obtain the matrix form of the action

$$\mathbf{I} = \mathbf{\Psi}^\dagger (\mathbf{H} - \epsilon \mathbf{M}) \mathbf{\Psi} \quad (3.45)$$

and

$$\mathbf{\Psi}^\dagger \equiv \{\psi_0^*, \psi_1^*, \psi_2^*, \dots, \psi_{N_{node}}^*\} \quad (3.46)$$

$$\mathbf{M} \equiv \sum_{j=1}^N \oplus \mathbf{M}^j \quad (3.47)$$

$$\mathbf{H} \equiv \sum_{j=1}^N \oplus \mathbf{H}^j \quad (3.48)$$

The elements of \mathbf{M}^j and \mathbf{H}^j in the local coordinate presentation are given by

$$M_{\mu\nu}^j = \int_0^1 s \varphi_\mu(\xi) \varphi_\nu(\xi) d\xi \quad (3.49)$$

$$H_{\mu\nu}^j = \int_0^1 \left[\frac{\hbar^2}{2m_e s} \varphi'_\mu(\xi) \varphi'_\nu(\xi) + s \varphi_\mu(\xi) U((\xi + j - 1)s) \varphi_\nu(\xi) \right] d\xi \quad (3.50)$$

The variational principle leads to the matrix form of the Schrödinger equation

$$\mathbf{H} \mathbf{\Psi} = \epsilon \mathbf{M} \mathbf{\Psi} \quad (3.51)$$

which is a generalized eigenvalue problem due to the multiplication of matrix \mathbf{M} called the mass matrix in the terminology of the finite element method. A modern algebraic algorithm has already been developed for solving this problem (see for example ref. [71]).

Regarding the matrix form of the Schrödinger equation, a short remark will be given in the following, which provides us with an alternative way for constructing the finite element form. Combining the kinetic and the potential terms into an operator H , the Schrödinger equation (3.40) can be formally expressed by

$$H|\psi\rangle = \epsilon|\psi\rangle \quad (3.52)$$

One can explain this as either an eigenvalue problem of the differential equation, or an algebraic eigenvalue problem. Actually the matrix form of Schrödinger equation (quantum mechanics) can be obtained by simply projecting this differential operator equation on to a *complete* and *orthonormal* set $\{\phi_m\}$,

$$\langle\phi_m|\phi_n\rangle = \delta_{mn} \quad (3.53)$$

$$\sum_m |\phi_m\rangle\langle\phi_m| = 1 \quad (3.54)$$

Projecting Eq.(3.52) on this basis yields

$$\langle\phi_m|H|\psi\rangle = \epsilon\langle\phi_m|\psi\rangle \quad (3.55)$$

Substitute the complete condition (3.54) gives

$$\sum_n \langle\phi_m|H|\phi_n\rangle\langle\phi_n|\psi\rangle = \epsilon\langle\phi_m|\psi\rangle \quad (3.56)$$

Since the basis $|\phi\rangle$'s are orthonormal, $\phi_n|\psi\rangle$ is just the projection of $|\psi\rangle$ onto $|\phi_n\rangle$, *i.e.*, c_n . Therefore, Eq.(3.56) changes into

$$\sum_n \langle m|H|n\rangle c_n = \epsilon c_m \quad (3.57)$$

This is just the Heisenberg's matrix mechanics

One may also obtain the above matrix equation by the following procedures, in which the complete condition will not be mentioned. The expansion of $|\psi\rangle$ in terms of this $\{\phi_m\}$ basis reads

$$|\psi\rangle = \sum_n c_n |\phi_n\rangle \quad (3.58)$$

Substitute this expansion into Eq.(3.52), we have

$$\sum_n c_n H|\phi_n\rangle = \epsilon \sum_n c_n |\phi_n\rangle \quad (3.59)$$

Projecting Eq.(3.59) onto $\langle\phi_m|$ yields

$$\sum_n \langle\phi_m|H|\phi_n\rangle c_n = \epsilon \sum_n c_n \langle\phi_m|\phi_n\rangle \quad (3.60)$$

Employing the orthonormal condition (3.53), one obtains the matrix form of the Schrödinger equation

$$\sum_n \langle m|H|n\rangle c_n = \epsilon c_m \quad (3.61)$$

If we define $\mathbf{H} \equiv \{\langle m|H|n\rangle\}$ and $\mathbf{\Psi} = \{c_m\}$, we have the matrix form of Schrödinger equation

$$\mathbf{H}\mathbf{\Psi} = \epsilon\mathbf{\Psi} \quad (3.62)$$

It is helpful to compare the matrix form of Schrödinger equation (3.62) with its finite element form defined by (3.51), where the matrix multiplier appears in the right hand side of the eigenvalue equation. This is easily understood because in the finite element approach a non-orthonormal basis is used. Now we try to re-derive the generalized matrix eigenvalue equation (3.51) following the procedures from Eq.(3.58) to (3.65), but utilizing the finite element basis defined by Eqs.(3.41) and (3.42). We avoid the derivations by following the way from (3.55) to (3.57) because of the problem in the completeness of the finite element basis (we will discuss this at the end of the section). We expand the wave function in the finite element basis (here only the global form of the finite element basis is involved just for convenience) as

$$|\psi\rangle = \sum_n \psi_n |\phi_n^h\rangle \quad (3.63)$$

here the coefficients are $\{\psi_n\}$, the values of the wave function at the nodes. Substitute this expansion into Eq.(3.52), we have

$$\sum_n \psi_n H|\phi_n^h\rangle = \epsilon \sum_n \psi_n |\phi_n^h\rangle \quad (3.64)$$

Project this equation onto $\langle\phi_m^h|$, one has

$$\sum_n \langle\phi_m^h|H|\phi_n^h\rangle \psi_n = \epsilon \sum_n \psi_n \langle\phi_m^h|\phi_n^h\rangle \quad (3.65)$$

Here, the matrix elements $\langle \phi_m^h | \phi_n^h \rangle$ are nothing but the elements of mass matrix \mathbf{M} defined previously. Thus we reach the generalized matrix eigenvalue problem, *i.e.*,

$$\sum_n \langle m | H | n \rangle^h \psi_n = \epsilon \sum_n M_{mn} \psi_n \quad (3.66)$$

where the $\langle m | H | n \rangle^h$, for one dimensional systems, is expressed as

$$\begin{aligned} \langle m | H | n \rangle^h &= \langle \phi_m^h | H | \phi_n^h \rangle = \int \phi_m^h(x) H \phi_n^h(x) dx \\ &= \int \phi_m^h(x) \left[-\frac{\hbar^2}{2m_e} \frac{d^2}{dx^2} + U(x) \right] \phi_n^h(x) dx \end{aligned} \quad (3.67)$$

One may notes that there is a second order derivative included in (3.67) acting on a basis function here, but in Eq.(3.50) appeared are the product of the two first derivatives of the basis functions. It is not surprise as we have pointed out previously that this is due to the partial integral when building up the action. We can also apply this trick here when calculating the matrix element,

$$\begin{aligned} \langle m | H | n \rangle^h &= \int_{x_a}^{x_b} \left[\left(\frac{\hbar^2}{2m_e} \right) \frac{d\phi_m^h(x)}{dx} \cdot \frac{d\phi_n^h(x)}{dx} + \phi_m^h(x) U(x) \phi_n^h(x) \right] dx \\ &\quad + \frac{\hbar^2}{2m_e} \left[\phi_m^h(x_a) \frac{d\phi_n^h(x)}{dx} \Big|_{x_a} - \phi_m^h(x_b) \frac{d\phi_n^h(x)}{dx} \Big|_{x_b} \right] \end{aligned} \quad (3.68)$$

Here we assume that our problem is confined in domain $[x_a, x_b]$. For an infinite extending systems, *i.e.*, defined in $(-\infty, +\infty)$, it is physically required that the wave function vanishes asymptotically as $x \rightarrow \pm\infty$, then the last two terms can be dropped. But for those systems with a nonzero wavefunction at boundaries, for example the scattering problem, this term should be kept (the action should be revised). In summary, we emphasize that the finite element forms for problems under investigation can be built up at the level of the differential equation.

Finally we intend to add some words on the completeness of the finite element basis. By definition it is required that the interpolation polynomials involved in the finite element analysis must satisfy conditions (3.17), or should the first derivatives also be interpolated, condition (3.37). These conditions simply gives the following feature

$$\sum_{m=0}^{N_{node}} \phi_m^h(x_k) \phi_m^h(x_l) = (N_{node} + 1) \delta_{kl} \quad (3.69)$$

Therefore, it is understood that the completeness of the finite element basis is there, at least for this discretized system in the numerical realization.

3.3 FINITE ELEMENT FORM OF DYSON EQUATIONS FOR RADIAL GREEN'S FUNCTION AND SCREENING POTENTIAL

In this section, the methods developed previously are used to create the finite element form of the Dyson equations for the radial Green's function and screening potential. The work domain is $[0, R_{\max}]$ with R_{\max} the cutoff radius. It is divided into N elements. The cubic Lagrange polynomials $\{\phi_m(r), m = 1, 2, 3, 4\}$ are chosen as the basis. There are $N_{node}^e = 4$ nodes in each element, and all together $N_{node} = 3N + 1$ nodes $\{r_i, i = 0, 3N\}$. The expansion of the Green's function in this basis reads

$$\tilde{G}_l(r, r'; i\Omega_n) = \sum_{kn} \phi_k^h(r) \tilde{G}_{kn}(i\Omega_n, l) \phi_n^h(r') \quad (3.70)$$

According to the property of these interpolation function as we discussed in the previous sections, the coefficients $\tilde{G}_{kn}(i\Omega_n, l)$ is nothing but the value of the Green's function between these two discrete points r_k and r_n , *i.e.*,

$$\tilde{G}_{kn}(i\Omega_n, l) \equiv \tilde{G}_l(r_k, r_n; i\Omega_n) \quad (3.71)$$

Substitute the expansion (3.70) into (2.92) of section 2.6, multiple by the function $\phi_m^h(r)$ from the left of the resulting equation and carry out the integrals with respect to r , to obtain

$$\sum_{kn} [(i\Omega_n + \mu) M_{mk} - H_{mk}^0(l) - \Sigma_{mk}(i\Omega, l)] \tilde{G}_{kn}(i\Omega_n, l) \phi_n^h(r') = \phi_m^h(r') \quad (3.72)$$

This equation holds for arbitrary variable r' , which yields the finite element form of the radial Dyson equation

$$\sum_k \Gamma_{mk}(i\Omega_n, l) \tilde{G}_{kn}(i\Omega_n, l) = \delta_{mn} \quad (3.73)$$

Formally, we have

$$\mathbf{\Gamma G} = \mathbf{1} \quad (3.74)$$

where $\mathbf{1}$ is the identity matrix. The corresponding matrices are defined by

$$\Gamma_{mk}(i\Omega_n, l) \equiv (i\Omega_n + \mu) M_{mk} - H_{mk}^0(l) - \Sigma_{mk}(i\Omega, l) \quad (3.75)$$

where the matrix M_{mk} is defined by

$$M_{mk} \equiv \int_0^{R_{\max}} \phi_m^h(r) \phi_k^h(r) dr \quad (3.76)$$

The matrix element $H_{mk}^0(l)$ is

$$\begin{aligned} H_{mk}^0(l) &\equiv \int_0^{R_{\max}} \phi_m^h(r) \left[-\frac{\hbar^2}{2m_e} \frac{d^2}{dr^2} + \frac{l(l+1)}{r^2} + U(r) \right] \phi_k^h(r) dr \\ &= \int_0^{R_{\max}} \phi_m^h(r) \left[\frac{\hbar^2}{2m_e} \frac{\overleftarrow{d}}{dr} \frac{\overrightarrow{d}}{dr} + l(l+1)r^2 + U(r) \right] \phi_k^h(r) dr \end{aligned} \quad (3.77)$$

where, “ \leftarrow ” and “ \rightarrow ” represents the action on the function at left and right side, respectively. In the last expansion of this equation only the first order derivatives appear. This is due to the fact that, we have proved in Appendix B, the radial Green’s function itself tends to zero asymptotically when r goes to 0 and ∞ .

The self-energy matrix is defined as

$$\Sigma_{km}(i\Omega_n, l) \equiv \int_0^{R_{\max}} dr dr' \phi_k^h(r) \tilde{\Sigma}_l(r, r'; i\Omega_n) \phi_m^h(r') \quad (3.78)$$

Expanding the self-energy in the same basis $\{\phi_m(r)\}$, one has

$$\tilde{\Sigma}_l(r, r'; i\Omega_n) = \sum_{ij} \phi_i^h(r) \tilde{\Sigma}_{ij}(i\Omega_n, l) \phi_j^h(r') \quad (3.79)$$

and inserting at Eq.(3.78), we finally have the finite element form of the self-energy matrix

$$\Sigma_{km}(i\Omega_n, l) = \sum_{ij} M_{ki} \tilde{\Sigma}_{ij}(i\Omega_n, l) M_{jm} \quad (3.80)$$

Please keep in mind that here the self-energy is just the one defined in (2.87) of section 2.6, *i.e.*,

$$\tilde{\Sigma}_{ij}(i\Omega_n, l) \equiv \tilde{\Sigma}_l(r_i, r_j; i\Omega_n) \quad (3.81)$$

Similarly, as in Eq.(3.79), expanding all the quantities involved in the Dyson equation Eq.(2.86) of the screening potential in the finite element basis gives the finite element form

$$\sum_k \left[\delta_{mk} - \sum_j F_{mj}^l \Pi_{jk}(ip_n, l) \right] W_{kn}(ip_n, l) = F_{mn}^l \quad (3.82)$$

which is formally expressed as

$$(\mathbf{1} - \mathbf{F}\mathbf{\Pi}) \mathbf{W} = \mathbf{F} \quad (3.83)$$

where the matrix elements are defined by

$$F_{mn}^l \equiv F_l(r_m, r_n) \quad (3.84)$$

$$W_{kn}(ip_n, l) \equiv W(r_k, r_n; ip_n, l) \quad (3.85)$$

$$\Pi_{jk}(ip_n, l) \equiv \sum_{mn} M_{jm} \tilde{\Pi}(r_m, r_n, ip_n, l) M_{nk} \quad (3.86)$$

with $F_l(r, r')$, $W(r, r'; ip_n, l)$, and $\tilde{\Pi}(r, r', ip_n, l)$ defined in chapter 2.

We close this section with a simpler example, the Hartree-Fock approximation. It can be easily shown that, when only the Hartree-Fock self-energy is considered, solving the Dyson equation for the Green's function changes into solving a simple Schrödinger equation-like equation for the wavefunction with the self-energy as a static nlocal potential [61]. The radial portion of the equation reduces to

$$\left\{ -\frac{\hbar^2}{2m_e} \left[\frac{d^2}{dr^2} - \frac{l(l+1)}{r^2} \right] + U(r) \right\} \tilde{\varphi}_l(r) = \int \tilde{\Sigma}_l^{\text{HF}}(r, r') \tilde{\varphi}_l(r') dr' + \epsilon_l \tilde{\varphi}_l(r) \quad (3.87)$$

where l is the angular quantum number. In the same finite element basis, we can get the matrix form of this equation with nlocal potential, which is

$$\sum_j H_{ij}^{\text{HF}}(l) \tilde{\varphi}_l(r_j) = \epsilon_l \sum_j M_{ij} \tilde{\varphi}_l(r_j) \quad (3.88)$$

$$H_{ij}^{\text{HF}}(l) \equiv H_{ij}^0(l) - \Sigma_{ij}^{\text{HF}}(l) \quad (3.89)$$

where we denote the j -th node by r_j in the wavefunction $\tilde{\varphi}_l(r_j)$ in order not to confuse with the quantum numbers, $H_{ij}^0(l)$ is defined in Eq.(3.77), and $\Sigma_{ij}^{\text{HF}}(l)$ is the same to the self-energy in Eq.(3.80) only if it is the Hartree-Fock self-energy. Once again we get a generalized eigenvalue problem, which is expressed formally as

$$\mathbf{H}^{\text{HF}} \boldsymbol{\varphi} = \epsilon_l \mathbf{M} \boldsymbol{\varphi} \quad (3.90)$$

The eigenenergies $\{\epsilon_{ln}\}$ and the eigenstates $\{\tilde{\varphi}_{ln}(r_j)\}$ can be obtained, for example, by solving this equation with a code for algebraic eigenvalue from the FORTRAN program library LAPACK [71]. Now we can simply construct the radial Green's function under the Hartree-Fock approximation

$$\tilde{G}_{ij}^{\text{HF}}(i\Omega_n, l) \equiv \sum_n \frac{\tilde{\varphi}_{ln}(r_i) \tilde{\varphi}_{ln}^*(r_j)}{i\Omega_n - \epsilon_{ln} + \mu} \quad (3.91)$$

where n is the principal quantum number, $i\Omega_n$ is the Matsubara frequency, and μ is the chemical potential. This Green's function is used as a reference when computing the frequency summations in this work, because one can easily get the analytical sum of this reference Green's by contour integral.

CHAPTER 4

ELECTRON POLARIZATION AND LINEAR RESPONSE THEORY

4.1 ELECTRODYNAMICS OF ELECTRON POLARIZATION

The polarization process of electrons in an external electron field is usually described by the density of polarization, $\mathbf{P}(\mathbf{r}, t)$. The charge density due to the polarization can be calculated by,

$$\rho_M(\mathbf{r}, t) = -\nabla \cdot \mathbf{P}(\mathbf{r}, t) \quad (4.1)$$

and the time derivative reads,

$$\partial_t \rho_M(\mathbf{r}, t) = -\nabla \cdot \partial_t \mathbf{P}(\mathbf{r}, t) \quad (4.2)$$

According to the continuity equation of the current and charge, one has

$$\partial_t \mathbf{P}(\mathbf{r}, t) = \mathbf{J}_M \quad (4.3)$$

Formally, we get

$$\mathbf{P}(\mathbf{r}, t) = \int_{-\infty}^t dt' \mathbf{J}_M(\mathbf{r}, t') e^{\eta t'}, \quad \eta = 0^+ \quad (4.4)$$

Substitute the inverse Fourier transformation of $\mathbf{J}_M(\mathbf{r}, t')$ in this equation and integrate over t' , we obtain the relation between the density of polarization and the current density in frequency domain, *i.e.*,

$$\mathbf{P}(\mathbf{r}, \omega) = \frac{i}{\omega + i\eta} \mathbf{J}_M(\mathbf{r}, \omega) \quad (4.5)$$

Then the frequency dependence of the dipole moment due to the polarization can be simply obtained by,

$$\begin{aligned} \mathbf{p}(\omega) &= \int d^3\mathbf{r} \mathbf{P}(\mathbf{r}, \omega) \\ &= \frac{i}{\omega} \int d^3\mathbf{r} \mathbf{J}_M(\mathbf{r}, \omega) \end{aligned} \quad (4.6)$$

Considering Ohm's law,

$$\mathbf{J}_\mu(\mathbf{r}, \omega) = \sum_\nu \sigma_{\mu\nu}(\mathbf{r}, \omega) \mathbf{E}_\nu(\mathbf{r}, \omega) \quad (4.7)$$

we may rewrite the Eq.(4.6) as,

$$p_\mu(\omega) = \frac{i}{\omega} \sum_\nu \int d^3\mathbf{r} \sigma_{\mu\nu}(\mathbf{r}, \omega) \mathbf{E}_\nu(\mathbf{r}, \omega) \quad (4.8)$$

where $\mu, \nu = 1, 2, 3$ represent the components of electric field \mathbf{E} , current density \mathbf{J}_M and the dipole moment \mathbf{p} , $\sigma_{\mu\nu}$ is the conductivity density tensor.

Now we have got the basic physical quantities to describe the electron polarization. In order to relate the dipole moment with the potentials for the later use, we choose the Landau gauge

$$\phi(\mathbf{r}, \omega) = 0 \quad (4.9)$$

$$\mathbf{E}(\mathbf{r}, \omega) = -\frac{1}{c} \partial_t \mathbf{A}(\mathbf{r}, \omega) \quad (4.10)$$

From Eq.(4.10), we get

$$\mathbf{A}(\mathbf{r}, t) = -c \int_{-\infty}^t dt' \mathbf{E}(\mathbf{r}, t')$$

A similar derivation to that of obtaining Eq.(4.5), we have

$$\mathbf{A}(\mathbf{r}, \omega) = -\frac{ic}{\omega} \mathbf{E}(\mathbf{r}, \omega)$$

Using this relation, Eq.(4.7) and (4.8) can be rewritten as

$$\mathbf{J}_\mu(\mathbf{r}, \omega) = \frac{i\omega}{c} \sum_\nu \sigma_{\mu\nu}(\mathbf{r}, \omega) \mathbf{A}_\nu(\mathbf{r}, \omega) \quad (4.11)$$

$$p_\mu(\omega) = -\frac{1}{c} \sum_\nu \int d^3\mathbf{r} \sigma_{\mu\nu}(\mathbf{r}, \omega) \mathbf{A}_\nu(\mathbf{r}, \omega) \quad (4.12)$$

When the wavelength is largely greater than the size of the sample, one may approximate the electric field $\mathbf{E}(\mathbf{r}, \omega)$ by an uniform field and then the dipole moment can be rewritten as,

$$p_\mu(\omega) = \sum_\nu \alpha_{\mu\nu}(\omega) E_\nu(\omega) \quad (4.13)$$

$$= \frac{i\omega}{c} \sum_\nu \alpha_{\mu\nu}(\omega) \mathbf{A}_\nu(\omega) \quad (4.14)$$

where $\alpha_{\mu\nu}$ is the polarizability tensor, defined by

$$\alpha_{\mu\nu}(\omega) \equiv \frac{i}{\omega} \int d^3\mathbf{r} \sigma_{\mu\nu}(\mathbf{r}, \omega) \quad (4.15)$$

4.2 LINEAR RESPONSE THEORY FOR ELECTRON DENSITY

The Hamiltonian of a macrosystem of electrons in an external electromagnetic field reads,

$$H_T = H_k + H_V$$

where H_V is the potential energy part and H_k is the kinetic energy term defined by,

$$H_k \equiv \sum_{\sigma} \int d^3\mathbf{r} \frac{1}{2m_e} \left[\left(i\hbar\nabla - \frac{q}{c}\mathbf{A}(\mathbf{r}, t) \right) \hat{\Psi}_{\sigma}^{\dagger}(\mathbf{r}) \right] \cdot \left[\left(-i\hbar\nabla - \frac{q}{c}\mathbf{A}(\mathbf{r}, t) \right) \hat{\Psi}_{\sigma}(\mathbf{r}) \right] \quad (4.16)$$

here σ is the spin index. A simple derivation changes the Hamiltonian into the following form,

$$H_T = H + H_I \quad (4.17)$$

where H is the Hamiltonian that includes the potential and kinetic energy terms of the macrosystem before the electromagnetic field is applied. While the interaction Hamiltonian can be expressed by

$$\begin{aligned} H_I = & -\frac{1}{c} \int d^3\mathbf{r} \frac{q\hbar}{2m_e i} \sum_{\sigma} \left[\hat{\Psi}_{\sigma}^{\dagger}(\mathbf{r}) \nabla \hat{\Psi}_{\sigma}(\mathbf{r}) - \left(\nabla \hat{\Psi}_{\sigma}^{\dagger}(\mathbf{r}) \right) \hat{\Psi}_{\sigma}(\mathbf{r}) \right] \cdot \mathbf{A}(\mathbf{r}, t) \\ & + \frac{1}{c} \int d^3\mathbf{r} \frac{q^2}{2m_e c} \sum_{\sigma} \hat{\Psi}_{\sigma}^{\dagger}(\mathbf{r}) \hat{\Psi}_{\sigma}(\mathbf{r}) |\mathbf{A}(\mathbf{r}, t)|^2 \end{aligned} \quad (4.18)$$

The density of the current induced by the external electromagnetic field is define by

$$\mathcal{J}_{\mu}(\mathbf{r}, t) \equiv -c \frac{\delta H_T}{\delta A_{\mu}} \quad (4.19)$$

A simple calculation gives,

$$\mathcal{J}_{\mu}(\mathbf{r}, t) = \mathcal{J}_{\mu}^P(\mathbf{r}) + \mathcal{J}_{\mu}^D(\mathbf{r}, t) \quad (4.20)$$

with

$$\mathcal{J}_{\mu}^P(\mathbf{r}) = \frac{q\hbar}{2m_e i} \sum_{\sigma} \left[\hat{\Psi}_{\sigma}^{\dagger}(\mathbf{r}) \partial_{\mu} \hat{\Psi}_{\sigma}(\mathbf{r}) - \left(\partial_{\mu} \hat{\Psi}_{\sigma}^{\dagger}(\mathbf{r}) \right) \hat{\Psi}_{\sigma}(\mathbf{r}) \right] \quad (4.21)$$

$$\mathcal{J}_{\mu}^D(\mathbf{r}, t) = -\frac{q^2}{mc} \sum_{\sigma} \hat{\Psi}_{\sigma}^{\dagger}(\mathbf{r}) \hat{\Psi}_{\sigma}(\mathbf{r}) A_{\mu}(\mathbf{r}, t) \quad (4.22)$$

By introducing \mathcal{J}_{μ}^P and \mathcal{J}_{μ}^D , one may rewrite the interaction Hamiltonian as

$$H_I = -\frac{1}{c} \sum_{\nu} \int d^3\mathbf{r} \left[\mathcal{J}_{\mu}^P(\mathbf{r}) + \frac{1}{2} \mathcal{J}_{\mu}^D(\mathbf{r}, t) \right] A_{\nu}(\mathbf{r}, t) \quad (4.23)$$

In order to calculate the mean value of the current density, we have to know the density matrix. The evolution of the density matrix satisfies the following equation of motion in the Schrödinger picture.

$$i\hbar\partial_t\hat{\rho} = [H_{\text{T}}, \hat{\rho}] \quad (4.24)$$

Since the interaction Hamiltonian is switched on at $t \rightarrow -\infty$, the initial condition for the density matrix reads,

$$\lim_{t \rightarrow -\infty} \hat{\rho}(t) = \hat{\rho}_0 \quad (4.25)$$

where $\hat{\rho}_0$ is the density matrix of the equilibrium grand-canonical ensemble of the macrosystem before the perturbation, and satisfies,

$$[H, \hat{\rho}_0] = 0 \quad (4.26)$$

Introducing the Heisenberg representation of the density matrix, the current density and the interaction Hamiltonian,

$$\tilde{\rho}(t) \equiv e^{iHt/\hbar} \hat{\rho}(t) e^{-iHt/\hbar} \quad (4.27)$$

$$\tilde{\mathcal{J}}_\mu \equiv e^{iHt/\hbar} \mathcal{J}_\mu e^{-iHt/\hbar} \quad (4.28)$$

$$\tilde{H}_{\text{I}} \equiv e^{iHt/\hbar} H_{\text{I}} e^{-iHt/\hbar} \quad (4.29)$$

we obtain the equation of the motion in the interaction picture,

$$i\hbar\partial_t\tilde{\rho}(t) = [\tilde{H}_{\text{I}}(t), \tilde{\rho}(t)] \quad (4.30)$$

The formal solution of this equation of motion yields the density matrix,

$$\tilde{\rho}(t) \approx \tilde{\rho}(-\infty) + \frac{1}{i\hbar} \int_{-\infty}^t dt [\tilde{H}_{\text{I}}(t'), \tilde{\rho}(t')] \quad (4.31)$$

To first order in \tilde{H}_{I} , it reduces to

$$\tilde{\rho}(t) \approx \tilde{\rho}(-\infty) + \frac{1}{i\hbar} \int_{-\infty}^t dt [\tilde{H}_{\text{I}}(t'), \tilde{\rho}(-\infty)] \quad (4.32)$$

or

$$\tilde{\rho}(t) \approx \hat{\rho}_0 + \frac{1}{i\hbar} \int_{-\infty}^t dt [\tilde{H}_{\text{I}}(t'), \hat{\rho}_0] \quad (4.33)$$

Here we have very easily gotten the solution of the density matrix in the Heisenberg representation.

Then the corresponding Schrödinger representation becomes,

$$\hat{\rho}(t) \approx \hat{\rho}_0 + e^{-iHt/\hbar} \frac{1}{i\hbar} \int_{-\infty}^t dt \left[\tilde{H}_I(t'), \hat{\rho}_0 \right] e^{iHt/\hbar} \quad (4.34)$$

Now we are ready to calculate the mean total current density, which reads

$$\langle \mathcal{J}_\mu(\mathbf{r}, t) \rangle = \text{Tr} [\hat{\rho}_0 \mathcal{J}_\mu(\mathbf{r}, t)] + \text{Tr} \left\{ e^{-iHt/\hbar} \frac{1}{i\hbar} \int_{-\infty}^t dt \left[\tilde{H}_I(t'), \hat{\rho}_0 \right] e^{iHt/\hbar} \mathcal{J}_\mu(\mathbf{r}, t) \right\} \quad (4.35)$$

Employing the operator identities,

$$\text{Tr}(\hat{A}\hat{B}\hat{C}) = \text{Tr}(\hat{B}\hat{C}\hat{A}) = \text{Tr}(\hat{C}\hat{A}\hat{B}) \quad (4.36)$$

$$\text{Tr}([\hat{A}, \hat{B}]\hat{C}) = \text{Tr}(\hat{B}[\hat{C}, \hat{A}]) \quad (4.37)$$

the mean current reduces to

$$\begin{aligned} \langle \mathcal{J}_\mu(\mathbf{r}, t) \rangle &= \text{Tr} [\hat{\rho}_0 \mathcal{J}_\mu(\mathbf{r}, t)] + \text{Tr} \left\{ \frac{1}{i\hbar} \int_{-\infty}^t dt \hat{\rho}_0 \left[\tilde{\mathcal{J}}_\mu(\mathbf{r}, t), \tilde{H}_I(t') \right] \right\} \\ &= \langle \mathcal{J}_\mu^P(\mathbf{r}) \rangle + \langle \mathcal{J}_\mu^D(\mathbf{r}, t) \rangle + \frac{1}{i\hbar} \int_{-\infty}^t dt \hat{\rho}_0 \langle \left[\tilde{\mathcal{J}}_\mu(\mathbf{r}, t), \tilde{H}_I(t') \right] \rangle \end{aligned} \quad (4.38)$$

Here the mean current density $\langle \mathcal{J}_\mu^D(\mathbf{r}, t) \rangle$ is easily obtained via the definition, which is

$$\langle \mathcal{J}_\mu^D(\mathbf{r}, t) \rangle = -\frac{q^2}{mc} \langle n(\mathbf{r}) \rangle A_\mu(\mathbf{r}, t) \quad (4.39)$$

where $\langle n(\mathbf{r}) \rangle$ is the mean particle number density. Since this current is only due to the external field, it does not exist when $t \rightarrow -\infty$. Therefore the response of the current to the external field is

$$\delta \langle \mathcal{J}_\mu(\mathbf{r}, t) \rangle = \frac{1}{i\hbar} \int_{-\infty}^t dt \langle \left[\tilde{\mathcal{J}}_\mu(\mathbf{r}, t), \tilde{H}_I(t') \right] \rangle - \frac{q^2}{mc} \langle n(\mathbf{r}) \rangle A_\mu(\mathbf{r}, t) \quad (4.40)$$

Substitute Eq. (4.28), (4.20) (4.29) and (4.23) into the commutator in (4.40), and keep only the first order term in $A_\nu(\mathbf{r}', t')$, we obtain the linear response of the current to the external field \mathbf{A} . It is just the macro-current density, which is denoted by,

$$J_\mu(\mathbf{r}, t) = \sum_\nu \int d^3\mathbf{r}' \int_{-\infty}^t dt' \left[C_{\mu\nu}^P(\mathbf{r}, t; \mathbf{r}', t') + C_{\mu\nu}^D(\mathbf{r}, t; \mathbf{r}', t') \right] A_\nu(\mathbf{r}', t') \quad (4.41)$$

with

$$C_{\mu\nu}^P(\mathbf{r}, t; \mathbf{r}', t') \equiv -\frac{1}{\hbar c} \chi_{\mu\nu}^P(\mathbf{r}, t; \mathbf{r}', t') \quad (4.42)$$

$$C_{\mu\nu}^D(\mathbf{r}, t; \mathbf{r}', t') \equiv -\frac{q^2}{mc} \langle n(\mathbf{r}) \rangle \delta_{\mu\nu} \delta(\mathbf{r} - \mathbf{r}') \delta(t - t') \quad (4.43)$$

$$\chi_{\mu\nu}^P(\mathbf{r}, t; \mathbf{r}', t') \equiv -i\theta(t - t') \langle \left[\tilde{\mathcal{J}}_\mu^P(\mathbf{r}, t), \tilde{\mathcal{J}}_\nu^P(\mathbf{r}', t') \right] \rangle \quad (4.44)$$

where $C_{\mu\nu}^P$ and $C_{\mu\nu}^D$ are the susceptibility, and $\tilde{\mathcal{J}}_\nu^P$ is the Heisenberg representation of current density \mathcal{J}_ν^P , *i.e.*

$$\tilde{\mathcal{J}}_\nu^P(\mathbf{r}, t) = e^{iHt/\hbar} \mathcal{J}_\nu^P(\mathbf{r}) e^{-iHt/\hbar} \quad (4.45)$$

To relate these susceptibilities with the polarizability, we need to prove the time-translation invariance of the density-density correlation function, $\chi_{\mu\nu}^P(\mathbf{r}t, \mathbf{r}'t')$. Expanding the right hand side of Eq. (4.44) by substituting Eq.(4.45) gives,

$$\begin{aligned} \chi_{\mu\nu}^P(\mathbf{r}, t; \mathbf{r}', t') &= -i\theta(t - t') \text{Tr} \left\{ \hat{\rho}_0 \left[e^{iHt/\hbar} \mathcal{J}_\mu^P(\mathbf{r}) e^{-iHt/\hbar}, e^{iHt'/\hbar} \mathcal{J}_\nu^P(\mathbf{r}') e^{-iHt'/\hbar} \right] \right\} \\ &= -i\theta(t - t') \text{Tr} \left\{ \hat{\rho}_0 \left[e^{iH(t-t')/\hbar} \mathcal{J}_\mu^P(\mathbf{r}) e^{-iH(t-t')/\hbar}, \mathcal{J}_\nu^P(\mathbf{r}') \right] \right\} \\ &= -i\theta(t - t') \langle [\tilde{\mathcal{J}}_\mu^P(\mathbf{r}, t - t'); \tilde{\mathcal{J}}_\nu^P(\mathbf{r}', 0)] \rangle \\ &= \chi_{\mu\nu}^P(\mathbf{r}, t - t'; \mathbf{r}', 0) \end{aligned}$$

Clearly the correlation function is just the function of $t - t'$. Then we denote it by $\chi_{\mu\nu}^P(\mathbf{r}, \mathbf{r}'; t - t')$.

The Fourier transformation of Eq.(4.41) reads

$$\begin{aligned} J_\mu(\mathbf{r}, \omega) &= \sum_\nu \int d^3\mathbf{r}' [C_{\mu\nu}^P(\mathbf{r}, \mathbf{r}'; \omega) + C_{\mu\nu}^D(\mathbf{r}, \mathbf{r}'; \omega)] A_\nu(\mathbf{r}', \omega) \\ &= -\frac{1}{\hbar c} \sum_\nu \left[\int \chi_{\mu\nu}^P(\mathbf{r}, \mathbf{r}'; \omega) d^3\mathbf{r}' + \frac{\hbar q^2}{m} \langle n(\mathbf{r}) \rangle \delta_{\mu\nu} \right] A_\nu(\mathbf{r}', \omega) \end{aligned}$$

Comparing with Eq.(4.11), one gets the expression of the conductivity and the polarizability tensor

$$\sigma_{\mu\nu}(\mathbf{r}, \omega) = \frac{i}{\hbar\omega} \left[\int \chi_{\mu\nu}^P(\mathbf{r}, \mathbf{r}'; \omega) d^3\mathbf{r}' + \frac{\hbar q^2}{m} \langle n(\mathbf{r}) \rangle \delta_{\mu\nu} \right] \quad (4.46)$$

$$\alpha_{\mu\nu}(\omega) = -\frac{1}{\hbar\omega^2} \left[\int \int \chi_{\mu\nu}^P(\mathbf{r}, \mathbf{r}'; \omega) d^3\mathbf{r} d^3\mathbf{r}' + \frac{\hbar q^2}{m} \langle N \rangle \delta_{\mu\nu} \right] \quad (4.47)$$

where, $\langle N \rangle$ is the total number of particles in the system.

4.3 τ -ORDER CORRELATION FUNCTION AND THE FINITE TEMPERATURE GREEN'S FUNCTION

For convenience, we rewrite the current density in Eq.(4.21) as

$$\begin{aligned} \mathcal{J}_\mu^P(\mathbf{r}) &= \frac{q\hbar}{2m_e i} \sum_\sigma \left[\hat{\Psi}_\sigma^\dagger(\mathbf{r}) \partial_\mu \hat{\Psi}_\sigma(\mathbf{r}) - \left(\partial_\mu \hat{\Psi}_\sigma^\dagger(\mathbf{r}) \right) \hat{\Psi}_\sigma(\mathbf{r}) \right] \\ &= \frac{q\hbar}{2m_e i} \sum_\sigma \int d^3\mathbf{X} d^3\mathbf{X}' \hat{\Psi}_\sigma^\dagger(\mathbf{r} + \mathbf{X}) D_\mu(\mathbf{X}, \mathbf{X}') \hat{\Psi}_\sigma(\mathbf{r} + \mathbf{X}') \end{aligned}$$

with

$$D_\mu(\mathbf{X}, \mathbf{X}') \equiv \delta(\mathbf{X})\delta(\mathbf{X}') \left(\frac{\overrightarrow{\partial}}{\partial X'_\mu} - \frac{\overleftarrow{\partial}}{\partial X_\mu} \right)$$

where " \leftarrow " and " \rightarrow " represent that the differential operator acts onto the function at its left and right, respectively.

Now we turn to the Heisenberg representation of the current operator \mathcal{J}_μ^P in the imaginary time domain. It reads

$$\begin{aligned} \tilde{\mathcal{J}}_\mu^P(\mathbf{r}, \tau) &= e^{H\tau/\hbar} \mathcal{J}_\mu^P(\mathbf{r}) e^{-H\tau/\hbar} \\ &= \left(\frac{q\hbar}{2m_e i} \right)^2 \sum_\sigma \int d^3\mathbf{r} d^3\mathbf{r}' \tilde{\Psi}_\sigma^\dagger(\mathbf{r} + \mathbf{X}, \tau) D_\mu(\mathbf{X}, \mathbf{X}') \tilde{\Psi}_\sigma(\mathbf{r} + \mathbf{X}', \tau) \end{aligned} \quad (4.48)$$

where,

$$\begin{aligned} \tilde{\Psi}_\sigma^\dagger(\mathbf{r}, \tau) &= e^{H\tau/\hbar} \hat{\Psi}_\sigma^\dagger(\mathbf{r}) e^{-H\tau/\hbar} \\ \tilde{\Psi}_\sigma(\mathbf{r}, \tau) &= e^{H\tau/\hbar} \hat{\Psi}_\sigma(\mathbf{r}) e^{-H\tau/\hbar} \end{aligned}$$

The imaginary time τ -order correlation function is defined by

$$\begin{aligned} \mathcal{K}_{\mu\nu}^P(\mathbf{r}\mathbf{r}', \tau) &\equiv -\langle T_\tau [\tilde{\mathcal{J}}_\mu^P(\mathbf{r}, \tau) \tilde{\mathcal{J}}_\nu^P(\mathbf{r}', 0)] \rangle \\ &= -\left(\frac{q\hbar}{2m_e i} \right)^2 \int d^3\mathbf{X} d^3\mathbf{X}' d^3\mathbf{Y} d^3\mathbf{Y}' \sum_{\sigma\sigma'} \langle T_\tau \{ \tilde{\Psi}_\sigma^\dagger(\mathbf{r} + \mathbf{X}, \tau) D_\mu(\mathbf{X}, \mathbf{X}') \tilde{\Psi}_\sigma(\mathbf{r} + \mathbf{X}', \tau) \\ &\quad \tilde{\Psi}_{\sigma'}^\dagger(\mathbf{r}' + \mathbf{Y}, 0) D_\nu(\mathbf{Y}, \mathbf{Y}') \tilde{\Psi}_{\sigma'}(\mathbf{r}' + \mathbf{Y}', 0) \} \rangle \\ &= \left(\frac{q\hbar}{2m_e i} \right)^2 \int d^3\mathbf{X} d^3\mathbf{X}' d^3\mathbf{Y} d^3\mathbf{Y}' D_\mu(\mathbf{X}, \mathbf{X}') D_\nu(\mathbf{Y}, \mathbf{Y}') \mathcal{L}(\tau) \end{aligned} \quad (4.49)$$

with

$$\mathcal{L}(\tau) \equiv -\sum_{\sigma\sigma'} \langle T_\tau \left\{ \tilde{\Psi}_\sigma^\dagger(\mathbf{r} + \mathbf{X}, \tau) \tilde{\Psi}_\sigma(\mathbf{r} + \mathbf{X}', \tau) \tilde{\Psi}_{\sigma'}^\dagger(\mathbf{r}' + \mathbf{Y}, 0) \tilde{\Psi}_{\sigma'}(\mathbf{r}' + \mathbf{Y}', 0) \right\} \rangle$$

The only useful combination given by Wick's theorem for the current case is as follows

$$\begin{aligned} \mathcal{L}(\tau) &= -\sum_{\sigma\sigma'} \langle T_\tau \left\{ \tilde{\Psi}_\sigma^\dagger(\mathbf{r} + \mathbf{X}, \tau) \bullet\bullet \tilde{\Psi}_\sigma(\mathbf{r} + \mathbf{X}', \tau) \bullet \tilde{\Psi}_{\sigma'}^\dagger(\mathbf{r}' + \mathbf{Y}, 0) \bullet \tilde{\Psi}_{\sigma'}(\mathbf{r}' + \mathbf{Y}', 0) \bullet\bullet \right\} \rangle \\ &= \sum_{\sigma\sigma'} \langle T_\tau \left\{ \tilde{\Psi}_\sigma(\mathbf{r} + \mathbf{X}', \tau) \bullet \tilde{\Psi}_{\sigma'}^\dagger(\mathbf{r}' + \mathbf{Y}, 0) \bullet \tilde{\Psi}_{\sigma'}(\mathbf{r}' + \mathbf{Y}', 0) \bullet\bullet \tilde{\Psi}_\sigma^\dagger(\mathbf{r} + \mathbf{X}, \tau) \bullet\bullet \right\} \rangle \\ &= \sum_{\sigma\sigma'} \mathcal{G}_{\sigma\sigma'}(\mathbf{r} + \mathbf{X}', \mathbf{r}' + \mathbf{Y}; \tau) \mathcal{G}_{\sigma'\sigma}(\mathbf{r}' + \mathbf{Y}', \mathbf{r} + \mathbf{X}; -\tau) \\ &= (2s+1) \mathcal{G}(\mathbf{r} + \mathbf{X}', \mathbf{r}' + \mathbf{Y}; \tau) \mathcal{G}(\mathbf{r}' + \mathbf{Y}', \mathbf{r} + \mathbf{X}; -\tau) \end{aligned} \quad (4.50)$$

The Fourier transformation yields,

$$\mathcal{L}(ip_n) = \frac{(2s+1)}{\beta\hbar} \sum_{i\omega_n} \mathcal{G}(\mathbf{r} + \mathbf{X}', \mathbf{r}' + \mathbf{Y}; i\omega_n) \mathcal{G}(\mathbf{r}' + \mathbf{Y}', \mathbf{r} + \mathbf{X}; i\omega_n - ip_n) \quad (4.51)$$

Consequently the Fourier transformation of the τ -order correlation function reads,

$$\begin{aligned} \mathcal{K}_{\mu\nu}^P(\mathbf{r}, \mathbf{r}'; ip_n) = & -\frac{(2s+1)\hbar q^2}{4\beta m^2} \sum_{i\omega_n} \int d^3\mathbf{X} d^3\mathbf{X}' d^3\mathbf{Y} d^3\mathbf{Y}' D_\mu(\mathbf{X}, \mathbf{X}') D_\nu(\mathbf{Y}, \mathbf{Y}') \\ & \mathcal{G}(\mathbf{r} + \mathbf{X}', \mathbf{r}' + \mathbf{Y}; i\omega_n) \mathcal{G}(\mathbf{r}' + \mathbf{Y}', \mathbf{r} + \mathbf{X}; i\omega_n - ip_n) \end{aligned} \quad (4.52)$$

where, ip_n is the Matsubara frequency for Bosons.

Considering the following integral,

$$\begin{aligned} I_1(\mathbf{X}, \mathbf{X}') &= \int d^3\mathbf{Y} d^3\mathbf{Y}' D_\nu(\mathbf{Y}, \mathbf{Y}') \mathcal{G}(\mathbf{r} + \mathbf{X}', \mathbf{r}' + \mathbf{Y}; i\omega_n) \mathcal{G}(\mathbf{r}' + \mathbf{Y}', \mathbf{r} + \mathbf{X}; i\omega_n - ip_n) \\ &= \int d^3\mathbf{Y} d^3\mathbf{Y}' \delta(\mathbf{Y}) \delta(\mathbf{Y}') \left\{ \mathcal{G}(\mathbf{r} + \mathbf{X}', \mathbf{r}' + \mathbf{Y}; i\omega_n) \frac{\partial}{\partial Y'_\nu} \mathcal{G}(\mathbf{r}' + \mathbf{Y}', \mathbf{r} + \mathbf{X}; i\omega_n - ip_n) \right. \\ &\quad \left. - \frac{\partial}{\partial Y_\nu} \mathcal{G}(\mathbf{r} + \mathbf{X}', \mathbf{r}' + \mathbf{Y}; i\omega_n) \mathcal{G}(\mathbf{r}' + \mathbf{Y}', \mathbf{r} + \mathbf{X}; i\omega_n - ip_n) \right\} \\ &= \mathcal{G}(\mathbf{r} + \mathbf{X}', \mathbf{r}'; i\omega_n) \frac{\partial}{\partial x'_\nu} \mathcal{G}(\mathbf{r}', \mathbf{r} + \mathbf{X}; i\omega_n - ip_n) \\ &\quad - \frac{\partial}{\partial x'_\nu} \mathcal{G}(\mathbf{r} + \mathbf{X}', \mathbf{r}'; i\omega_n) \mathcal{G}(\mathbf{r}', \mathbf{r} + \mathbf{X}; i\omega_n - ip_n) \end{aligned} \quad (4.53)$$

From this integral, we can then construct another one,

$$\begin{aligned} I_2 &= \int d^3\mathbf{X} d^3\mathbf{X}' D_\nu(\mathbf{X}, \mathbf{X}') I_1(\mathbf{X}, \mathbf{X}') \\ &= \int d^3\mathbf{X} d^3\mathbf{X}' \delta(\mathbf{X}) \delta(\mathbf{X}') \left\{ \frac{\partial}{\partial X'_\mu} \mathcal{G}(\mathbf{r} + \mathbf{X}', \mathbf{r}'; i\omega_n) \frac{\partial}{\partial x'_\nu} \mathcal{G}(\mathbf{r}', \mathbf{r} + \mathbf{X}; i\omega_n - ip_n) \right. \\ &\quad - \mathcal{G}(\mathbf{r} + \mathbf{X}', \mathbf{r}'; i\omega_n) \frac{\partial}{\partial X_\mu} \frac{\partial}{\partial x'_\nu} \mathcal{G}(\mathbf{r}', \mathbf{r} + \mathbf{X}; i\omega_n - ip_n) \\ &\quad - \frac{\partial}{\partial X'_\mu} \frac{\partial}{\partial x'_\nu} \mathcal{G}(\mathbf{r} + \mathbf{X}', \mathbf{r}'; i\omega_n) \mathcal{G}(\mathbf{r}', \mathbf{r} + \mathbf{X}; i\omega_n - ip_n) \\ &\quad \left. + \frac{\partial}{\partial x'_\nu} \mathcal{G}(\mathbf{r} + \mathbf{X}', \mathbf{r}'; i\omega_n) \frac{\partial}{\partial X_\mu} \mathcal{G}(\mathbf{r}', \mathbf{r} + \mathbf{X}; i\omega_n - ip_n) \right\} \\ &= \frac{\partial}{\partial x_\mu} \mathcal{G}(\mathbf{r}, \mathbf{r}'; i\omega_n) \frac{\partial}{\partial x'_\nu} \mathcal{G}(\mathbf{r}', \mathbf{r}; i\omega_n - ip_n) - \mathcal{G}(\mathbf{r}, \mathbf{r}'; i\omega_n) \frac{\partial^2}{\partial x_\mu \partial x'_\nu} \mathcal{G}(\mathbf{r}', \mathbf{r}; i\omega_n - ip_n) \\ &\quad - \frac{\partial^2}{\partial x_\mu \partial x'_\nu} \mathcal{G}(\mathbf{r}, \mathbf{r}'; i\omega_n) \mathcal{G}(\mathbf{r}', \mathbf{r}; i\omega_n - ip_n) + \frac{\partial}{\partial x'_\nu} \mathcal{G}(\mathbf{r}, \mathbf{r}'; i\omega_n) \frac{\partial}{\partial x_\mu} \mathcal{G}(\mathbf{r}', \mathbf{r}; i\omega_n - ip_n) \end{aligned} \quad (4.54)$$

Clearly the integral I_2 is the integral in Eq.(4.52). Substitute it in this equation, τ -order correlation function reduces to,

$$\mathcal{K}_{\mu\nu}^P(\mathbf{r}, \mathbf{r}'; ip_n) = \frac{(2s+1)\hbar q^2}{4\beta m^2} \mathcal{Q}_{\mu\nu}(\mathbf{r}, \mathbf{r}'; ip_n) \quad (4.55)$$

with

$$\begin{aligned} \mathcal{Q}_{\mu\nu}(\mathbf{r}, \mathbf{r}'; ip_n) &\equiv \sum_{i\omega_n} \left\{ \frac{\partial^2}{\partial x_\mu \partial x'_\nu} \mathcal{G}(\mathbf{r}, \mathbf{r}'; i\omega_n) \mathcal{G}(\mathbf{r}', \mathbf{r}; i\omega_n - ip_n) + \mathcal{G}(\mathbf{r}, \mathbf{r}'; i\omega_n) \frac{\partial^2}{\partial x_\mu \partial x'_\nu} \mathcal{G}(\mathbf{r}', \mathbf{r}; i\omega_n - ip_n) \right. \\ &\quad \left. - \frac{\partial}{\partial x_\mu} \mathcal{G}(\mathbf{r}, \mathbf{r}'; i\omega_n) \frac{\partial}{\partial x'_\nu} \mathcal{G}(\mathbf{r}', \mathbf{r}; i\omega_n - ip_n) - \frac{\partial}{\partial x'_\nu} \mathcal{G}(\mathbf{r}, \mathbf{r}'; i\omega_n) \frac{\partial}{\partial x_\mu} \mathcal{G}(\mathbf{r}', \mathbf{r}; i\omega_n - ip_n) \right\} \end{aligned} \quad (4.56)$$

4.4 τ -ORDER CORRELATION FUNCTION FOR THE POLARIZABILITY FOR SPHERICALLY SYMMETRIC SYSTEMS

For the spherically symmetric systems, only three equivalent principal tensors contribute to the conductivity and the polarization due to the cancelation of the off diagonal elements. Therefore we consider here only the principal element along z -direction, *i.e.*, $\mathcal{Q}_{33}(\mathbf{r}, \mathbf{r}', ip_n)$. It will be obtained by integrating over the angular coordinates of \mathbf{r} and \mathbf{r}' . According to the definition of the radial Green's function Eq.(2.46), the spherical polar coordinate representation of the derivative in z direction,

$$\frac{\partial}{\partial z} = \cos\theta \frac{\partial}{\partial r} + \frac{1}{r} \sin^2\theta \frac{\partial}{\partial \cos\theta} \quad (4.57)$$

and the recurrence relation of the spherical harmonic function, we have

$$\mathcal{Q}_{33}(r, r'; ip_n) = \int d\Omega d\Omega' \mathcal{Q}_{33}(\mathbf{r}, \mathbf{r}', ip_n) = Q_{33}(r, r'; ip_n) + Q_{33}^*(r', r; ip_n) \quad (4.58)$$

with

$$\begin{aligned}
Q_{33}(r, r'; ip_n) &\equiv \frac{1}{3} \sum_{l, i\omega_n} \frac{\partial^2 G_l(r, r'; i\omega_n)}{\partial r \partial r'} [l G_{l-1}(r', r; i\omega_n - ip_n) + (l+1) G_{l+1}(r', r; i\omega_n - ip_n)] \\
&\quad - \frac{1}{3} \sum_{l, i\omega_n} \frac{\partial G_l(r, r'; i\omega_n)}{\partial r} \frac{\partial}{\partial r'} [l G_{l-1}(r', r; i\omega_n - ip_n) + (l+1) G_{l+1}(r', r; i\omega_n - ip_n)] \\
&\quad + \frac{2}{3r} \sum_{l, i\omega_n} \frac{\partial G_l(r, r'; i\omega_n)}{\partial r'} [l^2 G_{l-1}(r', r; i\omega_n - ip_n) - (l+1)^2 G_{l+1}(r', r; i\omega_n - ip_n)] \\
&\quad + \frac{2}{3r'} \sum_{l, i\omega_n} \frac{\partial G_l(r, r'; i\omega_n)}{\partial r} [l^2 G_{l-1}(r', r; i\omega_n - ip_n) - (l+1)^2 G_{l+1}(r', r; i\omega_n - ip_n)] \\
&\quad + \frac{4}{3rr'} \sum_{l, i\omega_n} l^3 G_l(r, r'; i\omega_n) G_{l-1}(r', r; i\omega_n - ip_n) \tag{4.59}
\end{aligned}$$

Introducing the transformations:

$$\tilde{Q}_{33}(r, r'; ip_n) = r^2 r'^2 Q_{33}(r, r'; ip_n)$$

$$\tilde{Q}_{33} = r^2 r'^2 \hat{Q}_{33}(r, r'; ip_n)$$

$$\tilde{G}_l(r, r'; i\omega_n) = rr' G_l(r, r'; i\omega_n)$$

Eq.(4.58) and (4.59) become,

$$\tilde{Q}_{33}(r, r'; ip_n) = \tilde{Q}_{33}(r, r'; ip_n) + \tilde{Q}_{33}^*(r', r; ip_n) \tag{4.60}$$

with

$$\begin{aligned}
\tilde{Q}_{33}(r, r'; ip_n) &\equiv \frac{1}{3} \sum_{l, i\omega_n} \frac{\partial^2 \tilde{G}_l(r, r'; i\omega_n)}{\partial r \partial r'} [l \tilde{G}_{l-1}(r', r; i\omega_n - ip_n) + (l+1) \tilde{G}_{l+1}(r', r; i\omega_n - ip_n)] \\
&\quad - \frac{1}{3} \sum_{l, i\omega_n} \frac{\partial \tilde{G}_l(r, r'; i\omega_n)}{\partial r} \frac{\partial}{\partial r'} [l \tilde{G}_{l-1}(r', r; i\omega_n - ip_n) + (l+1) \tilde{G}_{l+1}(r', r; i\omega_n - ip_n)] \\
&\quad + \frac{2}{3r} \sum_{l, i\omega_n} \frac{\partial \tilde{G}_l(r, r'; i\omega_n)}{\partial r'} [l^2 \tilde{G}_{l-1}(r', r; i\omega_n - ip_n) - (l+1)^2 \tilde{G}_{l+1}(r', r; i\omega_n - ip_n)] \\
&\quad + \frac{2}{3r'} \sum_{l, i\omega_n} \frac{\partial \tilde{G}_l(r, r'; i\omega_n)}{\partial r} [l^2 \tilde{G}_{l-1}(r', r; i\omega_n - ip_n) - (l+1)^2 \tilde{G}_{l+1}(r', r; i\omega_n - ip_n)] \\
&\quad + \frac{4}{3rr'} \sum_{l, i\omega_n} l^3 \tilde{G}_l(r, r'; i\omega_n) \tilde{G}_{l-1}(r', r; i\omega_n - ip_n) \tag{4.61}
\end{aligned}$$

One may see through Eq.(4.61) that $\tilde{Q}_{33}(r, r'; ip_n)$ is symmetric under exchanging r and r' . Thus, it is real, *i.e.*,

$$\tilde{Q}_{33}(r, r'; ip_n) = 2\text{Re} \tilde{Q}_{33}(r, r'; ip_n) \quad (4.62)$$

Finally, we get the principal tensors of the τ -order correlation function for spherically symmetric systems along z -direction,

$$\tilde{\mathcal{K}}_{33}^P(r, r'; ip_n) = \int d\Omega d\Omega' \tilde{\mathcal{K}}_{33}^P(\mathbf{r}, \mathbf{r}'; ip_n) = \frac{(2s+1)\hbar q^2}{2\beta m^2} \text{Re} \tilde{Q}_{33}(r, r'; ip_n) \quad (4.63)$$

where

$$\tilde{\mathcal{K}}_{33}^P(r, r'; ip_n) = r^2 r'^2 \mathcal{K}_{33}^P(r, r'; ip_n)$$

4.5 DYNAMICAL POLARIZABILITY AND OPTICAL ABSORPTION CROSS SECTION

Employing the Lehmann representation (see for example, Fetter and Walecka [61]), it can be easily shown that the Matsubara frequency dependence of the susceptibility defined in Sec.4.2 is the same to that of the τ -order correlation function in Sec.4.3. Also, converting between the expressions in the real and the Matsubara frequency domains is just the analytical continuation. Hence the polarizability defined by (4.47) immediately changes into their counterpart in Matsubara frequency domain, and are related to the τ -order correlation function by

$$\alpha_{\mu\nu}(ip_n) = -\frac{1}{\hbar(ip_n)^2} \left[\int \int \mathcal{K}_{\mu\nu}^P(\mathbf{r}, \mathbf{r}'; ip_n) d^3\mathbf{r} d^3\mathbf{r}' + \frac{\hbar q^2}{m} \langle N \rangle \delta_{\mu\nu} \right] \quad (4.64)$$

For the spherically symmetric systems, the integral over the angular coordinates gives

$$\alpha_{\mu\nu}(ip_n) = -\frac{1}{\hbar(ip_n)^2} \left[\int \int \tilde{\mathcal{K}}_{\mu\nu}^P(r, r'; ip_n) dr dr' + \frac{\hbar q^2}{m} \langle N \rangle \delta_{\mu\nu} \right] \quad (4.65)$$

Due to the isotropic nature of the system, all the principal tensors are the same and the others are zero. We consider only one of them, denoted by α ,

$$\alpha(ip_n) = -\frac{1}{\hbar(ip_n)^2} \left[\int \int \tilde{\mathcal{K}}_{33}^P(r, r'; ip_n) dr dr' + \frac{\hbar q^2}{m} \langle N \rangle \delta_{\mu\nu} \right] \quad (4.66)$$

where $\tilde{\mathcal{K}}_{33}^{\text{P}}(r, r'; ip_n)$ is defined in the last section.

If the close form of $\alpha(z)$ is known, the real frequency dependence can be simply obtained by the analytical continuation

$$\alpha(\omega) = \lim_{\eta \rightarrow 0^+} \alpha(\omega + i\eta) \quad (4.67)$$

Unfortunately, we usually do not have the analytical expression of it. In the Matsubara frequency domain, however, we can calculate only the polarizabilities at the discrete points $\{z_n = ip_n, n = 1, 2, \dots, N\}$ (where $n = 0$ is dropped, it need special treatment). These discrete values $\alpha(z_n)$ can be fitted to the N -point Padé approximant $P_N(z)$, through which the analytical continuation can be made.

In the Thiele's reciprocal-difference method [73], the N -point Padé approximant $P_N(z)$ is expressed by a continued fraction

$$P_N(z) = \frac{c_1}{1+} \frac{c_2 (z - z_1)}{1+} \dots \frac{c_N (z - z_{N-1})}{1 + (z - z_{N-1}) g_{N+1}(z)} \quad (4.68)$$

where the coefficients c_i are to be determined so that

$$P_N(z_i) = \alpha(z_i), \quad , i = 1, 2, \dots, N \quad (4.69)$$

The coefficients c_i are then given by the recursion relation

$$g_1(z_i) = \alpha(z_i), \quad c_i = g_i(z_i), \quad i = 1, 2, \dots, N \quad (4.70)$$

$$g_\nu(z_i) = \frac{g_{\nu-1}(z_{\nu-1}) - g_{\nu-1}(z)}{(z - z_{\nu-1}) g_{\nu-1}(z)}, \quad \nu \geq 2 \quad (4.71)$$

This Padé approximant can further reduce to

$$P_N(z) = \frac{A_N(z)}{B_N(z)} \quad (4.72)$$

where $A_N(z)$ and $B_N(z)$ are the polynomials of order $(N-1)/2$ for odd integer N . For the even integer N , however, the orders of $A_N(z)$ and $B_N(z)$ are $(N-2)/2$ and $N/2$, respectively. They satisfy the following recursion relations

$$A_{n+1}(z) = A_n(z) + (z - z_n) c_{n+1} A_{n-1}(z) \quad (4.73)$$

$$B_{n+1}(z) = B_n(z) + (z - z_n) c_{n+1} B_{n-1}(z) \quad (4.74)$$

where

$$A_0 = 0, \quad A_1 = a_1, \quad B_0 = B_1 = 1 \quad (4.75)$$

CHAPTER 5

APPLICATIONS TO SPHERICALLY SYMMETRIC NANOPARTICLES

5.1 SYSTEMS AND BACKGROUND POTENTIAL

The dynamical response of the conduction electrons in metallic nanoparticles has been a subject of numerous experimental and theoretical researches, which results in the specific optical absorption at 400 ~ 600nm range. The main feature is the surface plasmon oscillation of these electrons with respect to the positive charged background. These conduction electrons are delocalized and able to explore the entire volume of the metallic nanoparticles without being substantially scattered by the ionic cores [44]. Thus the jellium model is used to approximate the ionic cores by a homogenous positively charged background. The corresponding positive charge density is

$$\rho_{\text{IO}} = \frac{3e}{4\pi r_s^3} \Theta(R - r) \quad (5.1)$$

where $\Theta(x)$ is a step function. The size of the nanoparticles is measured by the radius of the N -atom jellium sphere, R , is related to the Wigner-Seitz radius r_s for bulk samples by

$$R = r_s N^{1/3} \quad (5.2)$$

A simple electrostatics calculation gives the background potential felt by the electrons,

$$U(r) = \begin{cases} \frac{Ne^2}{2R} \left[\left(\frac{r}{R} \right)^2 - 3 \right], & r \leq R \\ -\frac{Ne^2}{r}, & r > R \end{cases} \quad (5.3)$$

In this hybrid approximation, the interaction of ionic cores on the electrons is replaced by this average field, while the correlation effect of the many-conduction-electron system is treated quantum mechanically by the self-consistent DRPA developed in the previous chapters. In the current research, we focus on the spherically symmetric metallic Sodium and Gold nanoparticles, distinguished by the bulk values of the Wigner-Seitz radius r_s .

5.2 COMPUTATIONAL PROCEDURES

5.2.1 INITIAL GREEN'S FUNCTION AND A MODEL POTENTIAL

To start a self-consistent iteration on the Dyson equation (2.85) or on the algebraic finite element form (3.73), an initial Green's function is required to compute the self-energy. There is almost no confinement on the initial Green's function. However a better guess results in a shorter time for the Green's function to converge. Then a better model potential is needed. The spherical square potential with finite depth is the simplest choice. Even though it can give a rather good description of the static electron properties, the step function like shape at the boundary can not reproduce physically the finite size effect. The effective potential obtained in the self-consistent density functional computations is an ideal candidate, but it is given by the numerical data [37]. The numerical fitting to the data shows that it decays exponentially outside the nanoparticle with the screening length L_s about one third of the bulk Fermi wavelength. A combination of this two potentials yields a model potential

$$U_m(r) = \begin{cases} -V_0, & r \leq R \\ -V_0 e^{(R-r)/L_s}, & r > R \end{cases} \quad (5.4)$$

with

$$V_0 = W_B + \frac{E_F}{(1 + \delta/R)^2} \quad (5.5)$$

where W_B and E_F are the bulk work function and Fermi energy, respectively. δ is a measure of the characteristic length of the electron leakage of a nanoparticle [37]. The second term in the definition of V_0 above is actually a Fermi energy of the free electron gas confined in a sphere of radius $(R + \delta)$, which is often involved in the shell model description of ground electronic state of nanoparticles [17].

Replacing the background potential $U(r)$ in the definition of $H_{ij}^0(l)$ in eq.(3.77) with $U_m(r)$ and ignoring $\Sigma_{ij}^{\text{HF}} = 0$ in eq.(3.89), the solution of the generalized algebraic eigenvalue equation (3.87) gives a set of eigenstates $\{\varphi_{ln}^0\}$ and eigenvalues $\{\epsilon_{ln}^0\}$. Then the initial Green's function reads

$$\tilde{G}_{ij}^0(i\Omega_n, l) \equiv \sum_n \frac{\tilde{\varphi}_{ln}^0(r_i) \tilde{\varphi}_{ln}^0(r_j)}{i\Omega_n - \epsilon_{ln}^0 + \mu} \quad (5.6)$$

where the chemical potential μ takes such a value that the mean electron number obtained through this Green's function equals to the total number of conduction electrons in the nanoparticle.

5.2.2 AUXILIARY GREEN'S FUNCTION FOR FREQUENCY SUMMATION

In calculating the mean electron density or the Hartree self-energy in this work, we often encounter the frequency summation on the Green's function. However, we have to cut off the summation at some finite frequency $i\omega_M$. Sometimes we can not make it very large due to limitations computer resources. The smaller cutoff will definitely introduce considerable systematical error/deviation because our Green's function decays with frequency asymptotically following the $1/\omega_n$ law. The contributions beyond the cutoff frequency should be somehow compensated. To do this, one usually introduces an auxiliary Green's function that shows the same asymptotical behavior of the original Green's function and can be analytically summed up to infinite frequencies. The Green's function built up in Eq.(3.91) of Sec.3.3 under the Hartree-Fock approximation satisfies this requirement and is then used as the auxiliary one in this work. Here we ignore subscripts and rewrite it as

$$\tilde{G}_l^A(r, r'; i\omega_n) \equiv \sum_n \frac{\tilde{\varphi}_{ln}(r) \tilde{\varphi}_{ln}^*(r')}{i\omega_n - \epsilon_{ln} + \mu} \quad (5.7)$$

where $\tilde{\varphi}_{ln}$ and ϵ_{ln} are obtained by solving the finite element form of the radial Hartree-Fock equation, *i.e.*, Eq.(3.87).

The frequency summation of this auxiliary Green's function can be easily obtained by considering the following Cauchy integral (the integral contour is shown in Fig.5.1),

$$I_R = \lim_{R \rightarrow \infty} \frac{1}{2\pi i} \oint_C \frac{dz e^{z\eta}}{(e^{\beta\hbar z} + 1)(z - \lambda)} \quad (5.8)$$

where $\eta \rightarrow 0^+$ ensures that the integrand is finite as $Re z \rightarrow -\infty$. Obviously, the integrand has poles at $x = \lambda$ along the real axis and at $z_n = \pm \frac{i(2n+1)\pi}{\beta\hbar} = i\omega_n$, along the imaginary axis. Here the poles z_n are just the

Matsubara frequencies for fermions. There will be countable infinity poles along the imaginary axis as $R \rightarrow \infty$. In the same limit, it can be shown that the integrand $f(z) = e^{z\eta} / [(e^{\beta\hbar z} + 1)(z - \lambda)]$ goes to zero. Thus Jordan's lemma [74] implies

$$\lim_{R \rightarrow \infty} I_R = 0 \quad (5.9)$$

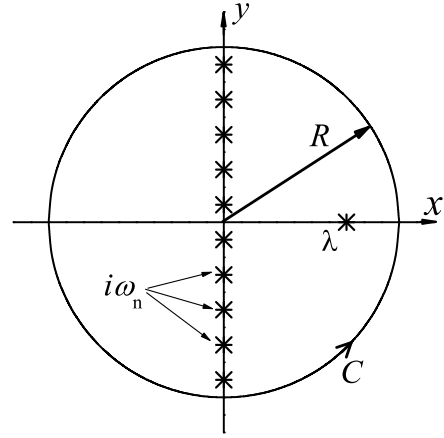


Figure 5.1: Integral contour

While the residue theorem says that this integral equals to the summation of all the residues inside the contour C . The residue for the pole λ is $1/(e^{\beta\hbar\lambda} + 1)$, and the one for pole $z_n = i\omega_n$ is $-1/[\beta(i\omega_n - \lambda)]$. Therefore we have

$$\lim_{\eta \rightarrow 0^+} \frac{1}{\beta\hbar} \sum_{i\omega_n} \frac{e^{i\omega_n\eta}}{i\omega_n - \lambda} = \lim_{\eta \rightarrow 0^+} \frac{e^{\lambda\eta}}{e^{\beta\hbar\lambda} + 1} = \frac{1}{e^{\beta\hbar\lambda} + 1} \quad (5.10)$$

This gives the frequency summation for the auxiliary Green's function,

$$\frac{1}{\beta\hbar} \sum_{i\omega_n} \tilde{G}_l^A(r, r'; i\omega_n) = \sum_n \frac{\tilde{\varphi}_{ln}(r) \tilde{\varphi}_{ln}(r')}{e^{\beta(\epsilon_{ln} - \mu)} + 1} \quad (5.11)$$

We drop \hbar in the denominator of this equation because $(\epsilon_{ln} - \mu)$ has the dimension of energy.

According to the above result, the frequency summation of the Green's function can be expressed as

$$\frac{1}{\beta\hbar} \sum_{i\omega_n} \tilde{G}_l(r, r'; i\omega_n) = \sum_n \frac{\tilde{\varphi}_{ln}(r) \tilde{\varphi}_{ln}(r')}{e^{\beta(\epsilon_{ln} - \mu)} + 1} + \frac{1}{\beta\hbar} \sum_{i\omega_n = -i\omega_M}^{i\omega_M} [\tilde{G}_l(r, r'; i\omega_n) - \tilde{G}_l^A(r, r'; i\omega_n)] \quad (5.12)$$

Here the first term is the infinite sum, while the second term is the finite one which decreases with the frequency according to a $1/(i\omega_n)^2$ law.

5.2.3 DETERMINING THE CHEMICAL POTENTIAL

The mean electron number density reads

$$\langle n(\mathbf{r}) \rangle = \text{tr} \mathcal{G}(\mathbf{r}, \mathbf{r}; \tau = -\eta) \quad (5.13)$$

where $\eta \rightarrow 0^+$. The Fourier transformation defined in Eq.(2.15) gives

$$\langle n(\mathbf{r}) \rangle = 2 \sum_{lm} |Y_{lm}(\theta, \varphi)|^2 \frac{1}{\beta\hbar} \sum_{i\omega} e^{i\omega_n\eta} G_l(r, r; i\omega_n) \quad (5.14)$$

Integrating over the angular coordinates give the radial electron distribution,

$$\begin{aligned} \langle n(r) \rangle &= \int d\Omega \langle n(\mathbf{r}) \rangle \\ &= \frac{2}{r^2} \sum_l (2l+1) \frac{1}{\beta\hbar} \sum_{i\omega} e^{i\omega_n\eta} \tilde{G}_l(r, r; i\omega_n) \end{aligned} \quad (5.15)$$

Finally the mean electron number is calculated by the following integral

$$\langle N \rangle = \int \langle n(r) \rangle r^2 dr \quad (5.16)$$

Here the frequency can be computed by the method described in Eq.(5.12). Obviously, the mean electron number is a function of the chemical potential. Changing it results in the change of the means electron number. However the total conduction electron number remains unchanged. Therefore the value of the chemical potential is such an one that makes the mean electron number equals to the total conduction electrons. To match the mean electron number with the total conduction electrons, a binary searching is used in the current work.

5.2.4 FEEDBACK METHOD AND CONVERGING CRITERIA

In order to accelerate the convergence of the self-consistent iteration of the Green's function and the self-energy through Dyson equations, the feedback method is employed in the self-energy iteration. It is formally expressed by

$$\tilde{\Sigma}^m = \lambda \tilde{\Sigma}^{m-1} + (1 - \lambda) \tilde{\Sigma}_0^m \quad (5.17)$$

where the self-energy matrix $\tilde{\Sigma}_0^m$ in the m -th iteration is the one calculated directly from Eq.(2.87) using the m -th iteration of the Green's function. The parameter $0 \leq \lambda < 1$ measures the strength of feedback. This iteration transfers back to the

original one when $\lambda = 0$. The parameter λ is something like a damping coefficients. There is a critical value λ_c at which the iteration spends the shortest time to converge. It converges very slowly as long as $\lambda > \lambda_c$, but will not converge as $\lambda < \lambda_c$. There is no prior knowledge of what value it should take, and we have no way but try different values. Fig.5.2 shows the variation of the chemical potential with the number of iterations for a test case of 1 nm Gold particles at temperature $T=2500\text{K}$. $\lambda = 0.75$ is a critical case with shortest iterations. The oscillation will appear when the feedback parameter is too small, for example, when $\lambda < 0.7006$, and the iteration will never converge.

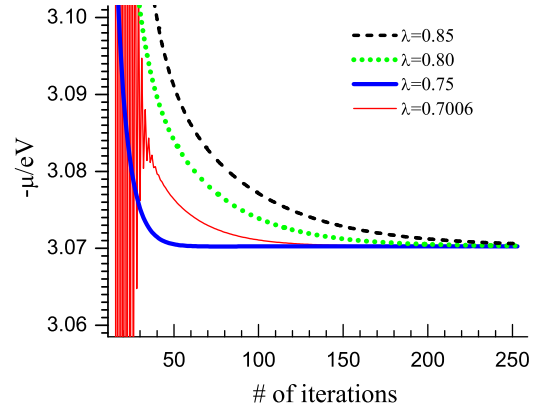


Figure 5.2: Variation of the chemical potential with the number of iterations. For a 1 nm Gold nanoparticle, at temperature $T=2500\text{ K}$, the spatial interval of the mesh $h = \lambda_F/8$.

To monitor the self-consistent iterations, one can also observe the variation of either the Green's function or the self-energy between two successive iterations. The self-energy is usually more sensitive than Green's function. Therefore, in this research, we trace the variation of the self-energy. The relative error of the self-energy matrix in two successive iterations is calculated by

$$\delta_{\Sigma} \equiv \left\{ \frac{\sum_{i\omega_n l, i, j} |\tilde{\Sigma}_l^m(r_i, r_j; i\omega_n) - \tilde{\Sigma}_l^{m-1}(r_i, r_j; i\omega_n)|^2}{\sum_{i\omega_n l, m, n} |\tilde{\Sigma}_l^m(r_i, r_j; i\omega_n)|^2} \right\}^{1/2} \quad (5.18)$$

The iteration will end as soon at the relative error δ_{Σ} satisfies the criteria.

$$\delta_{\Sigma} < \epsilon_{\Sigma} \quad (5.19)$$

where ϵ_{Σ} is the required precision (shown by the horizontal dashed line in Fig.5.3).

Similarly, the error on the Green's function is estimated by

$$\delta_G \equiv \left\{ \frac{\sum_{i\omega_n l, i, j} |\tilde{G}_l^m(r_i, r_j; i\omega_n) - \tilde{G}_l^{m-1}(r_i, r_j; i\omega_n)|^2}{\sum_{i\omega_n l, m, n} |\tilde{G}_l^m(r_i, r_j; i\omega_n)|^2} \right\}^{1/2} \quad (5.20)$$

In Fig.(5.3) and Fig.5.4 plotted are the variation of the relative errors on the self-energy and the Green's function, which show similar picture as observed in Fig.5.2.

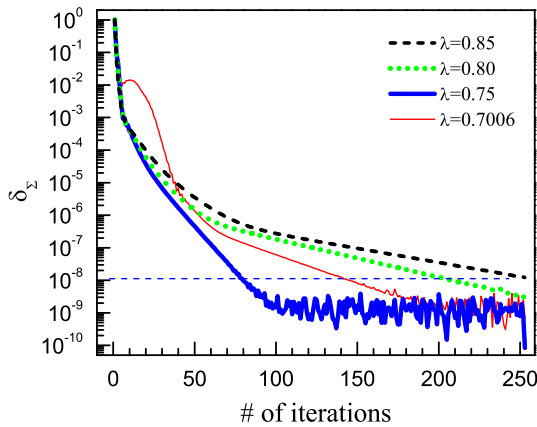


Figure 5.3: Variation of the relative error on the self-energy in two successive iterations with the times of iteration

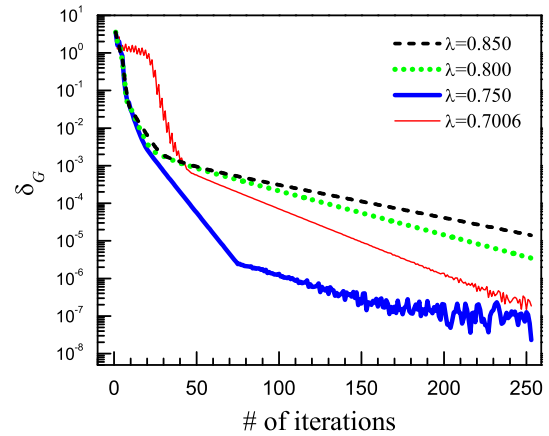


Figure 5.4: Variation of the relative error on the Green's function in two successive iterations with the times of iteration

5.2.5 ANGULAR QUANTUM NUMBER AND FREQUENCY CUTOFF, TEMPERATURE AND MESH INTERVAL

To start any practical computation, one has to set finite cutoffs for the angular quantum number and the Matsubara frequency, as well as the temperature and the size of intervals for the spatial mesh. We estimate these parameters in the Hartree-Fock approximation. The main reason is that the program consumes much less time to get a converge result in this approximation. Nevertheless this approximation has already included most of the contribution of electron correlation. Now let us consider the

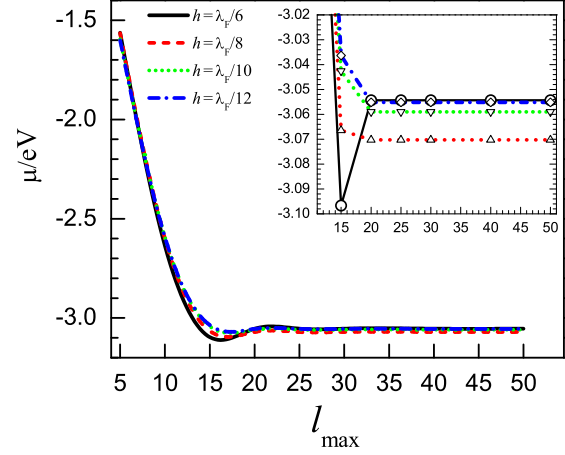


Figure 5.5: Variation of the chemical potential with the angular quantum number cutoff.

changes of the chemical potential with the angular quantum number cutoff denoted by l_{\max} for the meshes with different intervals. Shown in Fig.5.5 are the angular momentum cutoff dependence of the chemical potential for a Gold particles with the radius of 1 nm, at $T = 2500\text{K}$. The insertions are the magnification of the key parts of these dependences, where the symbols represent the calculated data points. At smaller cutoff, we get higher chemical potential. This is because the important contribution of higher angular momentum states is ignored and the code has to increase the value of the chemical potential so that the calculated mean electron number matches the total number of conduction electrons involved in the system. As the cutoff increases the contribution of these higher angular momentum states has already been included, and thus the chemical potential decreases. Since the contribution of the very high angular momentum states is usually very small, there is no further decay on the value of the chemical potential. For $l_{\max} > 20$, the chemical potential tends to a stable value. Thus we set $l_{\max} = 20$ through out this work. The inserted figure shows us that the effect of the mesh interval is very weak on the values of the chemical potential, only about five out of a thousand.

In Fig.5.6 the temperature dependences of the chemical potential for a Gold sphere with different mesh intervals are plotted. It shows a slowly linear increase of the chemical potential with

temperature below 1300K. A nonlinear variation appears at higher temperatures. However, the over all variations are within 5%. Once again a very weak dependence on the mesh interval h is observed. To be more specific, we plot the distribution of the radial electron density in Fig.5.7 for three different temperatures, where $n_0(r)$ is the corresponding bulk conduction electron density. The variation of the electron density over a wide temperature is much small. This is reasonable because the characteristic energy for the conduction electrons in nanoparticles is usually much larger than the thermal energy associated with the temperature of several thousand Kelvins, for examples, the surface plasmon frequency is several electron volts and the typical gap between the single-electron energy levels is greater than 0.5eV. Therefore we will be very safe to set the work temperature for our finite temperature Green's function computations at $T = 2500K$. At this temperature, only 32 Matsubara imaginary frequencies are needed in our computation, which greatly reduces the computation time. The resulting frequency cutoff is about 40eV, much larger than the plasmon oscillation energy.

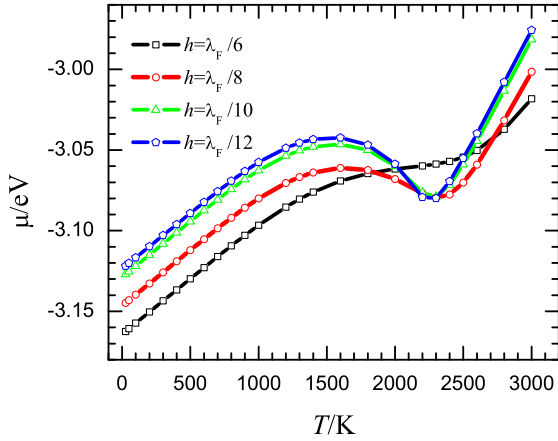


Figure 5.6: Temperature dependence of the chemical potential for a Gold sphere with the radius of 1nm

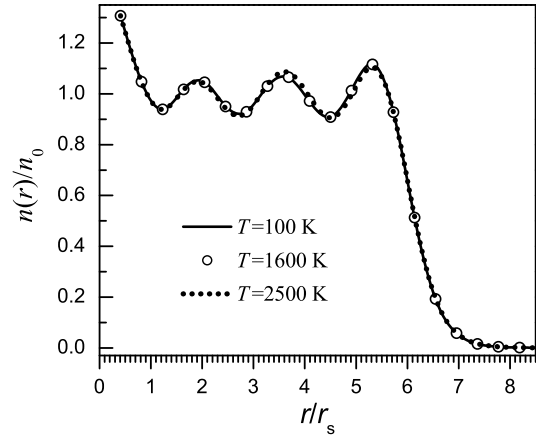


Figure 5.7: Distribution of the radial electron density for a Gold sphere with the radius of 1nm at different temperatures

5.3 RESULTS AND DISCUSSION

In this section, the results are given for the test cases of Gold and Sodium nanospheres with radius around 1nm. First we will show the result for the Hartree-Fock approximation. By this

approximation, one can get a rough insight into the electron dynamics of the system, especially the electron-hole pair excitation. The Green's function obtained in this approximation is to be used as the initial Green's function for the RPA computation.

5.3.1 HARTREE-FOCK APPROXIMATION

Fig.5.8 and 5.9 show the finite size effect of the electron leakage obtained in the Hartree-Fock approximation for Gold and Sodium nanospheres, respectively. The electron leakage is measured by the ratio of the mean number of spilling out electron to that of the total conduction electrons, *i.e.*, $\langle \Delta N \rangle / \langle N \rangle$. The mean number of spilling out electrons is calculated by integrating the radial density outside the jellium sphere, *i.e.*,

$$\langle \Delta N \rangle \equiv \int_R^\infty \langle n(r) \rangle r^2 dr \quad (5.21)$$

The numerical fitting on the data in the figures actually indicate a power law dependence of the

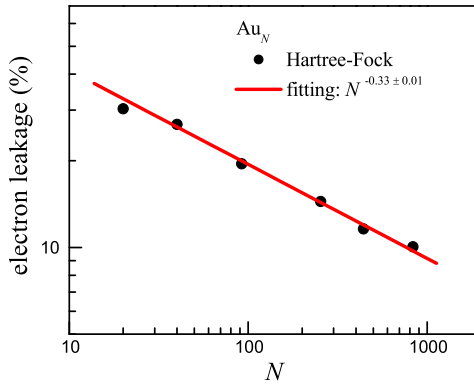


Figure 5.8: Electron leakage from Gold nanospheres in Hartree-Fock Approximation

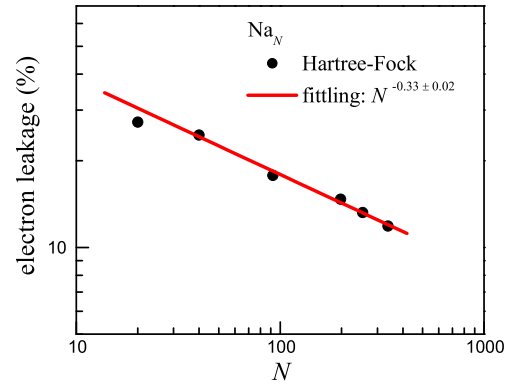


Figure 5.9: Electron leakage from Sodium spheres in Hartree-Fock Approximation

leakage on the number of atoms consisting of the nanospheres,

$$\langle \Delta N \rangle / \langle N \rangle \sim N^{1/3} \sim 1/R \quad (5.22)$$

This result explains why nanoscale particles have a higher static polarizability than their macroscopic counterpart.

According to classical electrodynamics a homogeneously charged conductor sphere of radius R has a static polarizability [20]

$$\alpha = R^3 \quad (5.23)$$

The spilling out effect results in the enlargement of the effective size of the charged sphere. If the characteristic range of the leakage is δ , then a estimation of the static polarizability is

$$\alpha = (R + \delta)^3 \quad (5.24)$$

which results in higher polarizability. The smaller the size of the jellium sphere the larger the leakage thickness δ , and consequently the bigger the polarizability.

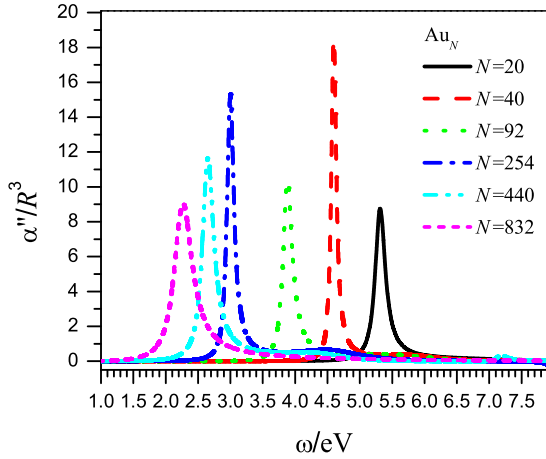


Figure 5.10: Imaginary part of the dynamical polarizability for Gold nanospheres in Hartree-Fock Approximation

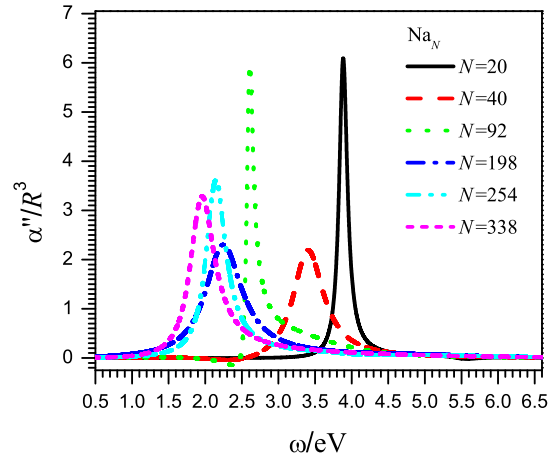


Figure 5.11: Imaginary part of the dynamical polarizability for Sodium nanospheres in Hartree-Fock Approximation

The imaginary parts of the dynamical electron polarizabilities for Gold and Sodium nanospheres are shown in Fig.5.10 and Fig.5.11, respectively. They show clearly the finite size effect of the peak frequencies – the blue shifts with the decreasing cluster size. These sharp peaks represent essentially the electron-hole excitation that excite electrons at the levels below the Fermi surface to the empty ones above the Fermi sea. The larger peak frequency for smaller sphere is due to the bigger gap between the levels [75]. These blue shifts can also be understood through the electron-hole excitation spectrum obtained in the free electron approximation [62,75]. The excitation occurs

within the region, in the (ω, q) plane, confined by the relation

$$\frac{q^2}{2m} - qv_F \leq \omega \leq \frac{q^2}{2m} + qv_F \quad (5.25)$$

where v_F is the Fermi speed, and q is the single-particle momentum. In infinite systems, the electron can have any momentum with values from 0 to ∞ . For finite size samples, however, the momentum is no longer conserved and there is a lower bound on the average momentum due to the constraint of the uncertainty principle. Electrons in an smaller sphere have a larger minimum momentum and thus the larger electron-hole excitation energy.

5.3.2 DRPA APPROXIMATION

Employing the Green's function obtained in the Hartree-Fock approximation as the initial Green's function, the Green's functions for nanospheres with different radii are calculated under the DRPA approximation. Fig. 5.12 and Fig. 5.13 are the size-dependence of the leakage for Gold and Sodium nanospheres. For the Gold nanospheres, the size effect obtained in DRPA approximation is not obviously different from that in the Hartree-Fock approximation, *i.e.*, both of them give the R^{-1} law. Comparing to results under the Hartree-Fock approximation, a bigger leakage is observed for the Sodium nsnosphere of 20 atoms, while the lower leakages are observed for the ones with the number of atoms larger that 20. It still follows a power law size-dependence but with the exponents greater than -1. At present, we have not understood this result. We will search for the answers in our future research.

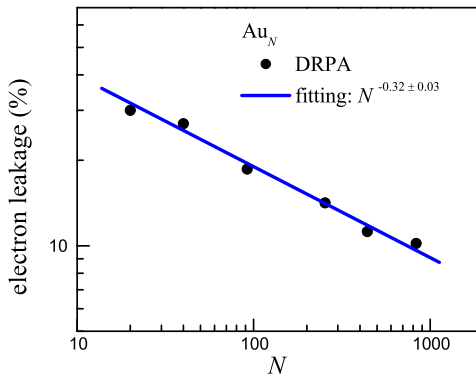


Figure 5.12: Electron leakage from Gold nanoparticles in DRPA Approximation

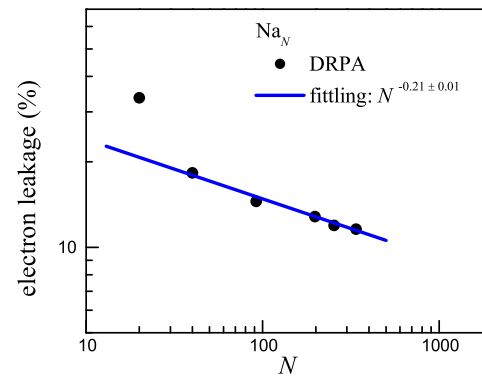


Figure 5.13: Electron leakage from Sodium nanoparticles in DRPA Approximation

CHAPTER 6

MESOSCOPIC ELECTRON AND PHONON TRANSPORT THROUGH A CURVED WIRE¹

¹Shi-Xian Qu and Michael R. Geller, *Phys. Rev. B* 70, 085414(2004).
Reprinted here with permission of publisher, 01/27/2005.

6.1 INTRODUCTION

A new class of nanomachines is attempting to measure extremely minute amounts of energy, of the order a few neV, and to use such calorimeters to probe fundamental properties of thermal conduction in the nanoscale regime. [76–80] Like the related case of electrical conduction, [81, 82] low-temperature thermal conduction in nanostructures is entirely different than in macroscopic materials because the phonons are in the mesoscopic regime, where they scatter elastically but not inelastically. Because inelastic scattering is required to establish thermodynamic equilibrium, there is a breakdown of Fourier’s law and the heat equation, which assume a local thermodynamic equilibrium characterized by a spatially varying temperature profile. These nanodevices have inspired considerable theoretical work on thermal transport by phonons in the mesoscopic limit. [83–97]

In this work we introduce a general method to calculate the scattering matrix for waves propagating through a curved wire or waveguide. The wire is assumed to be of uniform cross-section and lying in a plane, but the curved segment may have any smooth curvature profile, [98] such as that shown schematically in Fig. 6.1a. The ends of the wire (the “leads”) are also assumed to

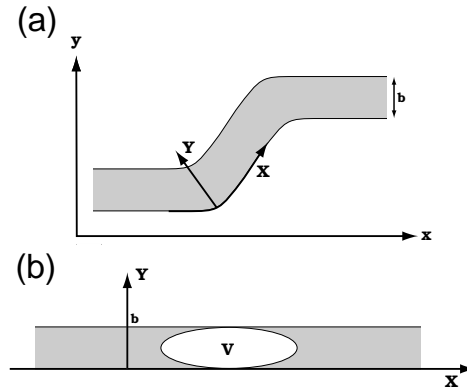


Figure 6.1: (a) An example of the type of two-dimensional curved wire geometry considered in this paper. The shape of the wire is used to define local orthogonal coordinates X and Y , with X the arclength along one of the edges. The width of the wire is b . (b) Scattering problem in the XY frame. Here the wire appears straight, but the curvature induces an effective potential V that causes scattering.

be straight. For definiteness we consider two-dimensional waves described by the scalar Helmholtz equation

$$[\nabla^2 + \alpha]\Phi(\mathbf{r}) = 0, \quad \mathbf{r} \equiv (x, y) \quad (6.1)$$

which is appropriate for electrons or scalar phonons in flat wires with rectangular cross-section. [99] Here $\alpha(\epsilon) \equiv 2m\epsilon/\hbar^2$ in the case of electrons of energy ϵ and mass m , whereas $\alpha(\epsilon) \equiv \epsilon^2/\hbar^2v^2$ in the case of scalar phonons of energy ϵ and bulk sound velocity v . Electron spin is of no importance here and is neglected. The boundary conditions at the edges of the wire are

$$\begin{aligned}\Phi(\mathbf{r}) &= 0, & (\text{for electrons}) \\ \mathbf{n} \cdot \nabla \Phi(\mathbf{r}) &= 0, & (\text{for phonons})\end{aligned}\tag{6.2}$$

where $\mathbf{n}(\mathbf{r})$ is a local outward-pointing normal. Here we have assumed conventional hard-wall boundary conditions for the electronic states, but stress-free conditions for the elastic waves because in this case the wires are usually freely suspended.

Although the wave equation in Eq. (6.1) is certainly simple, the scattering problem described here is complicated because the boundary conditions (6.2) are applied along the curves defining the two edges of the wire. Our approach involves rewriting Eqs. (6.1) and (6.2) in terms of new curvilinear coordinates X and Y , dictated by the shape of the wire, such that the wave equation becomes more complicated (the wire's curvature produces an effective potential), but the boundary conditions become trivial. We choose X to be the arclength along one edge of the wire, and Y is locally perpendicular. This transformation allows us to apply the standard techniques of scattering theory, including solution of the Lippmann-Schwinger equation, in the XY frame.

A particularly novel aspect of the phonon transport problem is that the reflection probability always vanishes in the long-wavelength limit, permitting an analytic (second-order Born approximation) treatment at low energies. The energy-dependent transmission probability is then expressed as a simple functional of the curvature profile $\kappa(X)$, making possible a straightforward analysis of a variety of wire shapes. The fact that long-wavelength phonons have perfect transmission is a consequence of the rigid-body nature of the underlying system: An elastic wave with infinite wavelength is just an adiabatic rigid translation of the wire, which must transmit energy perfectly.

There has been considerable attention given to mesoscopic electron transport through curved wires and waveguides, [100] but none to thermal transport. Electron transmission probabilities in curved wires are usually obtained by mode-matching, a method restricted to piecewise separable geometries (wires composed of straight segments, circles, and other shapes where the wave equation is separable). A related problem that has been studied extensively is the formation of electronic

bound states and resonances in curved wires, where the mapping to local curvilinear coordinates is also often used. [100–102] Surprisingly, we are not aware of any work using moving frames and then directly solving the resulting Lippmann-Schwinger equation in that basis. [103] Nor are we aware of the use of this method in the extensive microwave engineering literature, [104, 105] where the (more generally applicable but purely numerical) finite-element method is the technique of choice.

In the next section we carry out the above analysis for the two-dimensional Helmholtz equation. In Sec. 6.3 we consider electron transport through a circular right-angle bend, recovering results obtained by Sols and Macucci [106] and by Lin and Jaffe [107] using mode-matching methods. Our main results are given in Sec. 6.4, where we address thermal transport through curved wires. Sec. 6.5 contains a discussion of our conclusions and the experimental implications of this work.

6.2 APPLICATION TO SCALAR WAVE EQUATION

We now explain our method in detail and apply it to the scalar scattering problem stated in Eqs. (6.1) and (6.2).

6.2.1 CURVILINEAR COORDINATE SYSTEM

First we use the shape of the wire to define a curvilinear coordinate system, the arclength X along one edge and a locally perpendicular coordinate Y . Which edge one chooses is of course arbitrary. The direction of increasing Y will be chosen so that X, Y , and z form a right-handed coordinate system. Both edges are assumed to be a smooth plane curves. [98]

The unit tangent vector

$$\mathbf{e}_X \equiv \frac{d\mathbf{r}}{dX} = \frac{dx}{dX} \mathbf{e}_x + \frac{dy}{dX} \mathbf{e}_y \quad (6.3)$$

and normal

$$\mathbf{e}_Y \equiv -\frac{dy}{dX} \mathbf{e}_x + \frac{dx}{dX} \mathbf{e}_y \quad (6.4)$$

define local orthonormal basis vectors for the XY frame. The sign in Eq. (6.4) is chosen so that $\mathbf{e}_X \times \mathbf{e}_Y = \mathbf{e}_z$. We then use the Frenet-Serret equation

$$\frac{d\mathbf{e}_X}{dX} = \kappa(X) \mathbf{e}_Y \quad (6.5)$$

to define a signed curvature $\kappa(X)$ of the $Y=0$ edge. According to this definition, $\kappa(X)$ is positive when Y increases toward the center of curvature. We will also make use of the metric tensor

$$g = \begin{bmatrix} (1 - \kappa Y)^2 & 0 \\ 0 & 1 \end{bmatrix} \quad (6.6)$$

in the XY system.

6.2.2 HELMHOLTZ EQUATION IN CURVILINEAR COORDINATES

Next we make a coordinate transformation from \mathbf{r} to $\mathbf{R} \equiv (X, Y)$, and rewrite the wave equation in terms of these coordinates. A convenient way to do this is to use the identity

$$\nabla^2 = (\det g)^{-\frac{1}{2}} \frac{\partial}{\partial X_i} (\det g)^{\frac{1}{2}} g_{ij}^{-1} \frac{\partial}{\partial X_j}. \quad (6.7)$$

The Helmholtz equation (6.1) then becomes

$$[\partial_X^2 + \partial_Y^2 - V + \alpha] \Phi(\mathbf{R}) = 0, \quad (6.8)$$

where we have separated the combination $\partial_X^2 + \partial_Y^2$ from the many terms that appear on the right-hand-side of Eq. (6.7), and combined the remaining ones into an effective potential V . The potential V is itself a differential operator; an explicit expression will be given below. The boundary conditions (6.2) are now

$$\begin{aligned} \Phi(\mathbf{R}) &= 0, & (\text{for electrons}) \\ \partial_Y \Phi(\mathbf{R}) &= 0, & (\text{for phonons}) \end{aligned} \quad (6.9)$$

on the edges $Y=0$ and $Y=b$, with b the width of the wire. A scattering state $\Phi(\mathbf{R})$ becomes fully determined once we specify its behavior as $X \rightarrow \pm\infty$.

In the XY frame the wire appears straight, as illustrated in Fig. 6.1b. The scattering potential vanishes in the leads because the wire is straight there. We are now able to use conventional scattering theory.

6.2.3 UNPERTURBED SCATTERING STATES

The unperturbed ($V=0$) scattering states for both spinless electrons and scalar phonons are labeled by three quantum numbers σ , n , and ϵ , and can be written in the form

$$\phi_{\sigma n \epsilon}(\mathbf{R}) = c_{n \epsilon} e^{\sigma i k_{n \epsilon} X} \chi_n(\mathbf{Y}), \quad (6.10)$$

where

$$k_{n\epsilon} \equiv \sqrt{\alpha(\epsilon) - (n\pi/b)^2} \quad (6.11)$$

is the wave number along the wire,

$$\chi_n(Y) \equiv \begin{cases} \sqrt{2/b} \sin(n\pi Y/b) & \text{for electrons} \\ \sqrt{(2-\delta_{n0})/b} \cos(n\pi Y/b) & \text{for phonons} \end{cases} \quad (6.12)$$

is a trigonometric function satisfying the transverse boundary conditions of Eq. (6.9), and

$$c_{n\epsilon} \equiv \frac{1}{\sqrt{2\pi}} \left| \frac{\partial k_{n\epsilon}}{\partial \epsilon} \right|^{1/2} \quad (6.13)$$

is a real normalization constant. σ is a chirality index, defined by

$$\sigma = \begin{cases} +1 & \text{if moving in } +X \text{ direction} \\ -1 & \text{if moving in } -X \text{ direction} \end{cases} \quad (6.14)$$

and n is an integer-valued branch index. The transverse eigenfunctions $\chi_n(Y)$ are normalized according to

$$\int_0^b dY \chi_n(Y) \chi_{n'}(Y) = \delta_{nn'}. \quad (6.15)$$

The dispersion relation given by Eq. (6.11) is shown in Fig. 6.2.

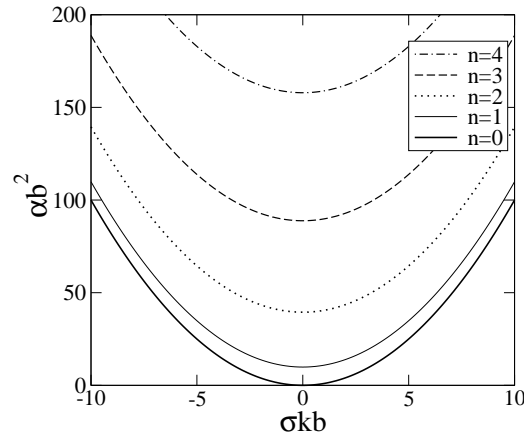


Figure 6.2: Dispersion relation for unperturbed scattering states, for both spinless electrons and scalar phonons. α is equal to $2m\epsilon/\hbar^2$ in the case of electrons, or $\epsilon^2/\hbar^2 v^2$ in the case of phonons. σ is 1 on the right half of the figure, and -1 on the left. b is the wire width.

The allowed values of the quantum numbers σ , n , and ϵ are as follows: The allowed energies form a continuum, from ϵ_{\min} to ∞ . Here

$$\epsilon_{\min} \equiv \begin{cases} \frac{\hbar^2 \pi^2}{2mb^2} & \text{for electrons} \\ 0 & \text{for phonons} \end{cases}. \quad (6.16)$$

For each value of energy, the branch index takes the values in a set S of integers defined by

$$S \equiv \begin{cases} 1, 2, \dots, N & \text{for electrons} \\ 0, 1, 2, \dots, N & \text{for phonons} \end{cases} \quad (6.17)$$

where

$$N(\epsilon) \equiv \sum_{n=0}^{\infty} \Theta\left[\alpha(\epsilon) - \frac{n^2 \pi^2}{b^2}\right] - 1, \quad (6.18)$$

with $\Theta(x)$ the unit step function. For electrons, N is the number of propagating channels below energy ϵ , whereas for phonons the number of propagating channels is $N+1$. Finally, for each allowed value of ϵ and n , σ takes on the values ± 1 .

The free scattering states satisfy the orthonormality and completeness conditions

$$\int d^2 R \phi_{\sigma n \epsilon}^*(\mathbf{R}) \phi_{\sigma' n' \epsilon'}(\mathbf{R}) = \delta_{\sigma \sigma'} \delta_{nn'} \delta(\epsilon - \epsilon') \quad (6.19)$$

and

$$\int_{\epsilon_{\min}}^{\infty} d\epsilon \sum_{\sigma=\pm 1} \sum_{n \in S} \phi_{\sigma n \epsilon}^*(\mathbf{R}) \phi_{\sigma n \epsilon}(\mathbf{R}') = \delta(\mathbf{R} - \mathbf{R}'), \quad (6.20)$$

where n takes the values given in Eq. (6.17).

6.2.4 EFFECTIVE POTENTIAL

The terms $\partial_X^2 + \partial_Y^2$ have been separated out from the right-hand-side of Eq. (6.7) so that the eigenfunctions $\Phi(\mathbf{R})$ reduce to that of a straight wire when $V = 0$. Accordingly, the effective potential is given by

$$V = \frac{\kappa^2 Y^2 - 2\kappa Y}{(1 - \kappa Y)^2} \partial_X^2 - \frac{\kappa' Y}{(1 - \kappa Y)^3} \partial_X + \frac{\kappa}{1 - \kappa Y} \partial_Y. \quad (6.21)$$

There will be no singularities in V as long as

$$-\infty < \kappa b < 1. \quad (6.22)$$

The condition (6.22) guarantees that both the $Y=0$ and $Y=b$ edges of the wire are smooth.

In applications where the radius of curvature $|\kappa|^{-1}$ is much larger than b , Eq. (6.21) can be simplified. To leading order in κb the effective potential reduces to

$$V = -2\kappa Y \partial_X^2 - \kappa' Y (1 + 3\kappa Y) \partial_X + \kappa \partial_Y. \quad (6.23)$$

6.2.5 LIPPMANN-SCHWINGER EQUATION

The scattering problem in the XY frame can be solved by standard methods. The Lippmann-Schwinger equation for an eigenfunction $\Phi(\mathbf{R})$ with (electron or phonon) energy ϵ is

$$\Phi(\mathbf{R}) = \phi_{\text{in}}(\mathbf{R}) + \int d^2 R' G_0(\mathbf{R}, \mathbf{R}', \epsilon) V \Phi(\mathbf{R}'), \quad (6.24)$$

where $\phi_{\text{in}}(\mathbf{R})$ is a free scattering state coming in from the left, and where $G_0(\mathbf{R}, \mathbf{R}', \epsilon)$ is the Green's function for the unperturbed Helmholtz equation, satisfying

$$[\partial_X^2 + \partial_Y^2 + \alpha(\epsilon)] G_0(\mathbf{R}, \mathbf{R}', \epsilon) = \delta(\mathbf{R} - \mathbf{R}'), \quad (6.25)$$

along with the boundary condition that $G_0(\mathbf{R}, \mathbf{R}', \epsilon)$ vanishes as $|X - X'| \rightarrow \infty$. The Lippmann-Schwinger equation gives the solution of Eq. (6.8) subject to the condition that $\Phi(\mathbf{R})$ reduces to the incident state $\phi_{\text{in}}(\mathbf{R})$ when $X \rightarrow -\infty$.

The unperturbed Green's function for both electrons and phonons is

$$G_0(\mathbf{R}, \mathbf{R}', \epsilon) = -\frac{i}{2} \sum_{n=0}^{\infty} \frac{\chi_n(Y) \chi_n(Y')}{k_{n\epsilon}} e^{ik_{n\epsilon}|X-X'|}. \quad (6.26)$$

We note that the summation in Eq. (6.26) is *not* restricted to the values given in Eq. (6.17). In particular, off-shell values of $k_{n\epsilon}$ are included. Furthermore, in the electron case the $n=0$ term in the summation vanishes, because the transverse eigenfunction $\chi_0(Y)$ vanishes.

We will also need to write Eq. (6.24) in the alternative form

$$\Phi(\mathbf{R}) = \phi_{\text{in}}(\mathbf{R}) + \int d^2 R' G(\mathbf{R}, \mathbf{R}', \epsilon) V \phi_{\text{in}}(\mathbf{R}'), \quad (6.27)$$

where $G(\mathbf{R}, \mathbf{R}', \epsilon)$ is the Green's function of the *perturbed* Helmholtz equation, satisfying

$$\begin{aligned} G(\mathbf{R}, \mathbf{R}', \epsilon) &= G_0(\mathbf{R}, \mathbf{R}', \epsilon) \\ &+ \int d^2 R'' G_0(\mathbf{R}, \mathbf{R}'', \epsilon) V G(\mathbf{R}'', \mathbf{R}', \epsilon). \end{aligned} \quad (6.28)$$

6.2.6 TRANSMISSION PROBABILITY

The transmission coefficient matrix $t_{nn'}(\epsilon)$ gives the probability amplitude for a right-moving electron or phonon to forward scatter from branch n to branch n' at energy ϵ . We define $t_{nn'}(\epsilon)$ to be zero if one or both branches have minima above ϵ .

We can obtain a formal expression for $t_{nn'}(\epsilon)$ by writing the $X \rightarrow \infty$ limit of the unperturbed Green's function as

$$G_0(\mathbf{R}, \mathbf{R}', \epsilon) \rightarrow -\frac{i}{2} \sum_{n \in S} \frac{\phi_{Rn\epsilon}(\mathbf{R}) \phi_{Rn\epsilon}^*(\mathbf{R}')}{k_{n\epsilon} c_{n\epsilon}^2}, \quad (6.29)$$

where the subscripts R denote right-moving ($\sigma = +1$) waves. The summation in Eq. (6.29) is now restricted to $n \leq N$ because the higher lying contributions are exponentially small in the $X \rightarrow \infty$ limit. Then from Eqs. (6.24) and (6.29) we obtain

$$\lim_{X \rightarrow \infty} \Phi(\mathbf{R}) = \phi_{Rn_i\epsilon}(\mathbf{R}) - \frac{i}{2} \sum_{n \in S} \frac{\langle \phi_{Rn\epsilon} | V | \Phi \rangle}{k_{n\epsilon} c_{n\epsilon}^2} \phi_{Rn\epsilon}(\mathbf{R}) \quad (6.30)$$

where the incoming right-moving wave is assumed to be in channel n_i . Therefore we conclude that

$$\lim_{X \rightarrow -\infty} \Phi = \phi_{Rn_i\epsilon} \quad (6.31)$$

and

$$\lim_{X \rightarrow \infty} \Phi = \sum_{n \in S} t_{n_i n}(\epsilon) \phi_{Rn\epsilon}, \quad (6.32)$$

where

$$t_{nn'}(\epsilon) \equiv \delta_{nn'} - \frac{i}{2} \frac{\langle \phi_{Rn'\epsilon} | V | \Phi \rangle}{k_{n'\epsilon} c_{n'\epsilon}^2} \quad (6.33)$$

is the amplitude for an incident wave (R, n, ϵ) to forward-scatter to (R, n', ϵ) . $t_{nn'}(\epsilon)$ is called the transmission matrix.

We emphasize that for the case of electron transport, $t(\epsilon)$ is an $N \times N$ matrix, where N varies with energy as indicated in Eq. (6.18). For phonons, $t(\epsilon)$ is $N+1$ -dimensional.

The expectation value in Eq. (6.33) involves the exact scattering state Φ with boundary condition corresponding to an incident state (R, n, ω) . Using Eq. (6.27) we write this as

$$\begin{aligned} \langle \phi_{Rn'\epsilon} | V | \Phi \rangle &= \langle \phi_{Rn'\epsilon} | V | \phi_{Rn\epsilon} \rangle \\ + \int \phi_{Rn'\epsilon}^*(\mathbf{R}) V_R G(\mathbf{R}, \mathbf{R}', \epsilon) V_{R'} \phi_{Rn\epsilon}(\mathbf{R}'), \end{aligned} \quad (6.34)$$

where V_R and $V_{R'}$ act on \mathbf{R} and \mathbf{R}' , respectively. The numerical method we use consists of expressing Eq. (6.28) in a basis of unperturbed scattering states, solving this equation by matrix inversion, and using Eq. (6.34) to obtain the transmission matrix in Eq. (6.33).

Finally, we define the energy-dependent transmission probabilities T_{el} and T_{ph} for electrons and phonons that determine the electrical and thermal currents. For electrons, the relevant quantity is the ratio of transmitted to incident charge current, given by

$$T_{\text{el}}(\epsilon) = \sum_{n,n'=1}^N |t_{nn'}|^2 = \text{Tr } t^\dagger t. \quad (6.35)$$

For thermal transport by phonons, the relevant quantity is the fraction of transmitted energy current, [86] given by

$$T_{\text{ph}}(\epsilon) = \sum_{n,n'=0}^N \frac{v_{n'}}{v_n} |t_{nn'}|^2, \quad (6.36)$$

where $v_n(\epsilon)$ is the phonon *group* velocity in the straight wire, which can be written as $\hbar v^2 k_{n\epsilon}/\epsilon$. Because the bulk sound velocity v is a constant here, and the scattering is elastic, we can equivalently write Eq. (6.36) as

$$T_{\text{ph}}(\epsilon) = \sum_{n,n'=0}^N \frac{k_{n'\epsilon}}{k_{n\epsilon}} |t_{nn'}|^2, \quad (6.37)$$

with the $k_{n\epsilon}$ given by Eq. (6.11).

6.2.7 LANDAUER FORMULA

The charge current I and linear conductance

$$G \equiv \lim_{V \rightarrow 0} \frac{I}{V} \quad (6.38)$$

are related to the electron transmission probability $T_{\text{el}}(\epsilon)$ through the Landauer formula [81, 82]

$$I = \frac{e}{2\pi\hbar} \int_0^\infty d\epsilon T_{\text{el}}(\epsilon) [n_{\text{F}}^{\mu_l}(\epsilon) - n_{\text{F}}^{\mu_r}(\epsilon)]. \quad (6.39)$$

Here $n_{\text{F}}^{\mu_l}(\epsilon)$ and $n_{\text{F}}^{\mu_r}(\epsilon)$ are the Fermi distribution functions in the left (l) and right (r) leads, with chemical potentials μ_l and μ_r differing in proportion to the applied voltage $V = (\mu_l - \mu_r)/e$.

Similarly, the thermal current I_{th} and conductance

$$G_{\text{th}} \equiv \lim_{\Delta T \rightarrow 0} \frac{I_{\text{th}}}{\Delta T} \quad (6.40)$$

are determined by the phonon transmission probability $T_{\text{ph}}(\epsilon)$ according to [84–86]

$$I_{\text{th}} = \frac{1}{2\pi\hbar} \int_0^\infty d\epsilon \epsilon T_{\text{ph}}(\epsilon) [n_{\text{B}}^{T_l}(\epsilon) - n_{\text{B}}^{T_r}(\epsilon)]. \quad (6.41)$$

$n_{\text{B}}^{T_l}(\epsilon)$ and $n_{\text{B}}^{T_r}(\epsilon)$ are Bose distribution functions in the left and right leads, with temperatures T_l and T_r .

6.3 ELECTRON TRANSPORT

We turn now to an application of our method to coherent electron transport through a circular right-angle bend with outer radius R and width b . In this case the curvature profile is

$$\kappa(X) = \frac{1}{R} \Theta(X) \Theta(\frac{\pi R}{2} - X), \quad (6.42)$$

where Θ is the unit step function. The origin of the X coordinate is taken to be one of the locations where the straight and curved sections of the wire meet.

As explained above, the numerical method we use to calculate $t_{nn'}(\epsilon)$ requires the matrix elements $\langle \phi_{\sigma n \epsilon} | V | \phi_{\sigma' n' \epsilon'} \rangle$ of the effective potential (6.21) in the unperturbed scattering states (6.10). However, matrix elements of the second term in Eq. (6.21), which contain the curvature gradient

$$\kappa'(X) = \frac{1}{R} [\delta(X) - \delta(X - \frac{\pi R}{2})], \quad (6.43)$$

involves integrals of a delta function δ times functions $F(\Theta)$ of Θ . Integrals of this form, involving products of generalized functions, have to be evaluated carefully, as we show in Appendix C. Apart from this technicality, the application of our method to this geometry is straightforward.

Mesoscopic charge transport through bent wires has already been studied extensively, [100] and we will only consider one case of this, namely $R = 1.2b$. First we calculate the individual electron transmission probabilities $|t_{nn'}(\epsilon)|^2$ from Eq. (6.33) for the lowest few channels n and n' . The results are given in Fig. 6.4 and are in excellent agreement with the mode-matching results of Sols and Macucci [106] for the same value of R/b (see Fig. 2a of Ref. [106]). Our result for $|t_{11}(\epsilon)|^2$ also agrees

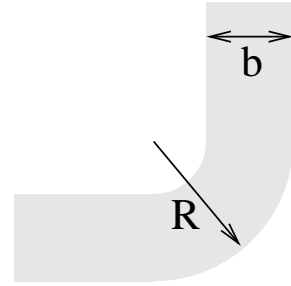


Figure 6.3: Section of quantum wire with circular right-angle bend.

qualitatively with that calculated by Lin and Jaffe [107] for a right-angle bend with a slightly larger curvature (see Fig. 8 of Ref. [107]).

The total electron transmission probability $\mathcal{T}_{\text{el}}(\epsilon)$, defined in Eq. (6.35), is presented in Fig. 6.5 for the same curved wire. At energies given by

$$\epsilon = n^2 \Delta_{\text{el}} \quad \text{with} \quad n = 1, 2, 3, \dots, \quad (6.44)$$

where $\Delta_{\text{el}} \equiv \pi^2 \hbar^2 / 2mb^2$, additional channels in the wire become propagating and contribute to the transmission probability. The threshold energies (6.44) follows from Eq. (6.11) and Fig. 6.2. The principal effect of the curvature in the wire is to soften the transitions at these thresholds.

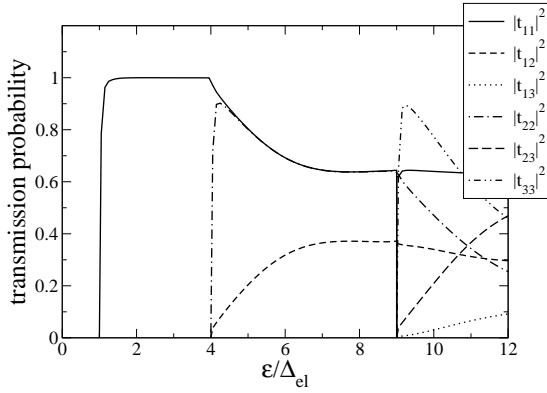


Figure 6.4: Individual electron transmission probabilities $|t_{nn'}|^2$ as a function of energy for a circular right-angle bend with $R/b = 1.20$. Here $\Delta_{\text{el}} \equiv \pi^2 \hbar^2 / 2mb^2$.

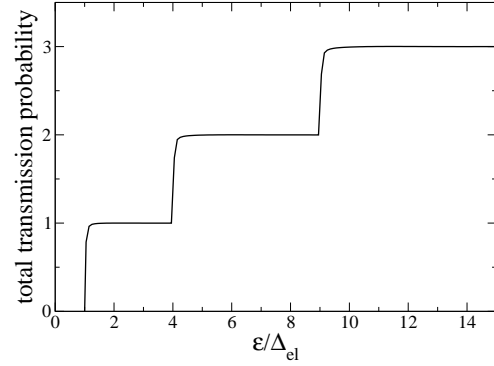


Figure 6.5: Total electron transmission probability \mathcal{T}_{el} . System parameters are the same as in Fig. 6.4.

6.4 PHONON TRANSPORT

We turn now to the main emphasis of our work, the calculation of transmission probabilities for two-dimensional scalar phonons with energy $\epsilon = \hbar\omega$ and (bulk) sound velocity v to propagate through curved wires. We are not aware of any previous work on this problem.

As before, we consider a circular right-angle bend with outer radius R and width b , with curvature profile given by Eq. (6.42). The method of solution is the same as that outlined in Sec. 6.3 and Appendix C, except that the transverse parts of the unperturbed scattering states, defined in Eq. (6.12), are now different. In Fig. 6.6 we give the individual phonon transmission

probabilities $|t_{nn'}(\epsilon)|^2$, defined in Eq. (6.33), for the lowest channels in a smoothly bent wire with $R = 2b$. In Fig. 6.7 we do the same for a more tightly bent wire, with $R = 1.001b$ (inner radius is $10^{-3}b$). At energies given by

$$\epsilon = n\Delta_{\text{el}} \quad \text{with} \quad n = 1, 2, 3, \dots, \quad (6.45)$$

where $\Delta_{\text{ph}} \equiv \pi\hbar v/b$, additional channels in the wire become propagating and contribute to thermal transport. In both examples, transmission is nearly perfect in the low-energy $\epsilon < \Delta_{\text{ph}}$ limit, where there is only a single propagating channel. At higher energies, scattering does occur. However it is mostly in the forward direction, and the fraction of transmitted energy $T_{\text{ph}}(\epsilon)$, defined in Eq. (6.36), is essentially unchanged from that of a straight wire.

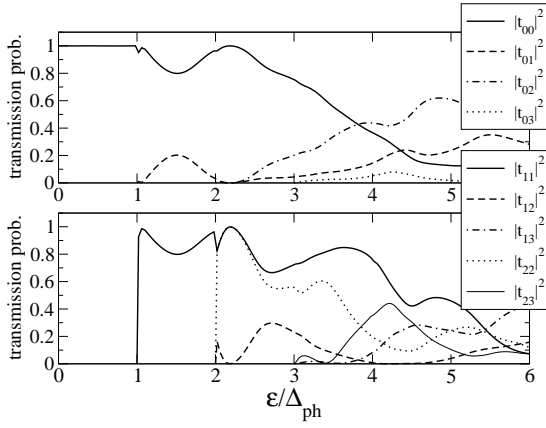


Figure 6.6: Individual phonon transmission probabilities $|t_{nn'}|^2$ as a function of energy for a circular right-angle bend with $R = 2b$. Here $\Delta_{\text{ph}} \equiv \pi\hbar v/b$.

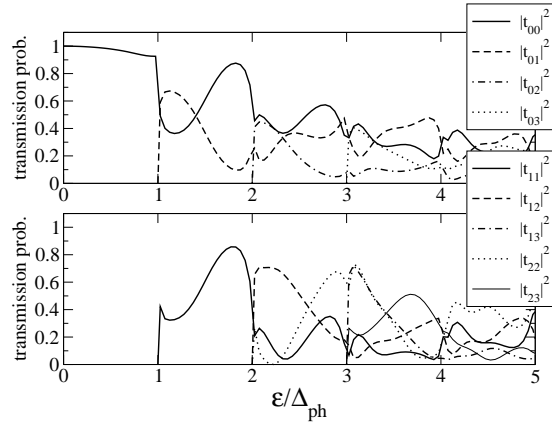


Figure 6.7: Individual phonon transmission probabilities $|t_{nn'}|^2$ as a function of energy for a circular right-angle bend with $R = 1.001b$.

In Fig. 6.8 we plot the thermal conductance G_{th} in units of the “quantum” of thermal conductance

$$G_{\text{q}} \equiv \frac{\pi k_{\text{B}}^2 T}{6\hbar} \approx 0.95 T \text{ pW K}^{-2}, \quad (6.46)$$

for a curved wire of width $b = 100 \text{ nm}$ and outer radius $R = 1.001b$. The scalar phonon velocity is taken to be $v = 8.5 \times 10^5 \text{ cm s}^{-1}$, the longitudinal sound speed in Si. The thermal transport is hardly affected by the curvature in the wire, as can be seen in Fig. 6.9, which compares an expanded plot of $G_{\text{th}}/G_{\text{q}}$ to that for a straight wire. The greatest suppression occurs near 200 mK and is only about 0.5% of the thermal conductance quantum.

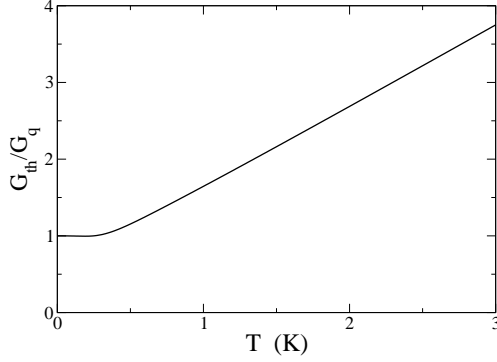


Figure 6.8: Dimensionless thermal conductance $G_{\text{th}}/G_{\text{q}}$ as a function of temperature, for a 100 nm curved Si-like quantum wire, with outer radius $R = 1.001 b$. Here $G_{\text{q}} \equiv \pi k_{\text{B}}^2 T / 6\hbar$, which is itself linearly proportional to temperature.

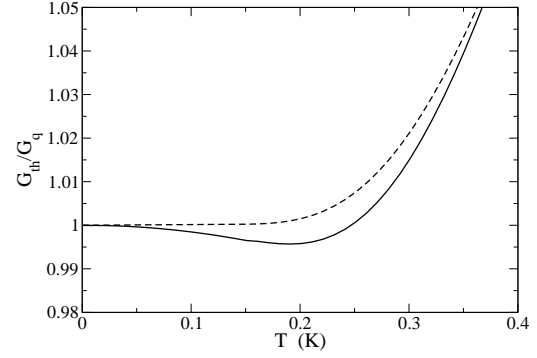


Figure 6.9: The solid curve is the same as Fig. 6.8. Dashed curve is the dimensionless thermal conductance for a straight Si-like wire with $b = 100$ nm. Thermal transport is hardly suppressed by the bending.

It is physically unrealistic to consider a 100 nm wire bent more sharply than $R = 1.001 b$, because the inner radius of 0.10 nm in this case is already approaching atomic dimensions. However, for a wire of width $b = 10 \mu\text{m}$ and the same inner radius of curvature, we have $R = 1.00001 b$, the transmission probabilities for which are shown in Fig. 6.10. The transmission probabilities when $R = 1.00001 b$ are similar to that for $R = 1.001 b$, shown previously in Fig. 6.7, as

is the thermal conductance. We find in that in a $10 \mu\text{m}$ Si-like quantum wire with $R = 1.00001 b$, the greatest suppression in G_{th} occurs near 2 mK and is again only about 0.5% of the conductance quantum in magnitude.

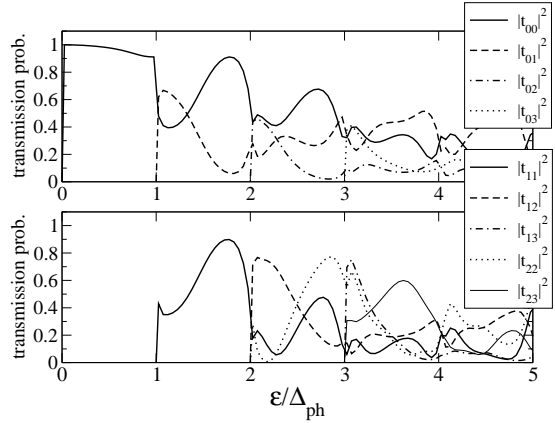


Figure 6.10: Individual phonon transmission probabilities $|t_{nn'}|^2$ as a function of energy for a circular right-angle bend with $R = 1.00001 b$.

6.5 DISCUSSION

We have introduced a general method to calculate the transmission of scalar waves appropriate for mesoscopic electron and phonon transport through a curved wire or waveguide. Applications to electron transport accurately reproduce results obtained by other methods. Phonon transport through curved wires is considered here for the first time.

Our results demonstrate that curvature hardly suppresses thermal transport, even for sharply bent wires, at least within the two-dimensional scalar phonon model considered. This behavior can, to some extent, be understood by considering transport in the extreme long- and short-wavelength limits. In the long-wavelength, low energy limit, $T_{\text{ph}} \rightarrow 1$, a consequence of the rigid-body nature of the wire. T_{ph} also approaches unity for short wavelengths, because in this limit the phonons cannot sense the curvature.

Because the phonon reflection probability always vanishes in the long-wavelength limit, a simple perturbative (Born approximation) treatment is possible at low energies. For example, the energy-dependent $n = 0$ transmission probability is

$$|t_{00}|^2 = 1 - |r_{00}|^2, \quad (6.47)$$

where, to leading nontrivial order,

$$\begin{aligned} r_{00} &= -\frac{i\hbar v}{2\epsilon b} \int d^2 R d^2 R' e^{i\epsilon X/\hbar v} \\ &\times V_R G_0(\mathbf{R}, \mathbf{R}', \epsilon) V_{R'} e^{i\epsilon X'/\hbar v}. \end{aligned} \quad (6.48)$$

V_R and $V_{R'}$ act on \mathbf{R} and \mathbf{R}' , respectively. This result allows the low-temperature thermal transport through a variety of wire shapes to be addressed quite simply. Although an analogous perturbative expression can be derived for the electronic transmission probability as well, the form of the transverse part χ_n of the unperturbed scattering states, as dictated by the hard-wall boundary conditions, then leads to a divergence in the Born series, [108] consistent with the fact that $T_{\text{el}} \rightarrow 0$ in the long-wavelength limit.

We conclude with a brief discussion of the experimental implications of our mesoscopic thermal transport results, the charge-transport case having already been discussed in the literature. [100,109] Thermal transport in carbon nanotubes has been studied experimentally by several groups, [110–

112] and nanotubes would be interesting systems to use to investigate the effects of bending on transport. To apply our method of analysis to this system would require the consideration of scattering of elastic waves in a curved, hollow tube. Although they were obtained for scalar phonons in two-dimensional strips, our results do suggest that the effects of curvature will be small, if not completely negligible, in these systems.

CHAPTER 7

HOT ELECTRONS IN LOW-DIMENSIONAL PHONON SYSTEMS¹

¹Shi-Xian Qu, Michael R. Geller and A. N. Cleland. Submitted to *Phys. Rev. Lett*, 03/15/2005.

The coupling between electrons and phonons plays a crucial role in determining the thermal properties of nanostructures. The widely used “standard” model of low temperature electron-phonon thermal coupling and hot-electron effects in bulk metals [113, 114] assumes (i) a clean three-dimensional free-electron gas with a spherical Fermi surface, rapidly equilibrated to a temperature T_{el} ; (ii) a continuum description of the acoustic phonons, which have a temperature T_{ph} ; (iii) a negligible Kapitza-like thermal boundary resistance [115] between the metal and any surrounding dielectric, an assumption that is well justified experimentally; and (iv), a deformation-potential electron-phonon coupling, expected to be the dominant interaction at long-wavelengths. In a bulk metal, the net rate P of thermal energy transfer between the electron and phonon subsystems is [114]

$$P = \Sigma V_{\text{el}} (T_{\text{el}}^5 - T_{\text{ph}}^5), \quad (7.1)$$

where V_{el} is the volume of the metal, and

$$\Sigma \equiv \frac{8 \zeta(5) k_{\text{B}}^5 \epsilon_{\text{F}}^2 N_{\text{el}}(\epsilon_{\text{F}})}{3\pi \hbar^4 \rho v_{\text{F}} v_{\text{l}}^4}. \quad (7.2)$$

Here ζ is the Riemann zeta function, ϵ_{F} is the Fermi energy, N_{el} is the electronic density of states (DOS) per unit volume, ρ is the mass density, v_{l} is the bulk longitudinal sound speed, and v_{F} is the Fermi velocity.

This model, which has no adjustable parameters, has successfully explained some experiments [114, 116, 117], but others report a power-law temperature dependence with smaller exponents [118, 119], indicating an enhanced electron-phonon coupling at low temperatures. However, the experiments typically involve heating measurements in thin metal films deposited on semiconducting substrates, and the relevant phonons at low temperature are strongly modified by the exposed stress-free surface. An attempt to directly probe such phonon-dimensionality effects was carried out by DiTusa *et al.* [119], who intentionally suspended some of their samples, necessarily modifying the vibrational spectrum, although they found no significant difference from their supported films. We argue that the paradox reported in Ref. [119] is actually quite widespread, and all experiments known to us on supported films actually contradict the standard model when that model is modified to account for the actual vibrational modes present in a realistic supported-film

geometry, illustrated in Fig. 7.1. Our results have important implications for the thermal properties of mesoscopic and low-dimensional phonon systems and the use of such systems as nanoscale thermometers, bolometers, and calorimeters [120–122].

The Hamiltonian we consider (suppressing spin) is $H = \sum_{\mathbf{k}} \epsilon_{\mathbf{k}} c_{\mathbf{k}}^{\dagger} c_{\mathbf{k}} + \sum_n \hbar \omega_n a_n^{\dagger} a_n + \delta H$, where $c_{\mathbf{k}}^{\dagger}$ and $c_{\mathbf{k}}$ are electron creation and annihilation operators, with \mathbf{k} the momentum, and a_n^{\dagger} and a_n are bosonic phonon creation and annihilation operators. The vibrational modes, labeled by an index n , are eigenfunctions of the continuum elasticity equation $v_t^2 \nabla \times \nabla \times \mathbf{u} - v_l^2 \nabla (\nabla \cdot \mathbf{u}) = \omega^2 \mathbf{u}$ for linear isotropic media, along with accompanying boundary conditions. v_t and v_l are the bulk transverse and longitudinal sound velocities. $\delta H \equiv \frac{2}{3} \epsilon_F \int_{V_{\text{el}}} d^3 r \psi^{\dagger} \psi \nabla \cdot \mathbf{u}$ is the deformation-potential electron-phonon interaction, with $\mathbf{u}(\mathbf{r}) = \sum_n (2\rho\omega_n)^{-\frac{1}{2}} [\mathbf{f}_n(\mathbf{r}) a_n + \mathbf{f}_n^*(\mathbf{r}) a_n^{\dagger}]$ the quantized displacement field. The vibrational eigenfunctions $\mathbf{f}_n(\mathbf{r})$ are defined to be solutions of the elasticity field equations, normalized over the phonon volume V_{ph} according to $\int_{V_{\text{ph}}} d^3 r \mathbf{f}_n^* \cdot \mathbf{f}_{n'} = \delta_{nn'}$. It will be convenient to rewrite the electron-phonon interaction as $\delta H = \sum_{\mathbf{k}\mathbf{q}n} [g_{n\mathbf{q}} c_{\mathbf{k}+\mathbf{q}}^{\dagger} c_{\mathbf{k}} a_n + g_{n\mathbf{q}}^* c_{\mathbf{k}-\mathbf{q}}^{\dagger} c_{\mathbf{k}} a_n^{\dagger}]$, with coupling constant $g_{n\mathbf{q}} \equiv \frac{2}{3} \epsilon_F (2\rho\omega_n)^{-\frac{1}{2}} V_{\text{el}}^{-1} \int_{V_{\text{el}}} d^3 r \nabla \cdot \mathbf{f}_n e^{-i\mathbf{q}\cdot\mathbf{r}}$. Note that we allow for different electron and phonon volumes.

The quantity we calculate is the thermal energy per unit time transferred from the electrons to the phonons,

$$P \equiv 2 \sum_{\mathbf{k}\mathbf{q}n} \hbar \omega_n [\Gamma_n^{\text{em}}(\mathbf{k} \rightarrow \mathbf{k} - \mathbf{q}) - \Gamma_n^{\text{ab}}(\mathbf{k} \rightarrow \mathbf{k} + \mathbf{q})], \quad (7.3)$$

where

$$\begin{aligned} \Gamma_n^{\text{em}}(\mathbf{k} \rightarrow \mathbf{k} - \mathbf{q}) &= 2\pi |g_{n\mathbf{q}}|^2 [n_{\text{B}}(\omega_n) + 1] \\ &\times n_{\text{F}}(\epsilon_{\mathbf{k}}) [1 - n_{\text{F}}(\epsilon_{\mathbf{k}-\mathbf{q}})] \delta(\epsilon_{\mathbf{k}-\mathbf{q}} - \epsilon_{\mathbf{k}} + \omega_n) \end{aligned} \quad (7.4)$$

is the golden-rule rate for an electron of momentum \mathbf{k} to scatter to $\mathbf{k} - \mathbf{q}$ while emitting a phonon n , and

$$\begin{aligned} \Gamma_n^{\text{ab}}(\mathbf{k} \rightarrow \mathbf{k} + \mathbf{q}) &= 2\pi |g_{n\mathbf{q}}|^2 n_{\text{B}}(\omega_n) \\ &\times n_{\text{F}}(\epsilon_{\mathbf{k}}) [1 - n_{\text{F}}(\epsilon_{\mathbf{k}+\mathbf{q}})] \delta(\epsilon_{\mathbf{k}+\mathbf{q}} - \epsilon_{\mathbf{k}} - \omega_n) \end{aligned} \quad (7.5)$$

is the corresponding phonon absorption rate. n_{B} is the Bose distribution function with temperature T_{ph} and n_{F} is the Fermi distribution with temperature T_{el} . The factor of 2 in (7.3) accounts for

spin degeneracy. It is possible to obtain an exact expression for P ; the result (suppressing factors of \hbar and k_B) is

$$P = \frac{m^2 V_{\text{el}}^2}{8\pi^4} \sum_n \int_0^\infty d\omega \delta(\omega - \omega_n) \left(\frac{\omega}{e^{\omega/T_{\text{el}}} - 1} - \frac{\omega}{e^{\omega/T_{\text{ph}}} - 1} \right) \\ \times \int d^3k \frac{|g_{n\mathbf{k}}|^2}{|\mathbf{k}|} \left[\omega + T_{\text{el}} \ln \left(\frac{1 + \exp[(\frac{m\omega^2}{2k^2} + \frac{k^2}{8m} - \frac{\omega}{2} - \mu)/T_{\text{el}}]}{1 + \exp[(\frac{m\omega^2}{2k^2} + \frac{k^2}{8m} + \frac{\omega}{2} - \mu)/T_{\text{el}}]} \right) \right].$$

The logarithmic term in P can be shown to be negligible in the temperature regime of interest and will be dropped. Carrying out the \mathbf{k} integration then leads to

$$P = \frac{v_1^4 \Sigma V_{\text{el}}}{24 \zeta(5)} \int_0^{\omega_D} d\omega F(\omega) \left(\frac{\omega}{e^{\omega/T_{\text{el}}} - 1} - \frac{\omega}{e^{\omega/T_{\text{ph}}} - 1} \right), \quad (7.6)$$

where $F(\omega) \equiv \sum_n U_n \delta(\omega - \omega_n)$ is a strain-weighted vibrational DOS, with

$$U_n \equiv \frac{1}{V_{\text{el}}} \int_{V_{\text{el}}} d^3r d^3r' \frac{\nabla \cdot \mathbf{f}_n(\mathbf{r}) \nabla' \cdot \mathbf{f}_n^*(\mathbf{r}')}{|\mathbf{r} - \mathbf{r}'|^2 + a^2}. \quad (7.7)$$

Here ω_D is the Debye frequency. U_n can be interpreted as an energy associated with mass-density fluctuations interacting via an inverse-square potential [123], cut off at distances of the order of the lattice constant a . We have reduced the calculation of P to the calculation of $F(\omega)$. Allen [124] has derived a related weighted-DOS formalism.

We now calculate $F(\omega)$ and P for a metal film of thickness d attached to the free surface of an isotropic elastic continuum with $L \rightarrow \infty$; see the inset to Fig. 7.1. The film and substrate are assumed to have the same elastic parameters, characterized by a mass density ρ and bulk sound velocities v_t and v_l . Where material parameters are necessary we shall assume a Cu film; however, the qualitative behavior we obtain is generic. The evaluation of $F(\omega)$ requires the vibrational eigenfunctions for a semi-infinite substrate with a free surface, which have been obtained in the classic paper by Ezawa [125]. The modes are labeled by a branch index m , taking the five values SH, +, -, 0, and R, by a two-dimensional wavevector \mathbf{K} in the plane defined by the surface, and by a parameter c with the dimensions of velocity that is continuous for all branches except the Rayleigh branch $m=R$. With the normalization convention of Ref. [125] we have

$$F(\omega) = \sum_{\mathbf{K}} U_{\text{R}\mathbf{K}} \delta(\omega - c_{\text{R}}K) \\ + \sum_{m \neq \text{R}} \sum_{\mathbf{K}} \int dc U_{m\mathbf{K}c} \delta(\omega - cK). \quad (7.8)$$

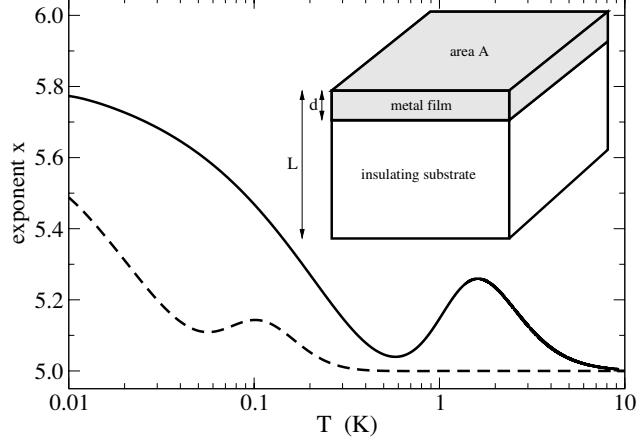


Figure 7.1: (inset) Conducting film of thickness d attached to insulator. The top surface of the metal is stress-free. (main) Temperature dependence of the thermal power exponent x for a 10 nm (solid curve) and 100 nm (dashed curve) Cu film.

The range of the parameter c depends on the branch m , and is summarized in Table 7.1. The frequency of mode $m\mathbf{K}c$ is cK .

m	range of c
SH	$[v_t, \infty]$
\pm	$[v_l, \infty]$
0	$[v_t, v_l]$
R	c_R (discrete)

Table 7.1: Values of the parameter c for the five branches of vibrational modes of a semi-infinite substrate.

Turning to an evaluation of (7.8), the SH branch is purely transverse, so $U_{\text{SH}} = 0$. The normalized eigenmodes for the \pm branches are

$$\begin{aligned}
 \mathbf{f}_{\pm} = & \sqrt{\frac{K}{4\pi cA}} \left\{ \left[\mp \alpha^{-\frac{1}{2}} (e^{-i\alpha Kz} - \zeta_{\pm} e^{i\alpha Kz}) + i\beta^{\frac{1}{2}} \right. \right. \\
 & \times (e^{-i\beta Kz} + \zeta_{\pm} e^{i\beta Kz}) \Big] \mathbf{e}_K + \left[\pm \alpha^{\frac{1}{2}} (e^{-i\alpha Kz} + \zeta_{\pm} e^{i\alpha Kz}) \right. \\
 & \left. \left. + i\beta^{-\frac{1}{2}} (e^{-i\beta Kz} - \zeta_{\pm} e^{i\beta Kz}) \right] \mathbf{e}_z \right\} e^{i\mathbf{K} \cdot \mathbf{r}}, \quad (7.9)
 \end{aligned}$$

where $\alpha \equiv \sqrt{(c/v_l)^2 - 1}$ and $\beta \equiv \sqrt{(c/v_t)^2 - 1}$. Here

$$\zeta_{\pm} \equiv \frac{[(\beta^2 - 1) \pm 2i\sqrt{\alpha\beta}]^2}{(\beta^2 - 1)^2 + 4\alpha\beta}, \quad \text{with} \quad |\zeta_{\pm}| = 1. \quad (7.10)$$

Then

$$\nabla \cdot \mathbf{f}_{\pm} = \mp i \frac{c^{\frac{3}{2}} K^{\frac{3}{2}}}{\sqrt{4\pi\alpha A} v_1^2} (e^{-i\alpha K z} - \zeta_{\pm} e^{i\alpha K z}) e^{i\mathbf{K} \cdot \mathbf{r}} \quad (7.11)$$

and $U_{\pm} = (c^3 K / \alpha v_1^4 V_{\text{el}}) I_{\pm}(Kd, c)$, where

$$\begin{aligned} I_{\pm}(Z, c) &\equiv \text{Re} \int_0^Z dx dx' \mathcal{K}_0(\sqrt{(x-x')^2 + a^2 Z^2 / d^2}) \\ &\times [e^{i\alpha(x-x')} - \zeta_{\pm} e^{i\alpha(x+x')}] . \end{aligned}$$

\mathcal{K}_0 is a modified Bessel function. To obtain U_{\pm} we use translational invariance in the xy plane to write (7.7) as

$$\begin{aligned} U_{m\mathbf{K}c} &= \frac{A}{V_{\text{el}}} \int_0^d dz dz' \int_A d^2 R \\ &\times \frac{\nabla \cdot \mathbf{f}_{m\mathbf{K}c}(\mathbf{R}, z) \nabla' \cdot \mathbf{f}_{m\mathbf{K}c}^*(0, z')}{R^2 + (z - z')^2 + a^2} , \end{aligned} \quad (7.12)$$

where $\mathbf{R} \equiv (x, y)$ is a two-dimensional coordinate vector. Then we scale out K , do the angular integration, and use the identity $\int_0^\infty dR R \mathcal{J}_0(R) [R^2 + s^2]^{-1} = \mathcal{K}_0(|s|)$, where \mathcal{J}_0 is a Bessel function of the first kind.

Next we consider the $m = 0$ branch, for which

$$\begin{aligned} \mathbf{f}_0 &= \sqrt{\frac{K}{2\pi\beta c A}} \left\{ \left[i\mathcal{C} e^{-\gamma K z} + i\beta e^{-i\beta K z} + i\beta \mathcal{A} e^{i\beta K z} \right] \mathbf{e}_K \right. \\ &+ \left. \left[-\gamma \mathcal{C} e^{-\gamma K z} + i e^{-i\beta K z} - i \mathcal{A} e^{i\beta K z} \right] \mathbf{e}_z \right\} e^{i\mathbf{K} \cdot \mathbf{r}} , \end{aligned} \quad (7.13)$$

where $\gamma \equiv \sqrt{1 - (c/v_1)^2}$,

$$\mathcal{A} \equiv \frac{(\beta^2 - 1)^2 - 4i\beta\gamma}{(\beta^2 - 1)^2 + 4i\beta\gamma}, \quad \text{and} \quad \mathcal{C} \equiv \frac{4\beta(\beta^2 - 1)}{(\beta^2 - 1)^2 + 4i\beta\gamma}.$$

Then

$$\nabla \cdot \mathbf{f}_0 = -\frac{c^{\frac{3}{2}} K^{\frac{3}{2}} \mathcal{C}}{\sqrt{2\pi\beta A} v_1^2} e^{-\gamma K z} e^{i\mathbf{K} \cdot \mathbf{r}} \quad (7.14)$$

and $U_0 = (|\mathcal{C}|^2 c^3 K / \beta v_1^4 V_{\text{el}}) I_0(Kd, c)$, where

$$I_0(Z, c) \equiv \int_0^Z dx dx' \mathcal{K}_0(\sqrt{(x-x')^2 + a^2 Z^2 / d^2}) e^{-\gamma(x+x')}.$$

Finally, for the Rayleigh branch,

$$\begin{aligned} \mathbf{f}_R &= \sqrt{\frac{K}{\mathcal{K} A}} \left\{ \left[i e^{-\varphi K z} - i \left(\frac{2\varphi\eta}{1+\eta^2} \right) e^{-\eta K z} \right] \mathbf{e}_K \right. \\ &- \left. \left[\varphi e^{-\varphi K z} - \left(\frac{2\varphi}{1+\eta^2} \right) e^{-\eta K z} \right] \mathbf{e}_z \right\} e^{i\mathbf{K} \cdot \mathbf{r}} , \end{aligned} \quad (7.15)$$

where $\varphi \equiv \sqrt{1 - (c_R/v_l)^2}$, $\eta \equiv \sqrt{1 - (c_R/v_t)^2}$, and $\mathcal{K} \equiv (\varphi - \eta)(\varphi - \eta + 2\varphi\eta^2)/2\varphi\eta^2$. c_R is the velocity of the Rayleigh surface waves, given by $c_R = \xi v_t$, where ξ is the root between 0 and 1 of $\xi^6 - 8\xi^4 + 8(3 - 2\nu^2)\xi^2 - 16(1 - \nu^2)$, with $\nu \equiv v_t/v_l$. For Cu, $\nu = 0.52$ and $\xi = 0.93$; hence $c_R = 2.4 \times 10^5 \text{ cm s}^{-1}$. Using (7.15),

$$\nabla \cdot \mathbf{f}_R = \frac{K^{\frac{3}{2}}(\varphi^2 - 1)}{\sqrt{\mathcal{K}A}} e^{i\mathbf{K} \cdot \mathbf{r}} e^{-\varphi K z} \quad (7.16)$$

and $U_R = (2\pi c_R^4 K / \mathcal{K} v_l^4 V_{\text{el}}) I_R(Kd)$, where

$$I_R(Z) \equiv \int_0^Z dx dx' K_0(\sqrt{(x-x')^2 + a^2 Z^2/d^2}) e^{-\varphi(x+x')}.$$

The final summations in (7.8) are carried out with the aid of the identity $\lim_{A \rightarrow \infty} \sum_{\mathbf{K}} \delta(\omega - cK) = \omega A / 2\pi c^2$ and elsewhere replacing K with ω/c . Then we obtain

$$\begin{aligned} F(\omega) &= \frac{\omega^2}{v_l^4 d} \left\{ \frac{c_R}{\mathcal{K}} I_R\left(\frac{\omega d}{c_R}\right) + \int_{v_t}^{v_l} dc \frac{|C|^2}{2\pi\beta} I_0\left(\frac{\omega d}{c}, c\right) \right. \\ &\quad \left. + \int_{v_l}^{\infty} dc \frac{1}{2\pi\alpha} [I_+(\frac{\omega d}{c}, c) + I_-(\frac{\omega d}{c}, c)] \right\}. \end{aligned} \quad (7.17)$$

This expression, combined with (7.6), is our principal result. Evaluation of (7.17) can be further simplified by the use of the powerful identities

$$\begin{aligned} I_{\pm}(Z, c) &= \text{Re} \left[\left(2Z - \frac{i\zeta_{\pm}}{\alpha} \right) f(Z, \alpha) + \frac{i\zeta_{\pm}}{\alpha} e^{2i\alpha Z} f^*(Z, \alpha) \right. \\ &\quad \left. + 2i \left(\frac{\partial f(Z, s)}{\partial s} \right)_{s=\alpha} \right], \end{aligned} \quad (7.18)$$

$$I_0(Z, c) = \frac{1}{\gamma} f(Z, i\gamma) - \frac{e^{-2\gamma Z}}{\gamma} f(Z, -i\gamma), \quad (7.19)$$

$$I_R(Z, c) = \frac{1}{\varphi} f(Z, i\varphi) - \frac{e^{-2\varphi Z}}{\varphi} f(Z, -i\varphi), \quad (7.20)$$

where $f(Z, s) \equiv \int_0^Z dx K_0(\sqrt{x^2 + a^2 Z^2/d^2}) e^{isx}$, thereby reducing the I_m to a single one-dimensional integral f .

The I_m have distinct large- and small- Z character, crossing over near $Z = 1$. Because of the integration over c in (7.17), F and P accordingly exhibit a broad crossover behavior. However, once $\omega d < c_R$, all branches will have assumed their low-frequency forms. We define a crossover temperature

$$T^* \equiv \hbar c_R / k_B d \quad (7.21)$$

dividing regimes determined by the small and large $\omega d/c_R$ behavior of F . In the large $\omega d/c_R$ limit the $m = \pm$ modes in (7.17) can be shown to be dominant, and $\lim_{\omega d \rightarrow \infty} \int_{v_l}^{\infty} dc \frac{1}{\alpha} I_{\pm}(\frac{\omega d}{c}, c) = \pi \omega d$. Therefore, we obtain $F(\omega) \rightarrow F_{\text{bulk}}(\omega) \equiv \omega^3/v_l^4$, independent of d , leading to a high-temperature behavior $P \rightarrow \Sigma V_{\text{el}}[\Phi(\omega_D/T_{\text{el}}) T_{\text{el}}^5 - \Phi(\omega_D/T_{\text{ph}}) T_{\text{ph}}^5]$, where Σ is the coefficient (7.2), and where $\Phi(y) \equiv [4! \zeta(5)]^{-1} \int_0^y dx x^4/(e^x - 1)$. $\Phi(10)$ is about 0.97, and $\Phi(y)$ rapidly approaches 1 beyond that. Thus, at temperatures above T^* but sufficiently smaller than the Debye temperature, the Φ factors are equal to unity, and we recover the bulk result (7.1).

The low temperature asymptotic analysis is somewhat complicated and will be presented elsewhere. Briefly, using the small Z expansion

$$\begin{aligned} f(Z, s) \rightarrow & -Z \ln Z + (1 + \ln 2 + \psi(1))Z - \frac{is}{2} Z^2 \ln Z \\ & + \frac{is}{2} \left(\frac{1}{2} + \ln 2 + \psi(1)\right) Z^2 + O(Z^3 \ln Z), \end{aligned} \quad (7.22)$$

where ψ is the Euler polygamma function, we find $F(\omega) \rightarrow F_{\text{bulk}}(\omega) \times [-\lambda (\frac{\omega d}{c_R}) \ln(\frac{\omega d}{c_R}) + O(\frac{\omega d}{c_R})]$ in the small $\omega d/c_R$ limit. Here

$$\lambda \equiv \frac{1}{\mathcal{K}} + \int_{v_t}^{v_l} dc \frac{c_R |\mathcal{C}|^2}{2\pi c^2 \beta} + \int_{v_l}^{\infty} dc \frac{c_R [2 - \text{Re}(\xi_+ + \xi_-)]}{2\pi c^2 \alpha}$$

is a constant determined by v_l , v_t , and c_R . Each T^5 function in (7.1) therefore crosses over at low temperature as $T^5 \rightarrow -\Lambda (\frac{T^6}{T^*}) \ln(\frac{T}{T^*})$, with $\Lambda = \lambda \pi^6/189 \zeta(5)$. For a Cu film, $\lambda \approx 0.815$ and $\Lambda \approx 3.998$. There are also mixed-temperature regimes possible, where only one of the two terms in (7.1) has crossed over.

The most striking consequence of the crossover is that the temperature exponent increases. In Fig. 7.1 we fit P (with either V_{el} or V_{ph} zero) to a power-law T^x with a temperature dependent exponent x , and plot the exponent for 10 nm ($T^* = 1.84$ K) and 100 nm ($T^* = 184$ mK) Cu films. $x(T)$ is nonmonotonic, displaying a pronounced maximum near T^* , and drifts upward as $T \rightarrow 0$. Such behavior has not (to the best of our knowledge) been observed, even though many experiments [114, 116, 117, 119] have achieved $T \ll T^*$. The physical origin of the crossover is that, at low temperature, the stress-free condition at the metal surface penetrates into the film, reducing the strain and hence electron-phonon coupling there. The characteristic distance over which the boundary condition has an effect is of the order of a bulk wavelength. When $T \gg T^*$, only a thin

outer surface layer of the film has a significantly diminished strain, and bulk behavior is expected. However, when $T \ll T^*$ the entire metal film experiences a reduced strain.

The experiments of Refs. [116] and [117], both using Cu films, observe an approximate T^5 dependence even well below T^* . It is therefore interesting to compare the observed *prefactors* with the coefficient Σ , evaluated for Cu. Using a free-electron gas approximation [126] and measured elastic properties [127], we obtain $5.97 \times 10^7 \text{ W m}^{-3} \text{ K}^{-5}$, which is at least an order of magnitude smaller than observed, consistent with our assertion that there is some unidentified mechanism *enhancing* the thermal coupling. Nobel metals are far from free-electron systems because of their complex Fermi surfaces. We attempt to address this shortcoming by regarding the “Fermi surface” quantities $N_{\text{el}}(\epsilon_{\text{F}})$ and v_{F} as independently adjustable parameters, to be obtained empirically from heat capacity and cyclotron resonance data. Carrying out this analysis, the details of which will be presented elsewhere, leads to the modified prefactor $\Sigma = 1.14 \times 10^8 \text{ W m}^{-3} \text{ K}^{-5}$, which is still considerably smaller than measured.

Although not included in the model considered here, disorder in a bulk metal film is expected to produce a crossover from the T^5 dependence to a T^6 scaling when the phonon elastic mean free path ℓ becomes smaller than the thermal wavelength [128, 129], a behavior which has not been reported experimentally until very recently [130]. Thus, the crossover predicted here should not be appreciably affected by disorder unless $\ell < d$. Although thin films are known to scatter phonons strongly, measured values of ℓ are still much larger than d in the temperature regime of interest here [131].

In conclusion, we argue that a wide variety of experiments contradict the predictions of an essentially exact application of the standard model of electron-phonon thermal coupling in metals to a supported-film geometry, suggesting a widespread breakdown of that model.

CHAPTER 8

CONCLUSION

A self-consistent dressed random phase approximation has been advanced to compute the finite temperature Green's function for the spherically symmetric nanoparticles. The finite element method is applied for the first time to solve the Dyson equations for the finite temperature Green's function and the screening potential, which provides an efficient and easy to operate methods, and leaves considerable freedom for users to choose the interpolation polynomials. The linear response theory is used to calculate the dynamical polarizability of the electron systems.

The corresponding large scale computer codes have been completed in the frame of the FORTRAN language. The dynamical polarizabilities for Gold and Sodium nanospheres are calculated, and the finite size effects have been discussed. The validity of codes and the methods involved in this work have been proved by these test cases.

A general method is introduced to calculate the transmission of scalar waves appropriate for mesoscopic electron and phonon transport through a curved wire or waveguide. Applications to electron transport accurately reproduce results obtained by other methods. Phonon transport through curved wires is considered here for the first time.

The curvature hardly suppresses thermal transport, even for sharply bent wires, at least within the 2-D scalar phonon model. Nanotubes would be interesting systems to investigate the effects of bending on transport.

A general method is developed to compute the net rate of thermal energy transfer between a three-dimensional conductor at temperature T_{el} and a low-dimensional phonon system at temperature T_{ph} . The standard electron-phonon coupling model is applied to a semi-infinite substrate with free surface. It predicts a low-temperature crossover from the familiar T^5 temperature dependence to a strong $T^6 \log T$ scaling. Comparison with existing experiments suggests a widespread breakdown of the standard model of electron-phonon thermalization in metals

BIBLIOGRAPHY

- [1] W. J. Parak, in *Nanoparticles*, ed. by G. Schmid (Wiley-VCH Verlag GmbH & Co.KGaA, Weinheim, 2004).
- [2] N. Lane, *J. of Nanoparticle Research* **3**, 95-103(2001).
- [3] R. F. Service, *Science* **271**, 920-922(1996).
- [4] R. F. Service, *Science* **290**, 1526-1567(2000).
- [5] W. D. Knight, K. Clemenger, W. A. de Heer, W. A. Saunders, M. Y. Chou and M. L. Cohen, *Phys. Rev. Lett.* **52**,2141-2143(1984).
- [6] K. Clemenger, *Phys. Rev. B* **32**, 1359-1362(1985).
- [7] K. Clemenger, *Phys. Rev. B* **44**, 12991-13001(1991).
- [8] D.J. Wales, *Science* **271**, 925-929(1996).
- [9] E. Beztig, J.K. Trautman, *Science* **257**, 189-195(1992).
- [10] R.P. Andres, T. Bein, M. Dorogi, S. Feng, J.I., Herderson, C.P. Kubiak, W. Mahoney, R.G. Osifchin, and R. Reifenberger, *Science* **272**, 1323-1325(1996).
- [11] R. D. Schaller and V. I. Klimov, *Phys. Rev. Lett.* **92**,186601(2004).
- [12] M. -C. Daniel and D. Astruc, *Chem. Rev.* **104**, 293-346(2004).
- [13] B. C. Gates, L. Guzzi, and H. Knözinger(ed.), *Metal clusters in catalysis* (Elsevier, Amsterdam, 1986).
- [14] S. Mandal, S. Phadtare and M Sastry, *Current Appl. Phys.* **5**,118-127(2005).
- [15] O Salata, *J. Nanobiotechnology* **2** No.3(2004).

- [16] A. A. Lazarides, K. L. Kelly, T. R. Jensen, and G. C. Schatz, J. Mol. Struct.(Theochem) **529**, 59-63(2000).
- [17] W. A. de Heer, Rev. Mod. Phys. **65**, 611-676(1993).
- [18] M. Brack, Rev. Mod. Phys. **65**, 677-732(1993).
- [19] V. Kasperovich and V. V. Kresin, Phil. Mag. B **78**,385-396(1998).
- [20] U. Kreibig and M. Vollmer, *Optical properties of metal clusters*(Springer-Verlag,Berlin, 1995).
- [21] S. Link and M. A. El-Sayed, Int. Rev. Phys. Chem **19**, 409-453(2000).
- [22] S. Link and M. A. El-Sayed, Ann. Rev. Phys. Chem **54**, 331-366(2003).
- [23] W. A. de Heer, K. Selby, V. Kresin, M. Vollmer, A. Châtelain, and W. D. Knight, Phys. Rev. Lett. **59**,1805-1808(1987).
- [24] K. Selby, M Vollmer, J. Masui, V. Kresin, W. A. de Heer, A. Scheidemann, and W. D. Knight, Phys. Rev. B **40**,5417-5427(1989).
- [25] K. Selby, V. Kresin, J. Masui, M Vollmer, W. A. de Heer, A. Scheidemann, and W. D. Knight, Phys. Rev. B **43**,4565-4572(1991).
- [26] T. Reiners, C. Ellert, M. Schmidt, and H. Haberland, Phys. Rev. Lett. **74**,1558-1561(1995).
- [27] J. Blanc, V. Bonačić-Koutecký, M. Broyer, J. Chevalereyre, P. Dugourd, J. Koutecký, C. Scheuch, J. P. Wolf, and L. Wöste, J. Chem. Phys. **96**, 1793-(1992).
- [28] J. Borggreen, P. Chowdhury, N. Kebaïli, L. Lundsberg-Nielsen, K, Lützenkirchen, M. B. Nielsen, J. Pedersen, and H. D. Rasmussen, Phys. Rev. B **48**, 17507-17516(1993).
- [29] B. Palpant, B. Prével, J. Lermé, E. Cottancin, M. Pellarin, M. Treilleux, A. Perez, J.L. Vialle, and M Broyer, Phys. Rev. B **57**, 1963-1970(1998).
- [30] M. Quinten, J. Clusters Science **10**, 319-358(1999).
- [31] J. -Y. Bigot, V. Halte, J. -C. Merlé, and A. Daunois, Chem. Phys. **251**,181-203(2000).

- [32] W. Pfeiffer, C. Kennerknecht and M. Merschdorf, Appl. Phys. A **78**,1011-1028(2004).
- [33] M. Dressel and G. Grüner, *Electrodynamics of Solids:Optical properties of electrons in matter* (Cambridge University Press, Cambridge, 2002).
- [34] N. W. Ashcroft and N. D. Mermin, *Solid State Physics*(Harcourt, Inc., Orlando, 1976).
- [35] N. D. Land and W. Kohn, Phys. Rev. B **1**, 4555-4568(1970); Phys. Rev. B **3**, 1215-1223 (1971); Phys. Rev. B **7**, 3541-3550(1970).
- [36] M. Y. Chou, A. Cleland and M. L. Cohen, Solid State Commun. **52**,645(1984).
- [37] W. Ekardt, Phys. Rev. B **29**, 1558-1564(1984).
- [38] W. Ekardt, Phys. Rev. Lett. **52**, 1925-1928(1984).
- [39] D. E. Beck, Phys. Rev. B **30**, 6935-6942(1984).
- [40] W. Ekardt, Phys. Rev. B **31**, 6360-6370(1985).
- [41] O. Gunnarsson and B. I. Lundqvist, Phys. Rev. B **13**, 4274–4298(1976).
- [42] M. J. Puska, R. M. Nieminen and M. Manninen, Phys. Rev. B **31**, 3486-3495(1985).
- [43] C. Yannouleas, R. A. Broglia, M. Brack, and P. F. Bortignon, Phys. Rev. Lett. **63**, 255–258(1989).
- [44] C. Yannouleas and R. A. Broglia, Phys. Rev. B **44**, 5793–5802(1991).
- [45] C. Yannouleas, E. Vigezzi and R. A. Broglia, Phys. Rev. B **47**, 9849–9861(1993).
- [46] M. Brack, Phys. Rev. B **39**, 3533–3542(1989).
- [47] G. F. Bertsch, Comput. Phys. Commun., **60**, 247–255(1990).
- [48] C. Guet and W. R. Johnson, Phys. Rev. B **45**, 11283–11287(1992).
- [49] A. Liebsch, Phys. Rev. Lett. **71**, 145–148(1993); Phys. Rev. B **48**, 11317–11328(1995).
- [50] V. V. Kresin, Phys. Rev. B **51**, 1844–1849(1995).

- [51] Ll. Serra and A. Rubio, Z. Phys. D **40**, 262–264(1997).
- [52] Ll. Serra and A. Rubio, Phys. Rev. Lett. **78**, 1428–1431(1997).
- [53] A. Rubio and Ll. Serra, Phys. Rev. B **48**, 18222–18229(1993).
- [54] J. Lermé, B. Ralpant, B. Préével, E. Cottancin, M. Pellarin, M. Treilleux, J. L. Vialle, A. Perez, and M. Broyer, Eur. Phys. J. D **4**, 95–108(1998).
- [55] J. Lermé, B. Ralpant, B. Préével, M. Pellarin, M. Treilleux, J. L. Vialle, A. Perez, and M. Broyer, Phys. Rev. Lett. **80**, 5105–5108(1998).
- [56] J. Lermé, Eur. Phys. J. D **4**, 265–277(2000).
- [57] L. I. Kurkina and O. V. Farberovich, Solid State Commun. **98**, 469–473(1996).
- [58] A. Bulgac, Czech. J. Phys. **48**, 696–701(1998).
- [59] S. A. Blundell, C. Guet and R. R. Zope, Phys. Rev. Lett. **84**, 4826–4829(2000).
- [60] K. Wong, G. Tikhonov and V. V. Kresin, Phys. Rev. B **66**, 125401(2002).
- [61] Alexander L. Fetter and John D Walecka, *Quantum Theory of Many-Particle Systems* (McGRAW-HILL BOOK COMPANY, New York, 1971).
- [62] Gerald D. Mahan, *Many particle Physics* (Plenum Press, New York, 1981).
- [63] A. A. Abrikosov, L. P. Gorkov and I. E. Dzyaloshinski, *Methods of Quantum Field Theory in Statistical Physics* (Dover Publications, INC., New York, 1975).
- [64] Matsubara T., Prog. Theor. Phys. (Kyoto) **14**, 351–378(1955).
- [65] Speth J., Werner E and Wild W, Phys. Rep. **33**, 127–208(1977)
- [66] M. E. Rose, *Elementary Theory of Angular Momentum* (Dover Publications, INC, New York, 1995).
- [67] William G. Strange and George J. Fix, *An analysis of the finite element method* (Prentice-Hall, Englewood Cliffs, 1973).

- [68] R. Gruber (ed.), *Finite elements in physics: proceedings of the 1st European Graduate Summer Course on Computational Physics Lausanne, Switzerland, 1-10 September 1986*(Elsevier Science, Amsterdam, 1986).
- [69] L. Ramdas Ram-Mohan, *Finite Element and Boundary Element Applications in Quantum Mechanics*(Oxford University Press, New York, 2002).
- [70] E. Merzbacher, *Quantum mechanics*, 2nd ed., chapter 4,(John Wiley & Sons, New York, 1970).
- [71] E. Anderson, Z. Bai, C. Bischof, S. Blackford, J. Demmel, J. Dongarra, J. Du Croz, A. Greenbaum, S. Hammarling, A. McKenney, and D. Sorensen, *LAPACK users' guide*, 3rd ed.,(Society for Industrial and Applied Mathematics, Philadelphia, 1999).
- [72] I. S. Gradshteyn/I. M. Ryzhik, *Table of Integrals, Series, and products*(Academic Press, New York, 1980).
- [73] G. A. Baker Jr., *Essentials of Padé Approximants* (Academic Press, New York, 1975).
- [74] George Arfken, *Mathematical methods for physicists*, 3rd ed.,(Academic Press, Orlando, 1985).
- [75] Enrico Lipparini, *Modern many-particle physics* (World Scientific, New Jersey, 2003).
- [76] T. S. Tighe, J. M. Worlock and M. L. Roukes, *Appl. Phys. Lett.* **70**, 2687(1997).
- [77] M. L. Roukes, *Physica B* **263**, 1(1999).
- [78] K. Schwab, E. A. Henriksen, J. M. Worlock, and M. L. Roukes, *Nature* **404**, 97(2000).
- [79] C. S. Yung, D. R. Schmidt, and A. N. Cleland, *Appl. Phys. Lett.* **81**, 31(2002).
- [80] A. N. Cleland, *Foundations of Nanomechanics* (Springer-Verlag, 2002).
- [81] C. W. J. Beenakker and H. van Houten, in *Solid State Physics: Advances in Research and Applications*, edited by H. Ehrenreich and D. Turnbull (Academic Press, 1991), Vol. 44.
- [82] S. Datta, *Electronic Transport in Mesoscopic Systems* (Cambridge University Press, 1997).
- [83] N. Nishiguchi, Y. Ando, and M. N. Wybourne, *J. Phys.: Condens. Matter* **9**, 5751 (1997).

- [84] L. G. C. Rego and G. Kirczenow, Phys. Rev. Lett. **81**, 232 (1998).
- [85] D. E. Angelescu, M. C. Cross, and M. L. Roukes, Superlattices Microstruct. **23**, 673 (1998).
- [86] M. P. Blencowe, Phys. Rev. B **59**, 4992 (1999).
- [87] A. Kambili, G. Fagas, V. I. Falko, and C. J. Lambert, Phys. Rev. B **60**, 15593 (1999).
- [88] A. Buldum, D. M. Leitner, and S. Ciraci, Europhys. Lett. **47**, 208 (1999).
- [89] D. M. Leitner and P. G. Wolynes, Phys. Rev. E **61**, 2902 (2000).
- [90] M. P. Blencowe and V. Vitelli, Phys. Rev. A **62**, 52104 (2000).
- [91] A. Ozpineci and S. Ciraci, Phys. Rev. B **63**, 125415 (2001).
- [92] M. C. Cross and R. Lifshitz, Phys. Rev. B **64**, 85324 (2001).
- [93] B. A. Glavin, Phys. Rev. Lett. **86**, 4318 (2001).
- [94] D. H. Santamore and M. C. Cross, Phys. Rev. Lett. **87**, 115502 (2001).
- [95] K. R. Patton and M. R. Geller, Phys. Rev. B **64**, 155320 (2001).
- [96] A. N. Cleland, D. R. Schmidt, and C. S. Yung, Phys. Rev. B **64**, 172301 (2001).
- [97] Q.-F. Sun, P. Yang, and H. Guo, Phys. Rev. Lett. **89**, 175901 (2002).
- [98] It will be sufficient to assume that the curves $\mathbf{r}(s)$ defining the edges of the wire as a function of arclength s are of class C^2 (derivatives through second order exist and are continuous).
- [99] The two-dimensional Helmholtz equation is valid at energy scales considerably less than v/d , where d is the thickness of the wire in the z direction.
- [100] J. T. Londergan, J. P. Carini, and D. P. Murdock, *Binding and Scattering in Two-Dimensional Systems: Applications to Quantum Wires, Waveguides, and Photonic Crystals* (Springer-Verlag, 1999).
- [101] P. Exner and P. Seba, J. Math. Phys. **30**, 2574 (1989).

- [102] J. Goldstone and R. L. Jaffe, Phys. Rev. B **45**, 14100 (1992).
- [103] Our method, of course, has its own limitations. For example, in the present formulation the width of the wire is assumed to be constant.
- [104] L. Lewin, *Theory of Waveguides* (John Wiley and Sons, 1975).
- [105] R. E. Collin, *Field Theory of Guided Waves*, 2nd ed. (IEEE Press, 1991).
- [106] F. Sols and M. Macucci, Phys. Rev. B **41**, 11887 (1990).
- [107] K. Lin and R. L. Jaffe, Phys. Rev. B **54**, 5750 (1996).
- [108] We thank Aleksandar Milošević for this observation.
- [109] H. U. Baranger, Phys. Rev. B **42**, 11479 (1990).
- [110] J. Hone, M. Whitney, C. Piskoti, and A. Zettl, Phys. Rev. B **59**, R2514 (1999).
- [111] P. Kim, L. Shi, A. Majumdar, and P. L. McEuen, Phys. Rev. Lett. **87**, 215502 (2001).
- [112] D. J. Yang, Q. Zhang, G. Chen, S. F. Yoon, J. Ahn, S. G. Wang, Q. Zhou, Q. Wang, and J. Q. Li, Phys. Rev. B **66**, 165440 (2002).
- [113] V. F. Gantmakher, Rep. Prog. Phys. **37**, 317(1974).
- [114] F. C. Wellstood, C. Urbina and J. Clarke, Phys. Rev. B **49**, 5942(1994).
- [115] W. A. Little, Can. J. Phys. **37**, 334(1959).
- [116] M. L. Roukes, M. R. Freeman, R. S. Germain, R. C. Richardson, M. B. Ketchen, Phys. Rev. Lett. **55**, 422 (1985).
- [117] C. S. Yung, D. R. Schmidt, and A. N. Cleland, Appl. Phys. Lett. **81**, 31 (2002).
- [118] J. Liu and N. Giordano, Phys. Rev. B **43**, 3928 (1991).
- [119] J. F. DiTusa, K. Lin, M. Park, M. S. Isaacson, and J. M. Parpia, Phys. Rev. Lett. **68**, 1156(1992).

- [120] M. L. Roukes, Physica B **263**, 1 (1999).
- [121] K. Schwab, E. A. Henriksen, J. M. Worlock, and M. L. Roukes, Nature (London) **404**, 974(2000).
- [122] D. R. Schmidt, R. J. Schoelkopf, and A. N. Cleland, Phys. Rev. Lett. **93**, 45901(2004).
- [123] Recall that, in elasticity theory, the mass-density fluctuation $\delta\rho$ is given by $-\rho\nabla\cdot\mathbf{u}$.
- [124] P. B. Allen, Phys. Rev. Lett. **59**, 1460(1987).
- [125] H. Ezawa, Ann. Phys. (N.Y.) **67**, 438(1971).
- [126] In the free-electron gas approximation, the Fermi energy of Cu is 7.03 eV, the DOS at ϵ_F is $1.13 \times 10^{34} \text{ erg}^{-1} \text{ cm}^{-3}$, and v_F is $1.57 \times 10^8 \text{ cm s}^{-1}$.
- [127] Cu has the low-temperature elastic constants $c_{11} = 1.76 \times 10^{12} \text{ dyne cm}^{-2}$, $c_{12} = 1.25 \times 10^{12} \text{ dyne cm}^{-2}$, and $c_{44} = 8.18 \times 10^{11} \text{ dyne cm}^{-2}$ [132], and its mass density is $\rho = 8.94 \text{ g cm}^{-3}$. To approximate a cubic material as an isotropic elastic continuum we define effective elastic constants $C_{11} \equiv c_{11} - 2\Delta$ and $C_{44} \equiv c_{44} + \Delta$, where $\Delta \equiv (c_{11} - c_{12} - 2c_{44})/5$, and we let $v_l = (C_{11}/\rho)^{\frac{1}{2}}$ and $v_t = (C_{44}/\rho)^{\frac{1}{2}}$. This leads to $v_l = 4.97 \times 10^5 \text{ cm s}^{-1}$.
- [128] B. Keck and A. Schmid, J. Low. Temp. Phys. **24**, 611(1976).
- [129] J. Rammer and A. Schmid, Phys. Rev. B **34**, 1352(1986).
- [130] I. J. Maasilta, J. T. Karvonen, J. M. Kivioja, and L. J. Taskinen, e-print cond-mat/0311031.
- [131] T. Klitsner and R. O. Pohl, Phys. Rev. B **36**, 6551(1987).
- [132] W. C. Overton and J. Gaffney, Phys. Rev. **98**, 969(1955).

APPENDIX A

SOME USEFUL RELATIONS FOR THE CLEBSCH-GODAN COEFFICIENTS

A.1 REDEFINED CLEBSCH-GODAN COEFFICIENTS \tilde{C}

Considering the feature of this work, we also use the redefined Clebsch-Gordan (CG) coefficients

$$\tilde{C}(l_1 l_2; m m_1 m_2) = \left(\frac{2l+1}{2l_2+1} \right)^{1/2} C(l_1 l_2; m m_1 m_2) \quad (\text{A.1})$$

where, $C(l_1 l_2; m m_1 m_2)$ is the conventional CG coefficients [66]. According to the following equation,

$$C(l_1 l_2; m m_1 m_2) = (-1)^{l_1+m_1} \left(\frac{2l_2+1}{2l+1} \right)^{1/2} C(l_1 l_2 l; -m_1 m_2 m) \quad (\text{A.2})$$

and the orthonormal relations

$$\sum_{m_1, m_2} C(l_1 l_2 l; m_1 m_2 m) C(l_1 l_2 l'; m_1 m_2 m') = \delta_{ll'} \delta_{mm'} \quad (\text{A.3})$$

$$\sum_{l, m} C(l_1 l_2 l; m_1 m_2 m) C(l_1 l_2 l'; m'_1 m'_2 m) = \delta_{m_1 m'_1} \delta_{m_2 m'_2} \quad (\text{A.4})$$

we obtain the corresponding relations for \tilde{C} ,

$$\sum_{m_1, m_2} \tilde{C}(l_1 l_2; m m_1 m_2) \tilde{C}(l'_1 l_2; m'_1 m_1 m_2) = \delta_{ll'} \delta_{mm'} \quad (\text{A.5})$$

$$\sum_{l, m} \tilde{C}(l_1 l_2; m m_1 m_2) \tilde{C}(l_1 l_2; m m'_1 m'_2) = \delta_{m_1 m'_1} \delta_{m_2 m'_2} \quad (\text{A.6})$$

and

$$\sum_{m_1, m_2} \tilde{C}(l_1 l_2 l; m_1 m_2 m) \tilde{C}(l_1 l_2 l'; m_1 m_2 m') = \frac{2l+1}{2l_2+1} \delta_{ll'} \delta_{mm'} \quad (\text{A.7})$$

$$\sum_{lm} \tilde{C}(l_1 l_2 l; m_1 m_2 m) \tilde{C}(l_1 l_2 l; m'_1 m'_2 m) = \frac{2l_1 + 1}{2l + 1} \delta_{lm} \delta_{m_2 m'_2} \quad (\text{A.8})$$

By this redefinition, the coupling rule for spherical harmonics [66] becomes

$$Y_{l_1 m_1}(\theta, \varphi) Y_{l_2 m_2}(\theta, \varphi) = \sum_{lm} \left[\frac{(2l_2 + 1)}{4\pi} \right]^{1/2} \tilde{C}(l_1 l_2 l; m_1 m_2 m) C(l_1 l_2 l; 000) Y_{lm}(\theta, \varphi) \quad (\text{A.9})$$

Then we have relation,

$$\int d\Omega Y_{l_3 m_3}^* Y_{l_2 m_2} Y_{l_1 m_1} = \left[\frac{(2l_2 + 1)}{4\pi} \right]^{1/2} \tilde{C}(l_1 l_2 l_3; m_1 m_2 m_3) C(l_1 l_2 l_3; 000) \quad (\text{A.10})$$

A.2 SOME SPECIAL CG COEFFICIENTS

Consider the following CG coefficients,

$$\begin{aligned} \tilde{C}(0l_\mu l_\nu; 0mm) &= \left(\frac{1}{2l_\nu + 1} \right)^{1/2} C(0l_\mu l_\nu; 0mm) \\ &= \left[\frac{(l_\mu - l_\nu)! (l_\nu - l_\mu)! (l_\nu + m)! (l_\nu - m)!}{(l_\mu + l_\nu + 1)! (l_\mu + m)! (l_\mu - m)!} \right]^{1/2} \sum_{\sigma} \frac{(-1)^{\sigma + l_\mu + m}}{(l_\nu + m - \sigma)! (\sigma - l_\mu - m)!} \end{aligned}$$

Here, the requirements $(l_\mu - l_\nu) \geq 0$ and $(l_\nu - l_\mu) \geq 0$ lead to the conclusion that the CG coefficients are zero unless $l_\mu = l_\nu$. When $l_\mu = l_\nu$, the requirements $(l_\mu + m - \sigma) \geq 0$ and $(-l_\mu - m + \sigma) \geq 0$ imply that $\sigma = l_\mu + m$, and then the summation gives,

$$\tilde{C}(0l_\mu l_\mu; 0mm) = (2l_\mu + 1)^{-1/2}$$

Therefore, we have

$$\tilde{C}(0l_\mu l_\nu; 0mm) = (2l_\mu + 1)^{-1/2} \delta_{l_\mu l_\nu} \quad (\text{A.11})$$

Then we calculate the following summation ($j > 0$),

$$\sum_m \tilde{C}(jll; 0mm) = \left[\frac{(2j + 1)(2l - j)!}{(2l + j + 1)!} \right]^{1/2} \frac{1}{j!} \sum_m \sum_{\sigma} \frac{(2l - \sigma)! (j + \sigma)!}{\sigma! (2l - j - \sigma)!} \frac{j! (-1)^{\sigma + l + m}}{(l + m - \sigma)! (j - l - m + \sigma)!}$$

To make the equation valid, the following conditions should be satisfied,

$$\sigma \geq 0, \quad 2l - \sigma \geq 0, \quad 2l - j - \sigma \geq 0, \quad (l + m - \sigma) \geq 0, \quad (j - l - m + \sigma) \geq 0$$

they yield the following limitation,

$$\begin{aligned} 0 &\leq \sigma \leq 2l - j \\ \sigma - l &\leq m \leq j - l + \sigma \end{aligned}$$

Set $l + m - \sigma = k$, the summation becomes,

$$\sum_m \tilde{C}(jll; 0mm) = \left[\frac{(2j+1)(2l-j)!}{(2l+j+1)!} \right]^{1/2} \frac{1}{j!} \sum_{\sigma} \frac{(2l-\sigma)!(j+\sigma)!}{(2l-j-\sigma)!\sigma!} \sum_{k=0}^j (-1)^k \frac{j!}{k!(j-k)!}$$

Considering formula [72],

$$\sum_{k=0}^m (-1)^k \binom{n}{k} = (-1)^m \binom{n-1}{m}, \quad [n \geq 1]$$

One may notes that the last summation in the equation becomes zero. Thus, we have

$$\sum_m \tilde{C}(jll; 0mm) = 0$$

Considering eq. (A.11), we get

$$\sum_m \tilde{C}(jll; 0mm) = (2l+1)^{1/2} \delta_{j,0} \quad (\text{A.12})$$

APPENDIX B

THE ASYMPTOTICAL BEHAVIOR OF THE RADIAL GREEN'S FUNCTION

The radial Green's function for a particle in a spherically symmetric potential reads,

$$\left\{ i\omega_n - V(r) + \mu + \frac{\hbar^2}{2m_e} \left[\frac{1}{r^2} \frac{d^2}{dr^2} r^2 - \frac{l(l+1)}{r^2} \right] \right\} G_l(r, r'; i\omega_n) = \frac{1}{rr'} \delta(r - r') \quad (\text{B.1})$$

Set,

$$\tilde{G}_l(r, r'; i\omega_n) = rr' G_l(r, r'; i\omega_n) \quad (\text{B.2})$$

we have the equation for $\tilde{G}_l(r, r'; i\omega)$,

$$\left\{ i\omega_n - V(r) + \mu + \frac{\hbar^2}{2m_e} \left[\frac{d^2}{dr^2} - \frac{l(l+1)}{r^2} \right] \right\} \tilde{G}_l(r, r'; i\omega_n) = \delta(r - r') \quad (\text{B.3})$$

In the limitation $x \rightarrow 0$, it reduces to,

$$\left[\frac{d^2}{dr^2} - \frac{l(l+1)}{r^2} \right] \tilde{G}_l(r, r') = \frac{2m_e}{\hbar^2} \delta(r - r') \quad (\text{B.4})$$

Integral over range $[r' - \epsilon, r' + \epsilon]$ and then take the limitation $\epsilon \rightarrow 0$, one may get the discontinuity condition of the derivative of the asymptotical Green's function, which is

$$\frac{\partial}{\partial r} \tilde{G}_l(r, r') \Big|_{r=r'+} - \frac{\partial}{\partial r} \tilde{G}_l(r, r') \Big|_{r=r'-} = \frac{2m_e}{\hbar^2} \quad (\text{B.5})$$

Suppose the solution of the homogeneous counterparty of eq.(B.4) take the form r^s , and substitute it into this counterparty, we get

$$s(s-1) = l(l+1)$$

The solutions of it are $s = l+1, -1$. Therefore, one may expresse the asymptotical behavior of $\tilde{G}_l(r, r')$ as,

$$\tilde{G}_l(r, r') = \begin{cases} A^{<} r^{l+1}, & r < r' \\ A^{>} r^{-l}, & r > r' \end{cases} \quad (\text{B.6})$$

The continuity of $\tilde{G}_l(r, r')$ and the discontinuity defined in eq.(B.5) at $r \rightarrow r'$ give,

$$A^< = -\frac{2m_e}{(2l+1)\hbar^2}r'^{-l}, \quad A^> = -\frac{2m_e}{(2l+1)\hbar^2}r'^{(l+1)} \quad (\text{B.7})$$

Thus the asymptotical form of the Green's function is,

$$\tilde{G}_l(r, r') \sim \begin{cases} -r^{l+1}/r'^l, & r < r' \\ -r'^{l+1}/r^l, & r > r' \end{cases} \quad (\text{B.8})$$

here we eliminate the constant $2m_e/(2l+1)\hbar^2$. The first order derivative is,

$$\frac{\partial}{\partial r}\tilde{G}_l(r, r') \sim \begin{cases} -r^l/r'^l, & r < r' \\ r'^{l+1}/r^{l+1}, & r > r' \end{cases} \quad (\text{B.9})$$

and the second order derivative is,

$$\frac{\partial^2}{\partial r' \partial r}\tilde{G}_l(r, r') \sim \begin{cases} r^l/r'^{l+1}, & r < r' \\ r'^l/r^{l+1}, & r > r' \end{cases} \quad (\text{B.10})$$

Clearly, the Green's function vanishes when both r and r' go to zero. The first order derivative for $l > 0$ tends to zero when both r and r' go to zero. It is finite when $r < r'$, and is 0 when $r > r'$ for $l = 0$. The second order derivative is undefined in the same limitation.

APPENDIX C

INTEGRALS INVOLVING PRODUCTS OF DIRAC DELTA FUNCTIONS AND STEP FUNCTIONS

Here we discuss integrals of the form

$$\int_{-\infty}^{\infty} dx F[\Theta(x)] \delta(x), \quad (\text{C.1})$$

where F is twice continuously differentiable, and $\Theta(x)$ and $\delta(x)$ are the unit step and Dirac delta functions, respectively. Integrals of the form (C.1), which involve *products* of generalized functions, depend sensitively on how $\Theta(x)$ and $\delta(x)$ are defined. It will be necessary to define $\Theta(x)$ and $\delta(x)$ according to their appearance in this work.

The step function $\Theta(x)$ appearing in Eq. (C.1) originated from the curvature profile of Eq. (6.42) used to describe a circular segment of wire connected to a straight lead, and the delta function comes from its derivative with respect to arclength in Eq. (6.43), which is required by the effective potential V of Eq. (6.21). Therefore we require $\Theta(x)$ to be smooth (on some microscopic scale) and continuous, and $\delta(x)$ to be related to it by

$$\frac{d}{dx} \Theta(x) = \delta(x). \quad (\text{C.2})$$

We also require, of course, that

$$\lim_{x \rightarrow -\infty} \Theta(x) = 0 \quad \text{and} \quad \lim_{x \rightarrow \infty} \Theta(x) = 1. \quad (\text{C.3})$$

The precise shape of $\Theta(x)$ near $x = 0$ is immaterial, but with no loss of generality we can require that $\Theta(0) = \frac{1}{2}$.

Integrals of the form (C.1) are now well defined. For example,

$$\int_{-\infty}^{\infty} dx \Theta(x) \delta(x) = \frac{1}{2}, \quad (\text{C.4})$$

as expected, but

$$\int_{-\infty}^{\infty} dx [\Theta(x)]^2 \delta(x) = \frac{1}{3}, \quad (\text{C.5})$$

instead of $\frac{1}{4}$. These results are obtained by integrating by parts and using the behavior of $\Theta(x)$ as $x \rightarrow \pm\infty$, *not* by evaluating $\Theta(0)$ and $[\Theta(0)]^2$. More generally,

$$\int_{-\infty}^{\infty} dx [\Theta(x)]^n \delta(x) = \frac{1}{n+1}, \quad (\text{for } n > 0) \quad (\text{C.6})$$

which is different from the naive value of $[\Theta(0)]^n = (\frac{1}{2})^n$, unless $n = 1$.

The reason why

$$\int_{-\infty}^{\infty} dx F[\Theta(x)] \delta(x) \neq F[\Theta(0)] \quad (\text{C.7})$$

in some of these examples is because the delta function is distributed over a small but finite region of x , whereas $\Theta(x)$ and $F[\Theta(x)]$ are generally *not* slowly varying over that length scale. We conclude, therefore, that integrals of the form (C.1) appearing in the evaluation of matrix elements of V , have to be evaluated using integration-by-parts (or with an equivalent method).